City Research Online

City, University of London Institutional Repository

Ultrasound Field Measurement and Modelling

for Non-Destructive Testing

John X Jian

Thesis submitted in fulfilment of the requirements

for the degree of Doctor of Philosophy

City, University of London

School of Mathematics, Computer Science and Engineering

May 2017

TABLE OF CONTENTS

DECLARATION

No portion of the work referred to in this thesis has been submitted in support of an application for another degree or qualification of this or any other university.

COPYRIGHT STATEMENT

Attention is drawn to the fact that copyright of this thesis rests with the author. A copy of this thesis has been supplied on condition that anyone who consults it is understood to recognise that its copyright rests with the author and that they must not copy it or use material from it except as permitted by law or with the consent of the author. Candidates wishing to include copyright material belonging to others in their thesis are advised to check with the copyright owner that they will give consent to the inclusion of any of their material in the thesis. If the material is to be copied other than by photocopying or facsimile then the request should be put to the publisher or the author in accordance with the copyright declaration in the volume concerned. If, however, a facsimile of photocopy will be included, then it is appropriate to write to the publisher alone for consent.

This thesis may be made available for consultation within the University Library and may be photocopied or lent to other libraries for the purpose of consultation.

ACKNOWLEDGEMENTS

ABSTRACT

Ultrasonic Testing (UT) is one of most important methods of Non-destructive Testing (NDT) and ultrasonic waves can be generated and detected by means of numeric methods. This thesis focuses on piezoelectric transducers and Electromagnetic Acoustical Transducer (EMAT).

For testing with piezoelectric transducer (also called a probe), couplant has to be applied between the test material and the probe allowing for ultrasonic waves generated in the probe by an active piezoelectric crystal to propagate into the testing material. The couplant can be water, mineral oil, or gel, dependent on the applications concerned and material compatibility, for example, water for immersion tests or automatated inspections.

No two piezoelectric transducer designs are identical in terms of their frequency range, beam propagation characteristics and directionality. The shape, dimensions, backing and matching of the transducer to the pulse generator together play a major role in the generation of the ultrasonic waves. Furthermore, the quantitative interpretation of pulse echo data obtained when such transducers are used in non-destructive evaluation (NDE) requires a complete knowledge of the ultrasonic field transmitted.

Ultrasonic fields of circular probes have been studied experimentally using a miniature probe and theoretically with models developed to predict ultrasonic field of such a probe. Good agreement has been observed. In a fluid, the ultrasonic field generated by a circular piezoelectric transducer can be described in terms of a combination of locally plane waves that radiate in the geometric region straight ahead of the active transducer element and edge waves radiating from the rim of the element. When a piezoelectric transducer is directly mounted onto a solid material, the ultrasonic field includes locally plane longitudinal waves, edge longitudinal waves and mode-converted edge shear waves. Both cases can be studied using miniature piezoelectric probes.

For electrically conductive materials, EMATs can be used for generation by means of Lorentz force or magnetostriction or both, and detection. EMAT technique is non-contact and couplant free and can work at high temperature. These attributes make it ideal for inspection in extreme conditions, such as high temperature, high speed, rough surface, etc. This thesis focuses on Lorentz force generation. The main disadvantages of an EMAT detector are its lower sensitivity compared to a piezoelectric probe and it is not straightforward to miniaturise the device to operate as a point sensor for the range of wavelengths of interest here. Therefore, optimal EMAT design is extremely important for successful EMAT application. Ultrasound may be generated without presence of external magnetic field as excitation electric current provides magnetic field as it induces eddy currents in the material under test, which creates Lorentz forces for ultrasonic generation. Where external magnetic field is applied, EMATs have to be designed correctly to achieve enhanced efficiency. As an example, Rayleigh wave EMAT generation has been studied. It is found that where external magnetic field is applied, constructive or destructive effects have been observed, which is understood dependent on direction of the external magnetic fields applied relevant to electric current direction. Optical interferometer to measure the true normal displacement of the solid surface with a resolution in the order of nanometres, but it is much more complex than an EMAT and a piezoelectric probe and requires an optically flat surface. The receiving EMAT detector measures particle velocity. By careful design, in-plane or out-of-plane (or both) velocities can be chosen for detection. This capability is very useful for the detection of longitudinal waves, shear waves, Rayleigh waves or Lamb waves efficiently.

The ultrasonic pulse-echo technique has been widely used in ultrasonic NDT. Ultrasonic pulse-echo responses and ultrasonic field signals are not the same. Typically, edge waves are rarely seen in a pulse echo response because the plane waves that are normal to the major face of the active crystal of the same probe are nearly in phase to constructively result in a significant signal whilst edge waves arrive at the active crystal in different directions and different phases cancelling each other and destructively producing only a small signal that is barely observable. As an example of ultrasonic pulse-echo application, weak bond evaluation, has been

performed. Weak bond evaluation has always been a challenge. As an example of practical applications, this study has evaluated Integrated Circuit packaging in electronic industry using scanning acoustical microscopy. The relationship among resulting ultrasonic C-scan images, destructive mechanical failure measurement, degradation cycles have been observed. The result is promising indicating the SAM is a very useful tool for weak bond evaluation.

Ultrasonic field measurement using a miniature probe and specially design EMAT is very important to characterize and standardize a probe. Such a technique can also find its applications in defect detection and categorization, which has not been considered in this study

NOMENCLATURE

ULTRASONIC FIELD IN FLUID OF A PIEZOELECTRIC TRANSDUCER

The ultrasonic field generated by a piezoelectric transducer (PZT) can be described in terms of a combination of locally plane waves that radiate in the geometric region straight ahead of the active piezoelectric crystal and edge waves radiating from the rim of the crystal.

ULTRASONIC FIELD IN SOLID A PIEZOELECTRIC TRANSDUCER

The ultrasonic field generated by a piezoelectric transducer directly mounted onto a solid material, includes locally plane longitudinal waves, edge longitudinal waves and mode-converted edge shear waves.

PLANE WAVE

For a practical piezoelectric transducer of a finite size of active piezoelectric crystal, the plane waves generated are not infinite plane waves, but "locally" plane waves. In this thesis, the term "locally" is dropped using PLANE WAVES for "locally" plane waves.

PC

Plane Compression/Longitudinal wave.

EC

Edge Compression/Longitudinal wave.

EDGE WAVE

For a practical piezoelectric transducer of a finite size of active piezoelectric crystal, edge waves radiate from the rim of the active piezoelectric crystal.

PS

Plane Shear/Transverse wave.

ES

Edge Shear/Transverse wave.

STATIC MAGENTIC FIELD

For EMAT ultrasonic generation considered in this thesis, it denotes the magnetic field that is created by a permanent magnet with its intensity assumed constant.

DYNAMIC MAGNETIC FIELD

For EMAT ultrasonic generation considered in this thesis, it denotes the magnetic field that is generated by continuous or pulsed currents flowing through an excitation coil. For pulsed current, the dynamic magnetic field is transient.

PULSE-ECHO TECHNIQUE

It is a technique using same probe to transmit ultrasonic waves into a material under test and to receive reflected or scattered ultrasonic wave from the material.

PITCH-CATCH TECHNIQUE

It is a technique using different probes to transmit ultrasonic waves into a material under test and another probe and to receive reflected or scattered ultrasonic wave from the material.

LIST OF FIGURES

1. INTRODUCTION

1.1 Motivation

Ultrasonic testing [1-3] is one of the three main volumetric Non-Destructive Testing (NDT) methods, i.e. ultrasonic testing, radiographic testing and electromagnetic testing. It is probably the most widely used NDT methods.

There are cases that ultrasonic field measurements are requested including

- To characterize and calibrate an ultrasonic transducer

- To understand the design of an ultrasonic transducer for particular NDT applications

- To understand ultrasonic propagation in a complex component or a wave guide

- To investigate defect scattering field for difficult and complicated inspections. This will help inspection design and enhance inspection capability.

- To research into ultrasonic mode conversion at an interface.

- To validate a model to predict ultrasonic field of an ultrasonic transducer.

- To validate a model to predict ultrasonic defect scattering field.

There are requirements on the testing sensors in order to measure ultrasonic field accurately including

- They should not interfere with the ultrasonic field.

A non-contact transducer, such as an EMAT is ideal. Contact area should be minimal if a piezoelectric transducer is applied.

- They should be able to take ultrasonic displacement/velocity in an intended orientation.

  There are cases that in-plane or out-of-plane displacement is of particular interest to an application.

- They should have reasonable sensitivity.

  Measured signal should be of acceptable signal to noise ratio.

- They should have a wider bandwidth than the probe to be measured.

- They should have acceptable lateral resolution and accuracy.

Ultrasonic field of a probe measured in pulse echo is not true ultrasonic field of the probe. The ultrasonic field generated by a conventional piezoelectric transducer for NDT consists of plane waves and edge waves. This phenomenon can't be observed by a measurement set in pulse echo.

Therefore, development and optimization of a receiving probe which meets the requirements above is very important for true ultrasonic field measurement.

1.2   Thesis Aims and Objectives

The aim of this study is to develop and optimise transducers that can be used to measure ultrasonic field in an intended orientation. Specific objectives of the research are as follows,

- A model for ultrasonic field of a typical piezoelectric transducer for NDT

- A model for ultrasonic field of an EMAT

- To develop transducers for the ultrasonic field measurement.

The objectives of this study are

- To carry out a literature review of ultrasonic transducers and ultrasonic field measurements.

- To explores the way to measure ultrasonic field in solid generated by typical Non-Destructive Testing piezoelectric transducer.

- To investigate ultrasonic transducers that can be used for ultrasonic field measurement, including miniature piezoelectric transducer and EMAT.

- Miniature probe design and optimization for ultrasonic field measurement

- EMAT design and optimization for ultrasonic field measurement

- To develop simples models to predict ultrasonic fields and to give explanation to experimental measurements.

- To measure ultrasonic field using a miniature piezoelectric transducer and compare measurements with theoretical predictions demonstrating its capability.

- To measure ultrasonic field using an EMAT and compare measurements with theoretical predictions demonstrating its capability.

- To use high frequency spherical focused transducer, for evaluation of weak bond in Integrated Circuit packaging.

1.3   Thesis outline

Chapter 2, Literature review

Literatures on ultrasonic field measurement and prediction have been reviewed in the chapter, covering piezoelectric transducer, Scanning Acoustical Microscopy (SAM), Capacitive Micromachined Ultrasonic Transducers (CMUTs), Electro-Magnetic Acoustical Transducers (EMATs), laser ultrasonic generation and detection.

Chapter 3, Ultrasonic Field Measurement using a Miniature Piezoelectric Transducer

This chapter reports on the characterization of specially developed miniature ultrasonic transducers as receivers which has been directly-coupled to a solid surface, to make field point measurements of the ultrasonic waves propagating from a pulsed transducer. The emitting transducer is water coupled at various angles to steel test pieces, the miniature receiving transducer being coupled to an opposite surface. The receiver is fabricated as a needle-like probe using a lead metaniobate disc of diameter 0.3 mm as the active element. The 6 dB bandwidth of the miniature probe ranges from around 0.5 to 7 MHz, which is wide enough to not significantly change the shape of the ultrasonic pulses investigated. To a reasonable approximation, the probe responds to the normal component of the particle velocity of the incoming wave, and can be used to measure both the longitudinal (compression) and transverse (shear) waves.

Chapter 4, Ultrasonic Field Measurement using an EMAT

EMATs are particle velocity sensors, which can be designed to have sensitivity to in-plane and, or out-of-plane ultrasonic displacements, by suitably arranging the magnetic field in the receiving EMATs relative to the orientation of the coil.

Chapter 5, A Model for Ultrasonic Field of a Piezoelectric Transducer

A model has been developed which can be used to calculate the particle velocity waveforms at arbitrary positions in a solid immersed in a fluid when irradiated by a transmitting transducer, launching a short pulse of a longitudinal wave into the fluid. Mode-converted longitudinal and shear waves are generated at the interface between the solid and the fluid. Calculations performed agree well with the results of experimental measurements using a specially-constructed miniature piezoelectric receiving probe. The model constructed has been used to explain the radiation field of a transmitting transducer into an immersed solid and it can be used for the optimal design of a transducer and ultrasonic NDT device in immersion mode that has been widely used for ultrasonic imaging and automatic inspection.

Chapter 6, A Model for EMAT Ultrasonic Field and EMAT Optimization

A model has been developed for the prediction of the transient displacement of a Rayleigh wave generated by an Electromagnetic Acoustic Transducer (EMAT), operating on the Lorentz principle. This model can be used to calculate Rayleigh waves of arbitrary forces. A linear coil and a spiral coil are considered as two examples. Out-of-plane displacement of the Rayleigh wave is measured experimentally using a Michelson laser interferometer. Good agreement is observed between the calculated and the measured results, demonstrating the value of this method. This chapter explains how the Lorentz forces due to the static and dynamic magnetic fields work constructively and destructively, indicating that the orientation of the external magnetic field must be correct to achieve an efficient generation of the Rayleigh wave.

Chapter 7, Application of a Focused Ultrasonic Transducer in Bond Evaluation

The evaluation of weak bonds within an IC package is investigated in this chapter. Samples of IC packaging have been fabricated containing structures of the die (silicon) / die-attach (silver-based adhesive) / lead-frame (copper), which are typically found in IC packaging, and are degraded, to various extents, through thermal cycling to obtain varied levels of bond degradation. Interface reflection

ultrasonic waveforms have been measured using a spherically-focused transducer and C-scan imaging is carried out, with the results explained using an interface spring model.

2.   LITERATURE REVIEW

Ultrasonic testing [1-3] is one of the three main volumetric Non-Destructive Testing (NDT) methods, i.e. ultrasonic testing, radiographic testing and electromagnetic testing.

Industrial Radiography can be performed utilizing either X-rays or gamma rays. Both are forms of electromagnetic radiation. The difference between various forms of electromagnetic energy is related to the wavelength. X and gamma rays have the shortest wavelength and this property leads to the ability to penetrate, travel through, and exit various materials such as carbon steel and other metals.
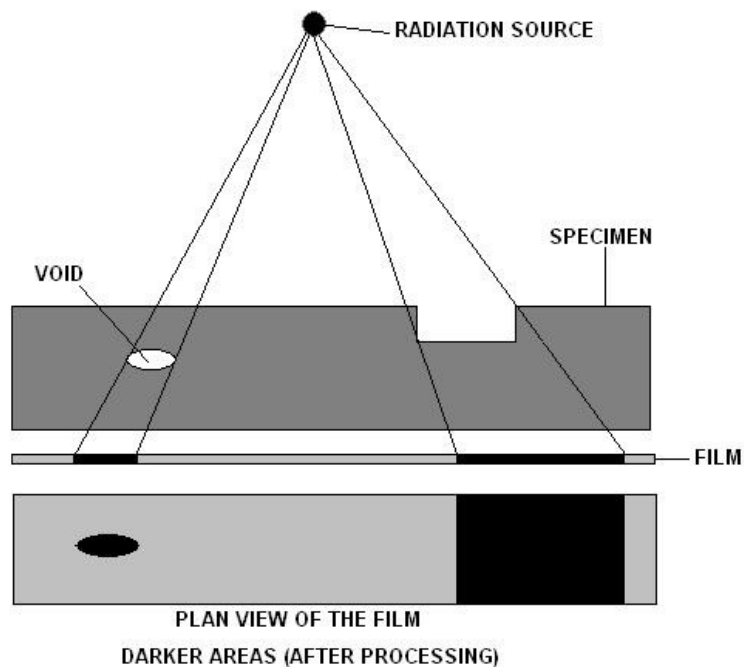
Figure 2.1 Principle of film radiography testing [4]

Eddy current testing is widely used in the aerospace industry and in other manufacturing and service environments that require inspection of thin metal for potential safety-related or quality-related problems. In addition to crack detection in metal sheets and tubing, eddy current can be used for certain metal thickness measurements such as identifying corrosion under aircraft skin, to measure conductivity and monitor the effects of heat treatment, and to determine the thickness of nonconductive coatings over conductive substrates. Both field portable and fixed system instruments are available to meet a wide variety of test needs.

a—The alternating current flowing through the coil at a chosen frequency generates a magnetic field around the coil.

b—When the coil is placed close to an electrically conductive material, eddy current is induced in the material.

c—If a flaw in the conductive material disturbs the eddy current circulation, the magnetic coupling with the probe is changed and a defect signal can be read by measuring the coil impedance variation.

Figure 2.2 Principle of eddy current testing [5]

Ultrasonic waves are generated by an ultrasonic transducer, which propagate in the material to be tested. The ultrasonic waves can be detected either by the same transducer in pulse-echo mode or by other transducer/s in pitch-catch mode.

Ultrasound can be generated by following mechanisms

- Piezoelectricity---Piezoelectric transducer

- Lorentz force---ElectroMagnetic Acoustical Transducer (EMAT)

- Magnetostriction---EMAT

- Ablative regime under optical energy---Laser ultrasound generation

- Thermoelastic regime under optical energy---Laser ultrasound generation

- Capacitance change--- Capacitive Micromachined Ultrasonic Transducer (CMUT)

2.1   Piezoelectric transducers

Piezoelectricity denotes charge accumulation in certain crystals and ceramics in response to applied mechanical stress. Such piezoelectric crystals and ceramics produce stress in response to the applied electric field. The core of a piezoelectric transducer is a piece of polarized piezoelectric material, which converts electrical pulses to mechanical vibrations to generate ultrasound and converts returned mechanical vibrations back into electrical energy in order to detect ultrasound. Today piezoelectric ceramic is most widely technology for ultrasonic transducers.

The centre frequency of a piezoelectric transducer is dependent on the thickness of the piezoelectric element used in the transducer. Its bandwidth is dependent on damping of its backing layers and configuration of its matching layers [6].

Piezoelectric transducers have been used to generate and detect ultrasound in air [7-10], fluid [11-12] and solid [13-15], are the most common transducer for NDE. Generally piezoelectric transducers for NDT operate at low voltage with high mechanical-electric conversion efficiency and are usable up to about $300^{o}C$. But there are some piezoelectric ceramics of high Curie temperature which allows them operating at high temperature but with low mechanical-electric conversion efficiency [16-18].

Single circular crystal probes are most common for NDE, and are explained with rigid circular pistons of thick mode for theoretical prediction of longitudinal wave radiation [19-23]. Shear wave radiation of Y-cut circular crystals has been predicted [24]. Extensive works on the ultrasound field predictions [25-43] and ultrasonic field measurements using miniature piezoelectric transducer, EMAT and laser [44-48] have been published. Effects of damping, active element size, applied electric voltage have been studied [49-51] and defect reflection of ultrasonic waves haven been predicted and observation with miniature piezoelectric transducer [52-54].

2.2   Scanning Acoustic Microscopy

Acoustic microscopy employs very high or ultra-high frequency ultrasound that generally is piezoelectric based and uses lenses to focus ultrasound to the desired shape. In its development history, there are at least following three configurations

- Scanning Acoustic Microscopy (SAM)

  An ultrasound transducer generates ultrasound waves which interact with a suspension of asymmetric particles in a thin fluid layer or with a suspension of tiny latex spheres in a fluid, which produces a visual image.

- Scanning Laser Acoustic Microscopy (SLAM)

An ultrasound transducer generates an ultrasound field whilst a scanning laser system is used to detect the ultrasound field for acoustic microscopy.

- C-mode Scanning Acoustic Microscopy (C-SAM).

  A transducer generates and receives returning ultrasound waves meaning that the acoustic image could easily be constrained to a depth of interest.

Scanning the ultrasonic probes over samples generates visible images of internal features of the samples, including defects such as cracks, delaminations and voids. Because of its very small wavelength of ultrasonic waves and small focused ultrasonic beam spot, it has a very high spatial resolution and can detect a very small defect around a wavelength.

The samples imaged by acoustic microscopes are typically assemblies of one or more solid materials that have at least one surface that is either flat or regularly curved. The depth of interest may involve an internal bond between materials, or a depth at which a defect may occur in a homogeneous material.

Typical applications are [55-76]

- Detection of delamination, such as coating

- Evaluation of bonds, such as Integrated Circuit (IC) packaging

- Failure analysis

- Crack detection

- Characterization of nanostructure

2.3 Capacitive Micro-machined Ultrasonic Transducers (CMUT)

A Capacitive Micro-machined Ultrasonic Transducer (CMUT) is constructed on silicon using micromachining technique as shown in Figure 2.3 [77]. A cavity is formed in a silicon substrate, and a thin layer suspended on the top of the cavity serves as a membrane on which a metalized layer acts an electrode, together with the silicon substrate which serves as a bottom electrode.
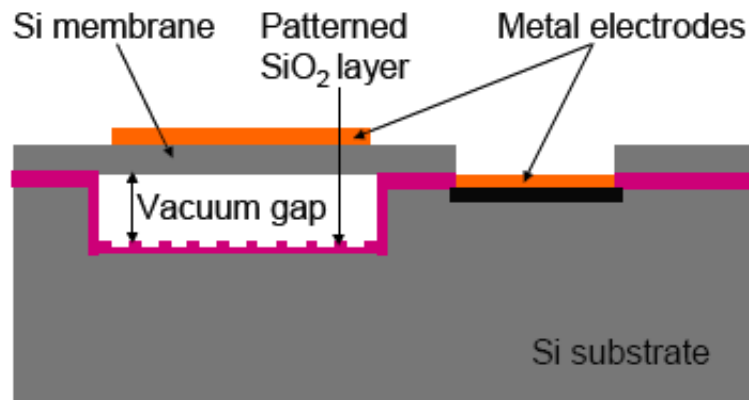
Figure 2.3 Schematic view of a captive Micro-machined ultrasonic transducer.

When an AC signal is applied across the biased electrodes, they vibrate accordingly generating ultrasonic waves in the medium of interest [78]. On the other hand, if ultrasonic waves are applied on the membrane of biased CMUT, it will generate alternating signal as the capacitance of the CMUT is varied. In this way, it works as a receiver of ultrasonic waves.

As CMUTs are micromachined devices, 2D and 3D arrays of transducers can be easily constructed in a small space [79]. The frequency of operation depends on the cell size, and on the stiffness of the material used as a membrane, and a larger

bandwidth can be achieved easily due to its small dimension. As CMUTs are built on silicon, the integration of electronics is relatively easy.

CMUTs are generally used for ultrasonic generation in air and have been modelled and optimised to increase electromechanical transform efficiency [80-84]. CMUTs have been reported for health monitoring [85-87].

2.4   Laser Ultrasonic Generation and Detection

Lasers can be used to generate and detect ultrasonic waves [88-93]. Generation lasers are short pulse (from tens of nanoseconds to femtoseconds) and high peak power lasers and in general a laser is a very strong ultrasonic source and can generate ultrasonic signals orders of magnitude higher than contact piezoelectric transducers. Common lasers used for ultrasound generation are solid state Q-Switched Nd:YAG and gas lasers (CO_2 or Excimers) .

The resulting ultrasonic waves contain bulk longitudinal waves, shear waves and guided waves (Rayleigh waves/surface waves) and their frequency spectrum is determined by the width of laser pulses and material property of the sample.

Laser ultrasound generation is described in two extreme regimes, the ablative regime and thermoelastic regime. In the ablative regime the laser energy is focused onto the surface of the sample which at sufficiently high energy densities will form a plasma. The plasma may consist of the vaporised sample and/or air breakdown depending on the sample and the experimental conditions. There are situations where a strong ablative-like source can be generated in a totally non-destructive way such as the case using a pulsed CO_2 laser to focus onto an aluminium sample. In the thermoelastic regime the laser energy is directed onto the surface of the sample at a sufficiently low energy density to avoid ablation. The laser energy is absorbed within the skin depth of the sample and rapidly heats that small volume of the sample. While there may be no superficial damage to the sample there may be

subsurface damage due to the absorption of laser energy. This is a major drawback when trying to generate on samples like carbon fibre composites where there is high absorption of the laser energy and poor thermal conductivity. However, for most industrial type samples the damage is usually on a microscopic scale and is negligible.
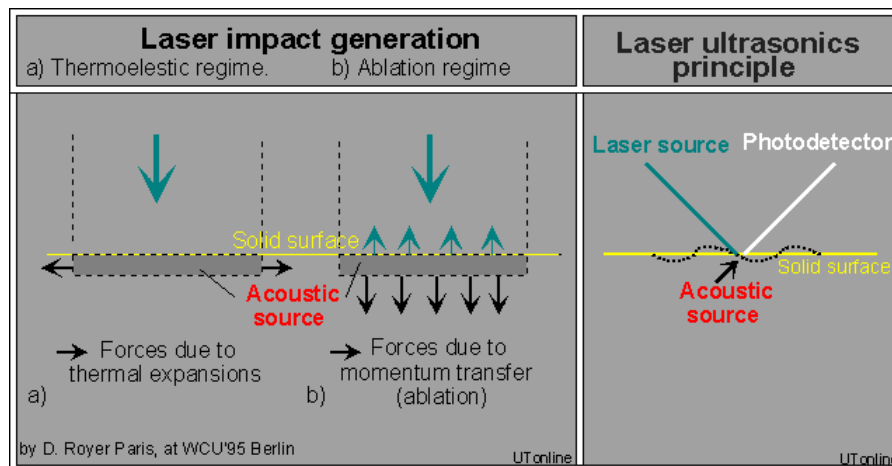
Figure 2.4 Laser ultrasound generation

Common laser detection techniques include: interferometry (homodyne or heterodyne or Fabry–Pérot) and optical beam deflection (Gas-Coupled Laser Acoustic Detection, GCLAD) or knife edge detection.

A Michelson interferometer generally has a larger bandwidth. It can detect displacements down to less than an Angstrom and is relatively insensitive to low frequency background vibration. However, it requires the surface of samples to have high reflectivity and is nearly impossible to set up an automatic alignment for on-line applications. Fabry-Perot interferometers can be used for on-line measurements and will work on surfaces with poor reflectivity. But its bandwidth is limited and the sensitivity is lower than that of the Michelson interferometer. At low

to moderate frequencies (say < 1 GHz) the mechanism for detection is the movement of the surface of the sample, at high frequencies (>1 GHz) other mechanisms may come into play (for instance modulation of the sample refractive index with stress). Optical beam deflection is based on the fact that the ultrasound waves create changes in the air's index of refraction. When the laser encounters these changes, the beam slightly deflects and displaces to a new course. This change is detected and converted to an electrical signal. This enables high sensitivity detection of ultrasound on rough surfaces for frequencies up to 10 MHz.

2.5   Electromagnetic Acoustical Transducers (EMAT)

A transmission EMAT generally contains a coil and external magnetic field provider that can be permanent magnet or a DC driven coil, or a coil only [94-109]. There are two mechanisms to generate waves through magnetic field interaction. One is Lorentz force when the material is conductive. The other is magnetostriction when the material is ferromagnetic.

The AC current in the electric coil generates eddy current on the surface of the material. The eddy current in the magnetic field experiences Lorentz force. In a microscopic view, the Lorentz force is applied on the electrons in the eddy current [101]. In a macroscopic view, the Lorentz force is applied on the surface region of the material due to interaction between electrons and atoms. The distribution of Lorentz force is controlled by the design of the magnet, and design of the electric coil, the properties of the test material, relative position between the transducer and the test part, and the excitation signal for the transducer.

Magnetostriction denotes dimensional change of a ferromagnetic material under a varying externally applied magnetic field. For ultrasonic generation, AC current in the exciting coil induces an AC magnetic field and thus produces dimension changes in a ferromagnetic material. These dimension changes generate ultrasound waves propagating in the material. For ultrasonic detection, incoming ultrasonic

waves cause dimension changes which induce electric current in the material. This electric current is detected by a sensing coil under an external magnetic field.

Generally speaking, EMATs have low electromechanical transform efficiency; therefore probe optimization is crucial to their successful applications [102-107]. EMAT has been used in a broad range of applications including,

- Thickness measurement for various applications

- Flaw detection in steel products

- Plate lamination defect inspection

- Bonded structure lamination detection

- Laser weld inspection for automotive components

- Various weld inspection for coil join, tubes and pipes

- Pipeline in-service inspection

- Rail road and wheel inspection

- Austenitic weld inspection for power industry

- Material characterization

2.6   Summary

Piezoelectric transducers have high transduction efficiency, are currently widely used in NDT, but operate at low temperature. There are piezoelectric ceramics that can operate at high temperature, which have been reported for structural health

monitoring but the transduction efficiency is low. With the use of piezoelectric transducers, ultrasound couplant is required and good surface condition of the test pieces is required for ultrasound propagating to the test pieces. The ultrasonic phased array technique has advanced greatly in recent years and has been increasingly applied for NDT [110-111].

Scanning Acoustical Microscopy uses high frequency ultrasound and requires test pieces to be immersed in fluid as the ultrasonic couplant. Therefore test pieces should be immersed in a scanning tank and its thickness should be small being in the range of millimetres.

EMATs have low transduction efficiency requiring signal processing to improve signal to noise ratio but they request no couplant for testing and can work at high temperature and below couplant freezing temperature [112]. EMATs can operate in non-contact on relatively rough surfaces. EMATs can only work on electrically conductive materials or ferromagnetic materials. Configurations of EMATs for generation of guided waves (Rayleigh waves – surface waves, Lamb waves – plate waves) and horizontal shear (SH) waves are generally simple. EMATs generally have a larger size compared to piezoelectric transducers.

Laser ultrasonic testing is a non-contact technique and the laser is a strong ultrasound source for solid [112]. Laser ultrasound generation does not require a very smooth surface, but for laser ultrasound detection, the laser interferometer technique require a surface of good reflection whilst optical beam deflection technique works on relatively rough surface.

CMUTs are used mainly to generate and measure ultrasound in air, which have been used for structure health monitoring to detect acoustical emission from monitored structures.

2.7   References

1   J A Ogilvy, Theoretical comparison of ultrasonic signal amplitudes from smooth and rough defects, NDT&E International 19 (1986): 371-385.

2   E Marianeschi, T Tili, A note on the smallest defect that can be detected using ultrasonics, NDT International 16 (1983): 75-77.

3   S Hirose, N Kono, and K Nakahata, Numerical simulation of scattered waves from flaws for ultrasonic array transducer, Review of Progress in QNDE, AIP Conf. Proc. 894 (2006): 822-829.

4   https://en.wikipedia.org/wiki/Industrial_radiography.

5   http://www.olympus-ims.com/en/eddycurrenttesting.

6   J P Weight, New transducers for high-resolution ultrasonic testing, NDT International 17 (1984): 3-8.

7   T Gudra, M Pluta, Z Kojro, The measurement and numerical modelling of the diffraction field of a spherical ultrasonic transducer working in the air at the frequency of 1.3 MHz, Ultrasonics 38 (2000):794-798.

8   E Blomme, D Bulcaen, F Declercq, Air-coupled ultrasonic NDE: experiments in the frequency range 750 kHz-2 MHz, NDT & E International 35 (2002): 417-426.

9   G Hayward and A Gachagan, An evaluation of 1-3 connectivity composite transducers for air coupled ultrasonic applications, J. Acoust. Soc. Am. 99 (1996): 2148-2157.

10   M Castaings and P Cawley, The generation, propagation, and detection of Lamb waves in plates using air coupled ultrasonic transducers, J. Acoust. Soc. Am. 100 (1996): 3070-3077.

11   S McLaren and J P Weight, Transmit-receive mode responses from finite☐sized targets in fluid media, J. Acoust. Soc. Am. 82 (1987): 2102-2112.

12   J P Weight, Ultrasonic beam structures in fluid media, J. Acoust. Soc. Am. 76 (1984): 1184-1191.

13   G Canella, The ultrasonic field in water and steel, Non-Destructive Testing 8 (1975): 38-42.

14   A Ilan and J P Weight, The propagation of short pulses of ultrasound from a circular source coupled to an isotropic solid, J. Acoust. Soc. Am. 88 (1990): 1142-1151.

15   J P Weight, A model for the propagation of short pulses of ultrasound in a solid, J. Acoust. Soc. Am. 81 (1987): 815-826.

16   A Baba, C T Searfass and B R Tittmann, High temperature ultrasonic transducer up to 1000°C using lithium niobate single crystal, Appl. Phys. Lett. 97 (2010): 232901.

17   G Canella, F Monti, Ultrasonic inspection of hot thick steel products, NDT International 13 (1980): 10-14.

18   Byoung-Chul Shin, Jeong-Rock Kwon, Ultrasonic transducers for continuous-cast billets, Sensors and Actuators A: Physical 51 (1995): 173-177.

19   H Djelouah and J C Baboux, Transient ultrasonic field radiated by a circular transducer in a solid medium, J. Acoust. Soc. Am. 92 (1992): 2932-2941.

20   J Hayman and J P Weight, Transmission and reception of short ultrasonic pulses by circular and square transducers, J. Acoust. Soc. Am. 66 (1979): 945-951.

21   K Beissner, Some basic relations for ultrasonic fields from circular transducers with a central hole, J. Acoust. Soc. Am. 131 (2012): 620-627.

22   L J Fradkin, A P Kiselev, and E Krylova, The radiating near-field asymptotics of a normal time-harmonic circular ultrasonic transducer in an elastic half-space, J. Acoust. Soc. Am. 104 (1998): 1178-1187.

23   R E Challis, Diffraction phenomena in the field of a circular piezoelectric transducer viewed in the time domain, Ultrasonics 20 (1982): 168-172.

24   A Lhémery, An analytic expression for the transient ultrasonic field radiated by a shear wave transducer in solids, J. Acoust. Soc. Am. 96 (1994): 3787-3791.

25   N Gengembre, A Lhémery, Pencil method in elastodynamics: application to ultrasonic field computation, Ultrasonics 38 (2000): 495-499.

26   Jian X, Weight JP, Grattan KTV, Dixon S, A model for propagation of short pulses of ultrasound in solid immersed in a fluid, Sensors & Actuators: A Physical 133 (2007): 439-446.

27   A R Selfridge, G S Kino, and B. T. Khuri□Yakub, A theory for the radiation pattern of a narrow□strip acoustic transducer, Appl. Phys. Lett. 37 (1980): 35.

28   H Ogi, M Hirao, T Honda, and H Fukuoka, Ultrasonic diffraction from a transducer with arbitrary geometry and strength distribution, J. Acoust. Soc. Am. 98 (1995): 1191-1198.

29   H Djelouah, J C Baboux, M Perdrix, Theoretical and experimental study of the field radiated by ultrasonic focussed transducers, Ultrasonics 29 (1991): 188-200.

30   L W Schmerr, Jr., A Sedov, and T P Lerch, A boundary diffraction wave model for a spherically focused ultrasonic transducer, J. Acoust. Soc. Am. 101 (1997): 1269-1277.

31   K P Richter, R Reibold, W Molkenstruck, Sound field characteristics of ultrasonic composite pulse transducers, Ultrasonics 29 (1991): 76-80

32   D Belgroune, J F Belleval, H Djelouah, A theoretical study of ultrasonic wave transmission through a fluid-solid interface, Ultrasonics 48 (2008): 220-230.

33   G C Low, A simple computer method for predicting the transient response of ultrasonic NDT probes, NDT International 13 (1980): 285-290.

34   D Gridin and L J Fradkin, The high-frequency asymptotic description of pulses radiated by a circular normal transducer into an elastic half-space, J. Acoust. Soc. Am. 104 (1998): 3190-3198

35   D. D. Zakharov and L. Ju. Fradkin, Asymptotic evaluation of the pulse train radiated by an angled beam and fluid coupled rectangular ultrasonic transducer, J. Acoust. Soc. Am. 127 (2010):1267.

36   L J Fradkin, A P Kiselev, and E Krylova, The radiating near-field asymptotics of a normal time-harmonic circular ultrasonic transducer in an elastic half-space, J. Acoust. Soc. Am. 104 (1998): 1178-1187.

37   L J Fradkin and A P Kiselev, The two-component representation of time-harmonic elastic body waves in the high- and intermediate-frequency regimes, J. Acoust. Soc. Am. 101 (1997): 52-65.

38   M C M Bakker and M D Verweij, Experimental validation of two elastodynamic models for the wave field generated by ultrasonic transducers, J. Acoust. Soc. Am. 113 (2003): 1850-1862.

39   David Duxbury, Jonathan Russell, Michael Lowe, The effect of variation in phased array element performance for Non-Destructive Evaluation (NDE), *Ultrasonics* 54, pp 1065-1078.

40   Victor Zernov, Larissa Fradkin, Michel Darmon, A refinement of the Kirchhoff approximation to the scattered elastic fields, *Ultrasonics* 52, pp830-835.

41   Djema Belgroune, Jean François de Belleval, Hakim Djelouah,   A theoretical study of ultrasonic wave transmission through a fluid–solid interface, *Ultrasonics* 48 pp220-230

42   Sylvain Chatillon, Vincent Dorval and Nicolas Leymarie, Semi-analytical methods for the simulation of the ultrasonic nondestructive testing of complex materials , *J. Acoust. Soc. Am*. 138, 2015

43   M. Darmon, V. Dorval, A. Kamta Djakou, L. Fradkin, S. Chatillon, A system model for ultrasonic NDT based on the Physical Theory of Diffraction (PTD), *Ultrasonics* 64, pp 115-127, 2016.

44   Jian X, Weight JP, Grattan KTV, Miniature wideband ultrasonic transducers to measure compression and shear waves in solid, Sensors & Actuators: A. Physical 127 (2006): 13-23.

45   A Erhard, H Fuchs, W Möhrle, P Matscholl, Characterization of sound field parameters of ultrasonic probes using a computer-controlled measurement and data acquisition system, NDT&E International 18 (1985): 359-362.

46   R Reibold, W Molkenstruck, Investigation of pulse-excited hydrophones for ultrasonic field measurements using laser interferometry, Ultrasonics 25 (1987): 114-118.

47   Jian X., S Dixon, K Quirk, K T V Grattan, Electromagnetic Acoustic Transducers for In- and Out-of plane Ultrasonic Wave Detection, Sensors & Actuators A: Physical,148 (2008): 151-156.

48   F D Martin and M A Breazeale, A simple way to eliminate diffraction lobes emitted by ultrasonic transducers, J. Acoust. Soc. Am. 49 (1971): 1668-1669.

49   R H Brittain, J P Weight, Fabrication of non-uniformly excited wide-band ultrasonic transducers, Ultrasonics 25 (1987): 100-106.

50   N D Patel, P S Nicholson, Effect of active diameter and damping on the performance of ultrasonic transducers, Ultrasonics 32 (1994): 99-106.

51   H Khelladi, H Djelouah, The size effects of a rigid reflector in the scattering of transient ultrasonic field, Ultrasonics 37 (2000): 697-702.

52   J P Weight, A model to predict the ultrasonic echo responses of small targets in solids, J. Acoust. Soc. Am. 94 (1993): 514-526.

53   J P Weight and A J Hayman, Observations of the propagation of very short ultrasonic pulses and their reflection by small targets, J. Acoust. Soc. Am. 63 (1978): 396-404.

54   A Doghmane, I Al-Suraihy, I Hadjoub, Z Hadjoub , Acoustic microscopy evaluation of anisotropy effects on elastic properties of Na2CoGeO4 single crystals, IOP Conference Series: Materials Science and Engineering 28 (2012): 012037.

55   D Xiang, Y Qin, F Li, Surface wave acoustic microscopy for rapid non-destructive evaluation of silicon nitride balls, Journal of Nondestructive Evaluation 30 (2011): 273-281.

56   R A Lemons, C F Quate, Acoustic microscope--scanning version, Appl. Phys. Lett. 24 (1974): 163-165.

57   B T Khuri-Yakub, Scanning acoustic microscopy, Ultrasonics 31 (1993): 361-372.

58   B Nongaillard, P Logette, J M Rouvaen, H Saisse, H Fevrier, Acoustic microscopy: a tool for non-destructive evaluation of ceramics, NDT International 19 (1986): 77-82.

59   M Clark, S Sharples, M Somekh, Non-contact acoustic microscopy, Measurement Science and Technology 11 (2000): 1792-1801.

60   E Drescher-Krasicka, T M Moore, C D Hartfield, Scanning acoustic microscopy stress measurements in electronic packaging, AIP Conference Proceedings (1998).

61   A Every, G Briggs, Surface response of a fluid-loaded solid to impulsive line and point forces: Application to scanning acoustic microscopy, Physical Review B 58 (1998): 1601-1612.

62   J Kushibiki, T Okuzawa, J Hirohashi, Y Ohashi, Line-focus-beam acoustic microscopy characterization of optical-grade LiTaO single crystals, Journal of Applied Physics (2000): doi:10.1063/1.373083.

63   A Tourlog, W Li, J D Achenbach, Line☐focus acoustic microscopy measurements of elastic constants for materials with high acoustic velocities, Applied Physics Letters

64   S Parthasarathi, B R Tittmann, M Nishida, Characterization of film interface integrity through scanning acoustic microscopy, Surface and Coatings Technology 105 (1998): 1-7.

65   Y Lee, J O Kim, J D Achenbach, Measurement of stresses by line-focus acoustic microscopy, Ultrasonics 32 (1994): 359-365.

66   R G Wilson, R D Weglein, Acoustic microscopy of materials and surface layers, Journal of Applied Physics (1984).

67   R D Weglein, Acoustic microscopy of curved surfaces, Applied Physics
        Letters (1981): doi:10.1063/1.92436.

68   V B Jipson, Acoustic microscopy of interior planes, Applied Physics
        Letters (1979): doi:10.1063/1.91133.

69   Jian X, Guo N, Dixon S, Grattan KTV, Ultrasonic Weak Bond Evaluation
        in IC Packaging , Meas. Sci.& Techno. 17 (2006): 2637-2642.

70   I Alig, M Bargmann, H Oehler, D Lellinger, M Wanner, D Koch,
        Investigation of delamination mechanisms in polymer coatings by scanning
        acoustic microscopy, Journal of Physics D: Applied Physics 44 (2011):
        034009.

71   B Derby, G A D Briggs, E R Wallach, Non-destructive testing and acoustic
        microscopy of diffusion bonds, Journal of Materials Science 18 (1983):
        2345-2353.

72   S Brand, P Czurratis, P Hoffrogge, D Temple, D Malta, J Reed, M Petzold,
        Extending acoustic microscopy for comprehensive failure analysis
        applications, Journal of Materials Science: Materials in Electronics 22
        (2011): 1580-1593.

73   V M Prokhorov, G L Pivovarov, Detection of internal cracks and
        ultrasound characterization of nanostructured Bi 2 Te 3 -based
        thermoelectrics via acoustic microscopy, Ultrasonics 51 (2011): 715-718.

74   T Mihara, G Suzuki, A Harazono, T Ikuno, Fatigue damage monitoring of
        round shape specimen by acoustic microscopy, NDT & E International 32
        (1999): 161-166.

75   W Lawton, J Barrett, Characterisation of chip-on-board and flip chip
        packaging technologies by acoustic microscopy, Microelectronics
        Reliability 36 (1996): 1803-1806.

76   J Z Pan, P J Jenkins, E R Rios, K J Miller, Detecting small fatigue cracks by acoustic microscopy, Fatigue & Fracture of Engineering Materials and Structures 16 (1993): 1329-1337.

77   Xuefeng Wang et al, MEMS 2008, Tucson, USA, January 13-17, 2008.

78   D W Schindel and D A Hutchins, The capacitance transducer as a standard ultrasonic source in solids, J. Acoust. Soc. Am. 97 (1995): 1650-1659.

79   Oralkan, A S Ergun, J A Johnson, M Karaman, U Demirci, K Kaviani, T H Lee, and B T Khuri-Yakub, Capacitive Micromachined Ultrasonic Transducers: Next-Generation Arrays for Acoustic Imaging? IEEE UFFC 49 (2002): 1956-1610.

80   J S McIntosh, A Neild, D A Hutchins, D R Billson, R A Noble, R Davies, Modelling of the radiated field from multi-element capacitive micromachined ultrasonic transducers, Ultrasonics 42 (2004): 447-452.

81   Seung-Mok Lee, Bu-sang Cha, and Masanori Okuyama, The influence of acoustic damping on the transformation efficiency of capacitive micromachined ultrasonic transducer in air, J. Appl. Phys. 108 (2010): 074512.

82   A Caronti, R Carotenuto, and M Pappalardo, Electromechanical coupling factor of capacitive micromachined ultrasonic transducers, J. Acoust. Soc. Am. 113 (2003): 279-288.

83   G Bashford, D W Schindel, D A Hutchins, and W M D Wright, Field characterization of an air-coupled micromachined ultrasonic capacitance transducer, J. Acoust. Soc. Am. 101 (1997): 315-322.

84   D A Hutchins, J S McIntosh, A Neild, D R Billson, and R A Noble, Radiated fields of capacitive micromachined ultrasonic transducers in air, J. Acoust. Soc. Am. 114 (2003): 1435.

85   D W Schindel, Ultrasonic imaging of solid surfaces using a focussed air-coupled capacitance transducer, Ultrasonics 35 (1998): 587-594.

86   Hutchins DA, Billson DR, Bradley RJ, Ho KS, Structural health monitoring using polymer-based capacitive micromachined ultrasonic transducers (CMUTs), Ultrasonics 51(2011):870-877.

87   C Biateau, B Hosten, and D Roziere, Measurement of air-coupled transducer characteristics for ultrasonic non-destructive evaluation, Review of Progress in QNDE, AIP Conf. Proc. 615 (2001): 921-928.

88   C.B. Scruby and L.E. Drain, Laser Ultrasonics, (Adam Hilger: Bristol), 1990.

89   Jian X, Fan Y, Edwards RS and Dixon S, Surface-breaking crack gauging with the use of laser-generated Rayleigh waves, J. Appl Phys. 100 (2006): 064907.

90   D A Hutchins and D. E. Wilkins, Polarized shear waves using laser line sources and electromagnetic acoustic transducer detection, Appl. Phys. Lett. 47 (1985): 789.

91   S E Burrows, B Dutton, S Dixon, Laser generation of lamb waves for defect detection: Experimental methods and finite element modelling, IEEE UFFC 59 (2012): 82 - 89.

92   Jian X, Dixon S, Guo N, Edwards RS, Pulsed Rayleigh Wave Interaction with Surface Cracks, J. Appl. Phys 101 (2007): 064906.

93   Jian X, Baillie I, Dixon S, Steel Billet Inspection using Laser-EMAT System, J Physics D Applied Physics 40 (2007): 1501-1506.

94   R Bruce Thompson, Generation of horizontally polarized shear waves in ferromagnetic materials using magnetostrictively coupled meander coil electromagnetic transducers, Appl. Phys. Lett. 34 (1979): 175.

95   D A Hutchins, D. E. Wilkins, and G. Luke, Electromagnetic acoustic transducers as wideband velocity sensors, Appl. Phys. Lett. 46 (1985): 634.

96   Dirk Rueter, Tino Morgenstern, Ultrasound generation with high power and coil only EMAT concepts, Ultrasonics 54, pp 2141-2150.

97   P.A. Petcher, S.E. Burrows, S. Dixon, Shear horizontal (SH) ultrasound wave propagation around smooth corners, Ultrasonics 54, pp 997-1004

98   Pol Grasland-Mongrain, Jean-Martial Mari, Bruno Gilles, Jean-Yves Chapelon and Cyril Lafon, Electromagnetic tomographic ultrasonic sensor, J. Acoust. Soc. Am. 131, 2012

99   Pol Grasland-Mongrain, Jean-Martial Mari, Bruno Gilles and Cyril Lafon, Electromagnetic hydrophone for high-intensity focused ultrasound measurement, J. Acoust. Soc. Am. 133, 2013

100   Pol Grasland-Mongrain, Bruno Gilles, Jean-Martial Mari, Benjamin Roussel, Adrien Poizat, Jean-Yves Chapelon and Cyril Lafon, Ultrasound velocity mapping with Lorentz force hydrophone, J. Acoust. Soc. Am. 134, 2013

101   Hoe Woong Kim, Joo Kyung Lee, Yoon Young Kim, Circumferential phased array of shear-horizontal wave magnetostrictive patch transducers for pipe inspection, Ultrasonics 54, pp 423-431.

102   Jian X, S Dixon, Edwards RS, Reed J, Coupling mechanism of electromagnetic acoustical transducers for ultrasonic generation, J. Acoust. Soc. Am. 119 (2006): 2693-2701.

103   R Ribichini, F Cegla, P B Nagy, and P Cawley, Study and comparison of different EMAT configurations for SH wave inspection, IEEE UFFC 58 (2011): 2571-2581.

104   X Jian, S Dixon, R Edwards, K Quirk, and I Baillie, Effect on ultrasonic generation of a backplate in electromagnetic acoustic transducers, J. Appl. Phys. 102 (2007): 024909.

105   Jian X, Dixon S, Enhancement of EMAT and Eddy Current using a Ferrite Back-Plate, Sensors & Actuators: A Physical, 136 (2007): 132-136.

106   Jian X, Dixon S, Grattan KTV, Edwards RS, A Model for Pulsed Rayleigh Wave & Optimal EMAT Design, Sensors & Actuators: A. Physical 128 (2006): 296-304.

107   H Ogi, M Hirao, and T Ohtani, Line-focusing of ultrasonic SV wave by electromagnetic acoustic transducer, J. Acoust. Soc. Am. 103 (1998): 2411-2415.

108   X Jian, S Dixon, I Baillie, R S Edwards, J Morrison, and Y Fan, Shear wave generation using a spiral electromagnetic acoustic transducer, Appl. Phys. Lett. 89 (2006): 244106.

109   X Jian, S Dixon, I Baillie, R Edwards and J Morrison, Integrity evaluation of steel products using EMATs, J. Phys. D: Appl. Phys. 40 (2007) : 300–304.

110   R A Roberts, Efficient design of ultrasonic phased array transducer surface geometry, Review of Progress in QNDE, AIP Conf. Proc. 820 (2005): 797-804.

111   T E Michaels and J E Michaels, Sparse ultrasonic transducer array for structural health monitoring, Review of Progress in QNDE, AIP Conf. Proc. 700 (2003): 1468-1475.

112   R J Dewhurst, C E Edwards, A D W McKie, S B Palmer, Comparative study of wide-band ultrasonic transducer, Ultrasonics 25 (1987): 315-321.

3. ULTRASONIC FIELD MEASUREMENT USING A MINIATURE PIEZOELECTRONIC TRANSDUCER

3.1 Summary

This chapter reports on the characterization of specially developed miniature ultrasonic transducers as receivers directly-coupled to a solid surface, to make field point measurements of the ultrasonic waves propagating from a pulsed transducer. The emitting transducer is water coupled at various angles to steel test pieces, the miniature receiving transducer being coupled to an opposite surface. The receiver is fabricated as a needle-like probe using a lead metaniobate disc of diameter 0.3 mm as the active element. The 6 dB bandwidth of the miniature probe ranges from around 0.5 to 7 MHz, which is wide enough not significantly to change the shape of the ultrasonic pulses investigated. To a reasonable approximation, the probe responds to the normal component of the particle velocity of the incoming wave, and can be used to measure both the longitudinal (compression) and transverse (shear) waves. The measurement results obtained compare well to the results of calculations made using theoretical models recently developed by the authors.

3.2 Introduction

No two piezoelectric transducer designs are identical in terms of their frequency range, beam propagation characteristics and directionality. The shape, dimensions, backing and matching of the transducer to the pulse generator together play a major role in the generation of the ultrasonic waves. Furthermore, the quantitative interpretation of pulse echo data obtained when such transducers are used in non-destructive evaluation (NDE) requires a complete knowledge of the ultrasonic field transmitted. There are many ways to measure pulsed ultrasonic fields, including

direct measurements using miniature piezoelectric transducers and electromagnetic acoustic transducers (EMATs) or techniques using optical interferometry [1-17, 19]. In this chapter a miniature piezoelectric transducer is used to measure the pulsed field in solid immersed in fluid.

In a fluid, the ultrasonic field generated by a circular piezoelectric transducer can be described in terms of a combination of locally plane waves that radiate in the geometric region straight ahead of the active transducer element and edge waves radiating from the rim of the element. These "diffraction effects" have been investigated using miniature piezoelectric probes [1-3] or by the use of optical interferometry methods [4-6]. When a piezoelectric transducer is directly mounted onto a solid material, the ultrasonic field includes locally plane longitudinal waves, edge longitudinal waves and mode-converted edge shear waves [7, 8]. This situation has been studied using miniature piezoelectric probes [7, 8], using EMATs on a metal [9-14] and optical interferometers [11-13, 15, 16]. An EMAT detector measures particle velocity. By careful design, in-plane or out-of-plane (or both) velocities can be chosen for detection [11-13]. Thus, both longitudinal and shear waves can be detected. EMATs operate in a non-contact way and can cope with surfaces less smooth than required for optical methods [13]. The main disadvantages of an EMAT detector are its lower sensitivity compared to a piezoelectric device and it is not straightforward to miniaturise the device to operate as a point sensor for the range of wavelengths of interest here. The optical interferometer can measure the true normal displacement of the solid surface with a resolution in the order of nanometres, but it is more complex than the other methods and requires an optically flat surface.

Although the miniature probes described here have long been used to make field-point measurements of the pulsed ultrasonic field in fluids [3], their use [7, 8, 17] directly coupled to a solid surface has not been fully investigated. In carrying out ultrasonic NDE of solid materials, test pieces are often immersed in water to aid coupling of the ultrasonic waves, especially to angled surfaces. Here the construction of a simple miniature piezoelectric transducer is briefly reviewed and its use to measure the complicated ultrasonic field generated within such a test piece is discussed.

This chapter is organized as follows: the section of Ultrasonic Field in a Solid gives a brief review of the pulsed ultrasonic field in solids. The Miniature Probes section and the Response of Miniature Probes section discuss the construction and response of the miniature receiving probe. The section of Measurement Set-up describes the measurement equipment and the experimental set-ups. Results obtained to characterise the probe and demonstrate its use to measure field point waveforms are given in the section of Results. Measurements of the refraction coefficients of locally plane waves are included to investigate the ability of the probe to measure both longitudinal and shear waves. The results of such measurements are compared with well-known calculated coefficients [18]. Experimental measurements of field point waveforms made using the miniature probe are compared with theoretical calculations obtained using a recently developed model [19] and the implications for NDE are discussed. The conclusions are summarised in last section.

3.3   Ultrasonic Field in a Solid

In order to interpret field-point waveforms measured with the miniature probe, it is necessary to briefly discuss further the nature of the ultrasonic field in a solid. For the case of direct coupling of the transducer to a solid, the field has been explained in terms of a locally plane longitudinal wave and a spreading edge longitudinal wave that partially mode converts into a shear edge wave [7, 8]. Throughout the remainder of this chapter,it is assumed the "plane" waves radiated by a finite transducer are not infinite plane waves and drop the term "locally" plane.

 A model of the plane and edge wave has been developed to explain the further complication of the ultrasonic field that arises if both the ultrasonic transducer and the test solid are immersed in a fluid, the transducer being aligned at arbitrary angle (in one plane) to the solid surface. Depending on the angle of incidence, both the incoming plane and edge longitudinal waves in the fluid, can give rise to corresponding plane and edge shear waves in the solid.

Consider first a circular emitting transducer aligned normally to the surface of a solid half space, as shown in Figure 3.1. The plane wave front is disk shaped and propagates within the geometric region straight ahead of the transducer both within the fluid and the solid. In two dimensions this is represented as the bold line *AB*. Since the plane longitudinal waves are incident normally, no mode-converted plane shear waves are produced in the solid. The wave front of the edge waves is toroidal in the fluid. For clarity the edge wave front is not shown but ray paths are shown by the lines *AP* and *BP*. Point *P* in the solid lies on the axis of the transducer. Due to the fact that the propagation velocities of the longitudinal and the shear waves are different, the refracted longitudinal ray (solid line) and the refracted shear ray (dotted line) propagate along different paths, the angle of refraction being given by Snell's Law. At point *P*, the plane longitudinal ray from point *C*, the refracted longitudinal and the mode converted shear edge wave may all be detected, the arrival time of each ray depending on both the path and the velocity differences. Since the path distance to point *P* on the axis from any edge point around the rim of the transducer is the same, the edge longitudinal wave contributions from each element of the rim arrive together at time t_{ec}. Similarly, the shear edge wave contributions from around the rim arrive together, but at a later time t_{es}. Thus, as a result of this circular symmetry in the plane parallel to the emitter surface, both longitudinal and shear the edge waves are focused on axis. Off axis, the edge wave contributions quickly drop off in amplitude and will be "smeared out" since the contributions from each element of the rim arrive at *P* at different times.
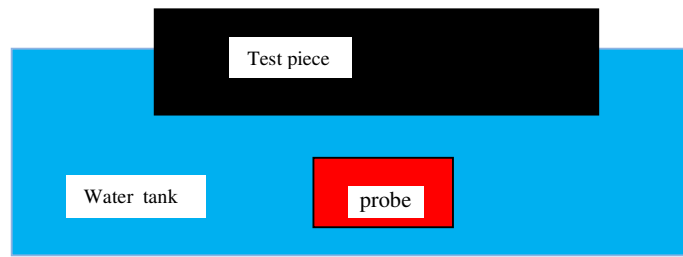
(a)
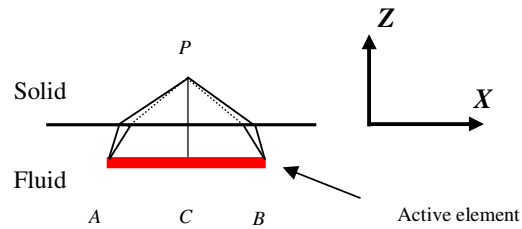
(b)

Figure 3.1 Schematic view of measurement setup (a) and ultrasound propagation paths (b) to ultrasonic field point P of plane compression wave (from active element centre C) and edge waves (from active element edges A and B) generated by a circular piezoelectric transducer water coupled at normal incidence to a solid. Note C is the centre of the active element.

Consider now that the (circular) emitting transducer is angled to the solid surface, as shown in Figure 3.2. Now the beam within the solid can be "split" into two as a result of refraction and mode conversion. The longitudinal- and shear-wave beams propagate in different directions and are described by Snell's Law. Depending on the angle of incidence to the solid surface, a mode converted plane shear wave can exist within the solid, in addition to the shear edge wave. The plane longitudinal and shear waves have an elliptic cross section and there is no longer a single axis for either mode of propagation around which the edge waves exhibit circular symmetry. As in Figure 3.1, for clarity in Figure 3.2 wave fronts are not shown in the solid, but consider ray paths for elements of the various radiating waves. Consider the arrival of waves at a point P that lies within both the plane longitudinal and plane shear beams. First, taking ray paths of elements of the plane waves within the solid, the longitudinal wave ray from point C (solid line, ray CP) arrives at P before the shear wave from point D (dotted line in the solid, ray DP), since in steel, the propagation velocity of the shear wave is around half that of the longitudinal wave. Considering now points on the rim of the source; the propagation time to P from each element of the rim (A and B, for instance) is different and so the edge longitudinal waves are not a maximum at P. However, although there is no circular symmetry, the maximum amplitude of the edge longitudinal-wave pulse can be found by translating the transducer in the X direction (- X direction for the particular position of P shown). For convenience this is referred as the "focus" position. Similarly the mode converted shear edge wave may be brought to a maximum at P by further translation of the transducer. Again the longitudinal and shear field-point pulses arising from these "focussed" rays arrive at P at different times. At points within the beams where the edge waves are not focused, the corresponding edge pulse contributions will be quickly "smeared" out.

(a)

(b)
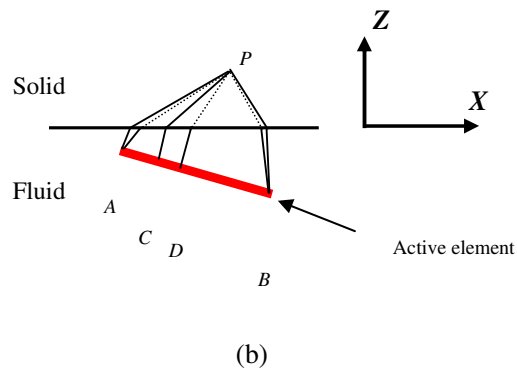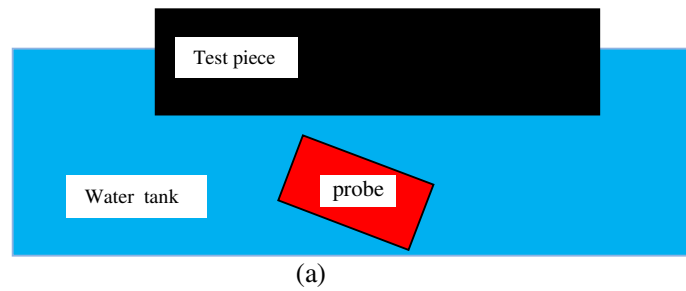
Figure 3.2 Schematic view of measurement setup (a) and ultrasound propagation paths (b) to ultrasonic field point P of plane (plane compression wave from C and plane shear wave from D) and edge waves (edge waves from A and B) generated by a circular piezoelectric transducer water coupled at oblique incidence to a solid.

3.4   Miniature Probes

In order to make accurate field point measurements of pulsed ultrasonic fields, the diameter of the active element of the receiving probe should be smaller than the wavelengths of the incoming ultrasonic waves and its frequency bandwidth must be at least that of the ultrasonic waves.

Currently, a number of types of miniature transducers are commercially available. But most of these are too large to act as point-like transducers for wavelengths used in wideband non-destructive evaluation. For instance, the Panametrics XMS transducer series typically has a diameter 3 mm. Commercially available wideband transmitting transducers used in NDE can give pulse shapes with spectra ranging from around 0.5 MHz to 5 MHz, with wavelengths in water ranging from 3mm to 0.3mm. Corresponding wavelengths in steel are around 12mm to 1.2mm for longitudinal waves and 6mm to 0.6mm for shear waves. Thus for such pulses in steel, the active diameter for an effective miniature probe should be smaller than 0.6mm, but a compromise between size and sensitivity must be made. Other practical considerations for the current application include a design that must allow point-like coupling to a solid surface and the requirement to minimise unwanted modes of vibration in the probe tip.

Recent research into lead metaniobate (PMN) based electrostrictive piezoelectric materials has led to the creation of probe material compositions with strain sensitivity significantly higher than those of lead zirconium titanate (PZT) ceramics, together with lower levels of unwanted radial modes of vibration. For these reasons PMN has been used in the fabrication of the miniature probes used here.

~1.5mm

PMN disc

Conductive
needle

Non-conductive
layer

Conductive
layer

Non-conductive
cover

BNC connector
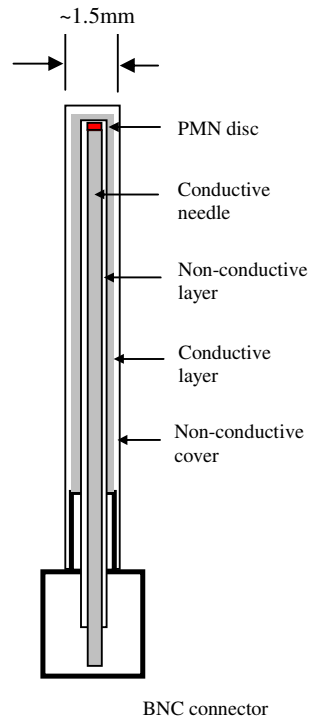
Figure 3.3 Schematic view of miniature probe.

A schematic representation showing the structure of the miniature probe is given in Figure 3.3. In creating it, a PMN disc of around 0.5 mm in diameter and thickness 0.2mm was bonded to the tip of a stainless steel needle of similar diameter and length around 50mm, using electrically conducting epoxy. The needle acts as a heavily damping backing material as well as a means to provide electrical connection to the back face of the element. Then the needle and element were abraded using fine polish paper to reduce the diameter of the tip assembly to around 0.3mm. The needle was bonded to the inner terminal of a BNC coaxial plug, which provides a convenient means to support the probe and allows direct connection to a head amplifier. The front face of the element was abraded to reduce the thickness of the element to around 0.15mm. The half-wave resonant frequency of such a PMN disc is around 14MHz, but the heavily damping, needle-like backing greatly damps this and other unwanted modes of reverberation with the probe element. To electrically isolate the needle and back face of the element from the front face, they were together coated with an electrically insulating layer that also provides further acoustic damping. Again the tip was abraded to expose the front face of the PMN element and the whole assembly is coated with a conducting layer to provide connection of the front face to the BNC outer "earth" electrode. Finally, the probe was encapsulated in a further coat to protect it and provide further acoustic damping, care being taken to keep the thickness over the front face small enough to avoid unwanted loss of sensitivity due to destructive interference.

The final dimensions of the probe element are chosen to provide a compromise between, size, sensitivity, bandwidth and dynamic range, the latter being defined as the ratio between the wanted outputs from a received pulse to the unwanted "ripples" generated within the probe itself. The significance of such ripples on the measurements to be made is discussed later in Section V part C. The small size of the active element within the probe leads to a high electrical source impedance and to avoid loss of signal due to capacitive potential division in connecting cables, the probe is directly plugged in to a miniature, submersible, head amplifier (gain 10dB, bandwidth 1 kHz to 50 MHz).

3.5 Response of the Miniature Probe

As is well known, in the case of longitudinal waves, the particles vibrate in the direction of wave propagation, whereas with shear waves particles vibrate perpendicularly to the direction of propagation, as shown in Figure 3.4. The unit normal vectors for the particle velocity for the longitudinal and shear waves are given by

$$\vec{n}_l = \begin{bmatrix} \sin\theta_l \cos\varphi_l & \sin\theta_l \sin\varphi_l & \cos\theta_l \end{bmatrix} \tag{3.1}$$

$$\vec{n}_s = \begin{bmatrix} \sin(\theta_s + \frac{\pi}{2})\cos\varphi_s & \sin(\theta_s + \frac{\pi}{2})\sin\varphi_s & \cos(\theta_s + \frac{\pi}{2}) \end{bmatrix} \tag{3.2}$$

where θ_l and φ_l are the angles of the propagation direction of longitudinal wave with respect to the Z and X axes respectively; similarly, θ_s and φ_s are the corresponding angles of the shear waves.

The unit direction vector of the miniature probe is given by

$$\vec{n}_p = \begin{bmatrix} \sin\theta_p \cos\varphi_p & \sin\theta_p \sin\varphi_p & \cos\theta_p \end{bmatrix} \tag{3.3}$$

where θ_p and φ_p are the angles of the miniature probe with the Z and X axes respectively.

The particle velocity can be decomposed into two components, these being the normal and perpendicular components to the receiving miniature probe. The normal velocity components for the longitudinal and the shear waves are given respectively by

$$u_{\ln} = u_l(t)\left(\vec{n}_l \cdot \vec{n}_p\right) \tag{3.4}$$

$$u_{sn} = u_s(t)\left(\vec{n}_l \cdot \vec{n}_p\right). \tag{3.5}$$

Normal to the receiving Miniature probe

v_{ln}

v_l

v_{sn}

v_s

Vibration of longitudinal waves along wave propagation direction

Vibration of shear Waves perpendicular to wave propagation direction
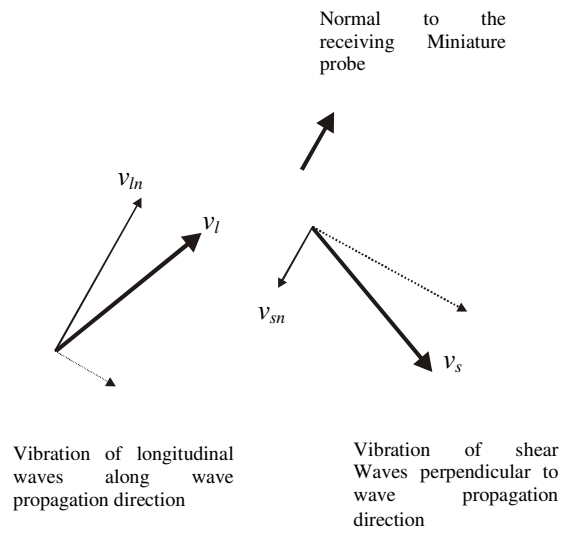
Figure 3.4 Decomposition of particle velocity into normal and perpendicular components with respect to the receiving miniature probe

The response of the miniature probe is to be measured when mounted directly on a solid surface. In doing so, it is assumed that the miniature probe responds to the normal particle velocity components. Therefore, the voltage detected by the miniature probe is given by

$$V_l = \eta u_{\mathrm{ln}} \tag{3.6}$$

$$V_s = \eta u_{s\mathrm{n}} \tag{3.7}$$

where η is a constant related to the efficiency of the mechanical-electrical transformation and the coupling condition between the miniature probe and the steel pieces. It is not straightforward to determine η and we do not attempt here to make absolute measurement of particle velocities. However, providing that experimental conditions can be designed to minimise variations in η, the proportional relationships in Equations 3.6 & 3.7 allows comparison of the shape of measured field-point waveforms with calculated results for u_{ln} and u_{sn} [19].

3.6   Measurement Set-up

Two main experimental set-ups have been used to obtain the results given later in this chapter. The first of these, given in Figure 3.5, shows the system used both to characterise the action of the miniature probe and to make measurements of field-point waveforms that illustrate the diffraction effects mention above. Figure 3.6 shows a similar arrangement, but with a wedge-shaped test piece designed to demonstrate directly the validity of the main assumption made when quantifying the response of the miniature probe, namely that it responds to the normal component of the incoming waves.
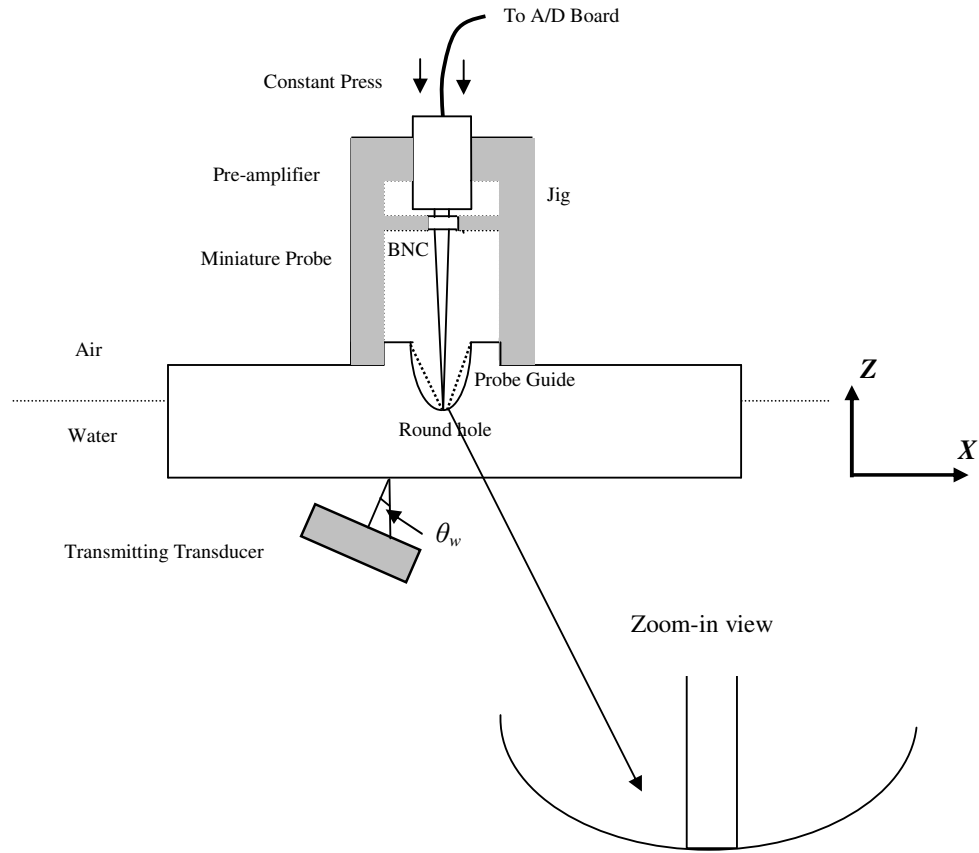
Figure 3.5 Measurement set-up with the miniature probe normal to the water/solid interface. θ_w is the incident angle to the water/steel interface
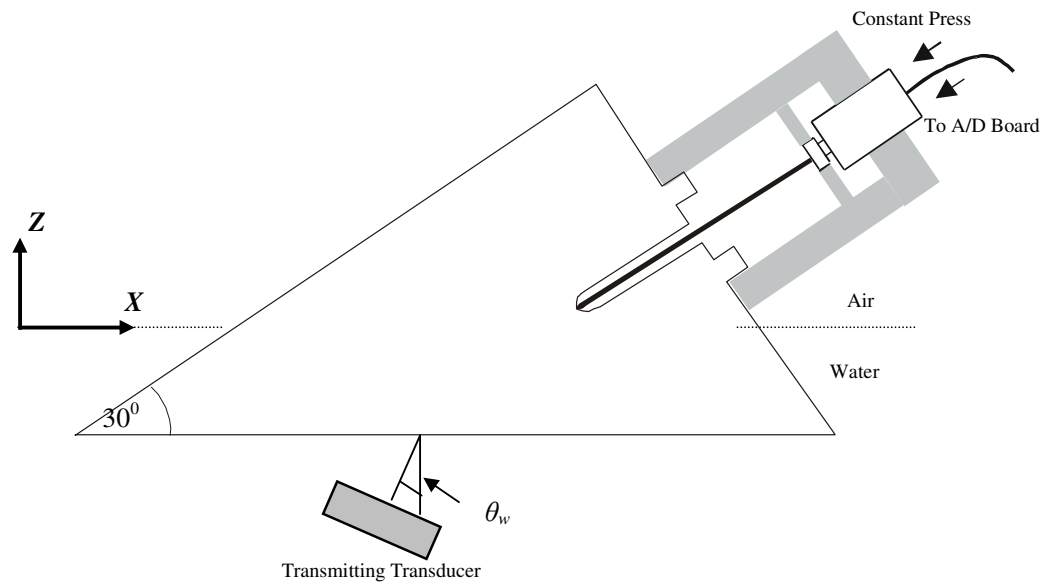
Figure 3.6 Measurement set-up with the miniature probe at 60 degrees to the water/steel interface. θ_w is the incident angle to the water/steel interface

In Figure 3.5, the test piece with the miniature probe and head amplifier mounted rests on a support immersed in water and the transmitting transducer is held within a scanning head that can be translated in the X and Z directions and angled to vary the angle between the normal of the emitting transducer and the normal of the bottom surface of the steel test piece. Throughout, θ_w is referred as the "incident angle in water". Four sample, of mild steel (mass density 7800kg/m^3 and phase velocity of longitudinal and shear waves respectively of 5961m/s and 3211m/s) of cylindrical shape of diameter 250 mm and of thicknesses 10, 15 20 and 25 mm were used. The thickness is measured from the bottom of the round hole where the receiving miniature probe is coupled to the flat surface to which to the incoming ultrasonic beam is directed.

The miniature probe and head amplifier are mounted within a custom-built jig designed to maintain constant coupling conditions between the probe and the surface of the test piece. The round-bottomed hole is incorporated to minimise problems due to multiple reverberations of the incoming ultrasonic wave between the parallel top and bottom surfaces. Since in general both longitudinal and shear waves can propagate in the solid test piece, multiple reflections can lead to overlapping echoes that seriously confuse the pulses to be measured. The bottom of the round hole is locally flat over the dimensions of the miniature probe and parallel to the surface of the sample. A plastic guide is used to ensure that the probe tip is centralised within the round hole. Once set up, the miniature probe in its jig is not disturbed throughout a series of measurements, the position of the probe within the beam being changed by translating and angling only the emitting transducer.

Prior to each experimental run, the support holding the test piece was adjusted to be orthogonal to the scanning head holding the emitting transducer and the direction of the transmitter was adjusted in two planes to obtain a maximum ultrasonic echo after reflection from the flat surface of the test piece. This ensures normal alignment of the emitter is maintained when it is translated in the X direction. All subsequent angular adjustments of the emitting transducer are made in the ZX plane. The scanning tank used provides digital read outs of the position and angle of the scanning head to accuracies of + or - 0.2mm and + or - 0.1 degree, respectively.

The emitting transducer is a wideband, heavily-damped Panametrics transducer incorporating a PMN element of diameter 19 mm and centre frequency 5 MHz. The transducer is excited by a unidirectional electrical pulse of amplitude 600 V, a level typical of those in NDE pulse-echo applications. Although much smaller excitation voltages could be used in the current work, eventually at around 50V, the ultrasonic amplitude is so small that signal-averaging techniques are required to recover signals from random electronic noise. The width of the excitation pulse and its rise and fall times are chosen to generate a simple ultrasonic pulse shape from the Panametrics transducer. In this way locally plane ultrasonic pulses were generated which approximate to one cycle at 3 MHz. The corresponding centre frequency wavelengths of such pulses are 1 and 2mm, for the shear and longitudinal waves, respectively. The pulses received by the miniature probe are amplified by the head amp and captured by an 8-bit analogue to digital converter with a sampling rate of 100 MHz, prior to storage on a PC.

The set-up using the wedge-shaped test piece is shown in Figure 3.6. This test piece was designed to obtain the response of the miniature probe to shear waves arriving with a range of propagation directions centralised on the normal to the measurement surface. For the sound velocities encountered in this investigation, a wedge angle of 30° was considered. Such an arrangement allows to test the hypothesis that the probe responds to the normal component of the incoming waves. A guide was incorporated around the probe tip to ensure that it is mounted centrally within the round-bottomed hole. As before, once set up the miniature probe/head amplifier jig was not disturbed throughout each experimental run.

3.7   Results

3.7.1   Frequency response of the miniature probe

The frequency response of the probe was measured by using it to receive a short pulse approximating to a single cycle at 3 MHz generated from a suitably excited wideband Panametrics transducer of diameter 19mm. Both the emitter and the miniature probe are immersed in water. The Panametrics transducer was first used as both emitter and receiver to receive a pulse after reflection from a normally aligned flat surface at a range of 20 mm. Since on reception the Panametrics transducer integrates over its active area, the output arising from reception at normal incidence of the reflected plane wave swamps that due to the spreading edge wave and the output appears as a single cycle similar in form to the radiated plane wave pulse. A Fourier transform of this pulse provides a "reference" spectrum. The same pulse from the same transmitter was then received by a miniature probe, at the same range as the flat surface, the probe being positioned on the axis of the emitting transducer. Since the probe acts as a point-like receiver, its output shows the edge wave components and as is known, for the case of an ideal circular emitter, the axial edge wave component has equal amplitude to the plane wave radiated [17,18]. At a range of 20 mm and for a 19 mm diameter emitter radiating a plane wave pulse of one cycle at 5MHz, the plane and edge wave pulses as received by the miniature probe are time separated [18]. Therefore, it is possible to measure the frequency response for just the plane wave component by taking the Fourier transform of just this portion of the overall output. In this way recording interference effects was avoided in the measured spectrum that are due to diffraction effects and not to the frequency response of the miniature probe itself. Figure 3.7 shows the spectrum of the plane wave pulse as received by a miniature probe, after deconvolution to compensate for the band limited nature of the reference pulse. The frequency response thus obtained is shown in Figure 3.7, together with a plot of the frequency spectrum of the plane wave component of the pulse radiated. Note that, for an ideal, circular piston source, the frequency spectrum of the axial edge wave component should be identical [1-3, 7, 8]. From Figure 3.7 it is concluded that the frequency

bandwidth of the miniature probe is adequate to measure the true shape of the plane- and edge-wave pulses considered here.
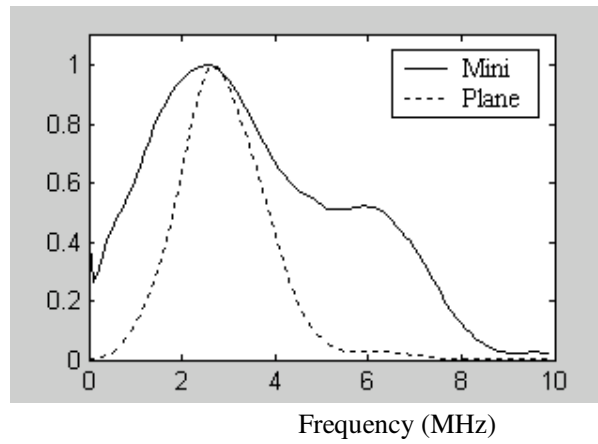
Frequency (MHz)

Figure 3.7 Normalized frequency spectrum of a typical miniature probe (solid line). For comparison the spectrum of the radiated pulse to be measured is shown as the dotted line

3.7.2   Refraction coefficients

As outlined above, in a fluid, ultrasonic transducers generate plane longitudinal and edge waves. In a solid medium both longitudinal and shear waves can exist and, depending on the angle of incidence, mode conversion from one to the other can occur at interfaces. Furthermore, as is well known, refraction and reflection occurs at interfaces. Since the angular dependence of the refraction of infinite plane waves at a fluid solid interface is well understood, as a first step in characterising the action of the miniature probe a series of experiments are described to measure just the plane waves radiated from a circular transducer.

Figure 3.8 shows a series of field-point measurements taken using the set up given in Figure 3.5. A test piece of thickness 15mm was used and the incident angle from the emitting transducer was varied so that the refracted waves in the steel lay between normal (0 degrees) to 77 degrees. The plane compression/longitudinal wave and edge compression/longitudinal wave are labelled PC and EC, respectively. By confining measurements to the central region of the beam, where the edge waves from the rim arrive after the plane wave and by careful choice of pulse shape, transducer geometry and the range at which measurements are taken, it is possible to arrange that the difference in arrival times of the PC and EC pulses is sufficient to allow the amplitude of the plane-wave pulse to be measured free of errors due to overlapping pulses. As shown in Figure 3.8, at all angles considered the first half-cycle of the PC pulse is not overlapped by the EC pulse, and the amplitude of this half-cycle is taken to represent the overall amplitude of PC. The time scale is restricted to show just the longitudinal wave components and to allow each plot to be shown to the same scale, the origin of on the Y axis each plot is arbitrary.
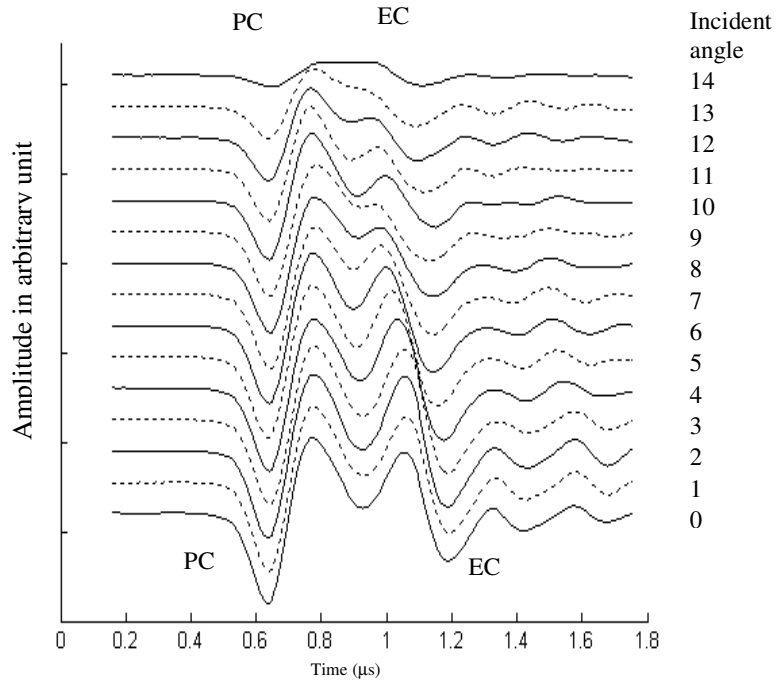
Figure 3.8 Measured plane compression waves (PC) and edge compression waves (EC) longitudinal waveforms with incident angles in water (θ) incrementing by 1 degree from bottom, 0 degrees to top, 14 degrees. The corresponding propagation angles in the steel vary from 0 to 77 degrees, respectively. The normal to the miniature probe is parallel to the vertical Z-axis. For clarity, each plot is to an arbitrary time origin.

Figure 3.9 shows a plot of the variation with propagation direction in steel of the amplitude (stars *) of the PC pulses given in Figure 3.8. For comparison the calculated refraction coefficients are shown as the dashed-dotted curve. The two curves are normalised so that they coincide at normal incidence. To test the hypothesis that the miniature probe responds to the normal component of the received waves, the calculated normal component of the refracted wave is shown as the solid curve. The good agreement between the measured amplitudes (*) and calculated normal components (solid line) supports the assumption that the probe responds to normal components.

Figures 3.10 and 3.11 show a similar set of results as those of Figures 8 and 9, but for the shear wave components. Here, the time scale is chosen to show the relevant (shear) component arising from mode conversion of the incident plane longitudinal wave. As before, the time origin of each plot is arbitrary. Once again, Figure 3.11 shows that taking the normal component of the refracted wave amplitudes gives generally good agreement between calculated (solid line) and measured (*) refraction coefficients. At the first critical angle for the shear wave, (the angle where the refracted longitudinal wave is directed parallel to the solid surface, here ~32 degrees) the agreement is not good. Such an effect has often been noted in work that compares calculated refraction coefficients obtained assuming infinite plane continuous waves, with experimental measurements of bounded, pulsed beams. This discrepancy is further discussed below where sets of results were presented to test further the hypothesis concerning the miniature probe's response to normal components.
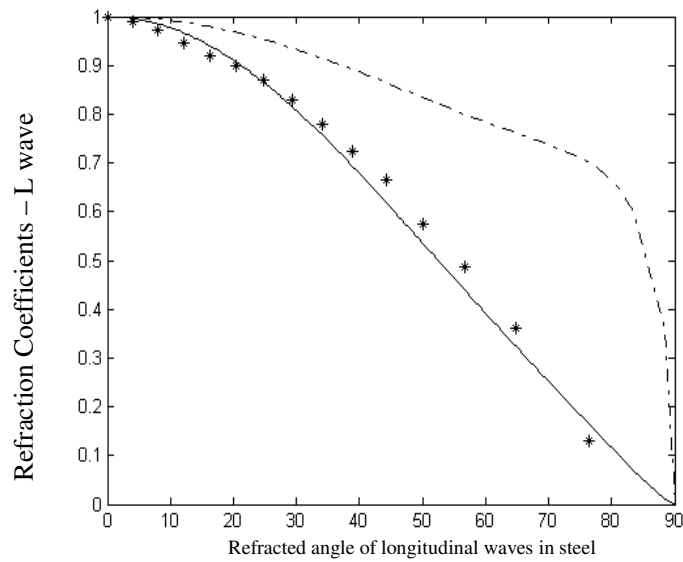
Figure 3.9 Measured (*) and calculated (solid line) refraction coefficient for the normal component of plane longitudinal waves (PL). The normal to the miniature probe is parallel to the vertical Z-axis. For comparison, the calculated refraction coefficient in the direction of propagation is shown as the dashed-dotted curve.
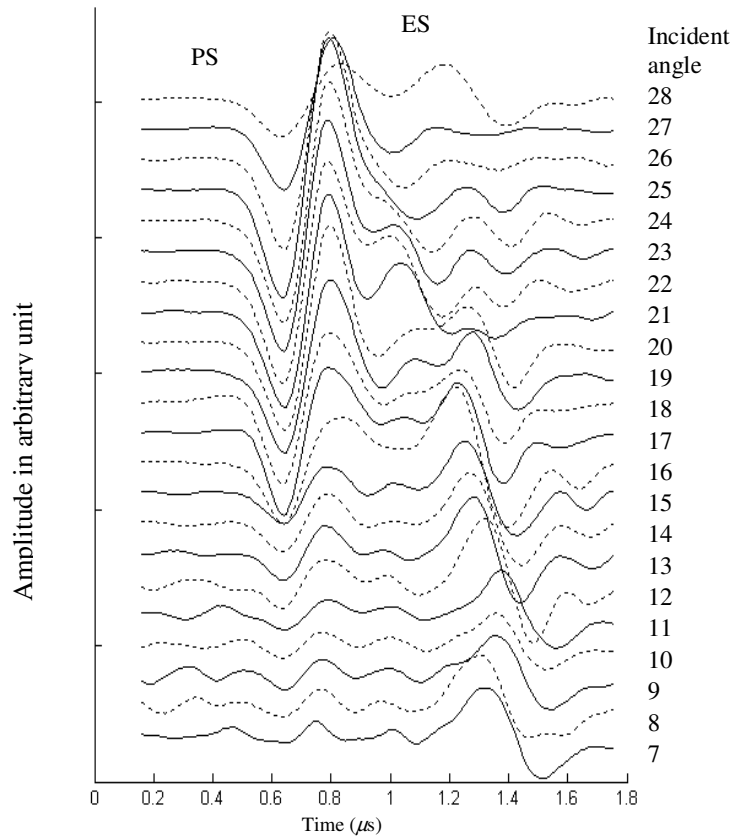
Figure 3.10 Measured plane shear waves (PS) and edge shear waves (ES) with incident angles in water incrementing by 1 degree, from bottom, 7 degrees to top 28 degrees. The corresponding propagation angles in the steel vary from 13 to 80 degrees, respectively. The normal to the miniature probe is parallel to the vertical Z-axis. For clarity, each plot is to an arbitrary time origin.
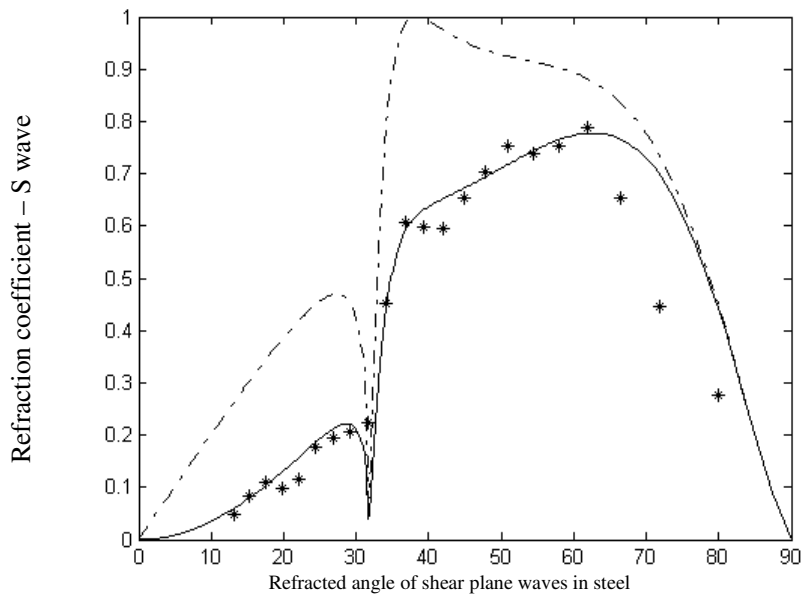
Figure 3.11 Measured (*) and calculated (solid line) refraction coefficient of the normal component of plane shear waves (PS). For comparison, the calculated refraction coefficient in the direction of propagation in the steel is shown as the dashed-dotted curve. The normal to the miniature probe is parallel to the vertical Z-axis

As demonstrated in Figure 3.12, a shear wave arriving at normal incidence to a surface has a zero component in the normal direction and the polarity of the normal component changes sign as the incident angle varies either side of the normal. Figure 3.13 shows a set of measured waveforms taken with the miniature probe coupled to the wedge-shaped test piece shown in Figure 3.7. The angle of the wedge has been chosen so that the amplitude of the incoming shear wave does not vary greatly as the angle of incidence to the probe goes through the normal direction. This aids in quantifying the probe's response, as the actual amplitude of the incoming waves is relatively constant over the range of angles considered. Figure 3.11 shows that the refraction coefficient and hence the incoming wave amplitude does not vary greatly when the propagation direction in the steel lies between 45 to 75 degrees. With the wedge angle used, the incoming shear wave arrives at normal incidence to the miniature probe when the propagation direction in the steel is 60 degrees and theoretically its output should be zero at this angle if it truly responds to normal components. Furthermore, there should be a change in polarity of the miniature probe output as the propagation direction in the steel varies either side of 60 degrees. From the measured waveforms given in Figure 3.13 we do observe a reversal of polarity, waveforms (a) through (c) being of opposite polarity compared to (e) through (f). Close to 60 degrees, although the probe output does not drop to zero, there is a minimum in its response. One explanation for a non-zero output near 60 degrees is that the incoming shear wave is not truly plane. The incoming edge-wave component is significant in this set of results, especially at propagation angles close to 60 degrees and tends to partially overlap the plane-wave component. Away from 60 degrees the plane-wave component dominates. Since the edge wave is not at normal incidence to the probe at around 60 degrees it will give a significant output from the probe.
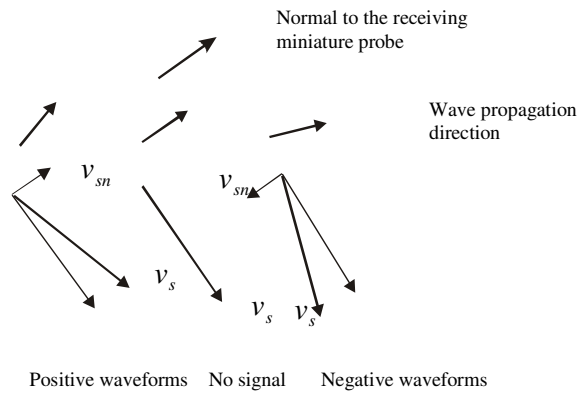
Figure 3.12 Decomposition of shear-wave particle velocity into normal and perpendicular components with respect to the receiving miniature probe. The direction of propagation of the centremost example is normal to the miniature probe.

The amplitudes of the measured waveforms given in Figure 3.13 are plotted against propagation direction in the steel in Figure 3.14. For comparison, the calculated amplitude of the incoming shear wave is shown as the dashed-dotted line and the normal component of the calculated amplitude is the solid line. Bearing in mind the discussion above, these plots reinforce the assumption that the probe responds to normal components.

When comparing the plots of Figure 3.14 with those of Figure 3.11, it should be noted that in Figure 3.14 the probe is angled at 60 degrees to the vertical Z-axis, so that plane shear waves can arrive around normal incidence, whereas in Figure 3.11 the probe is aligned to the Z-axis.
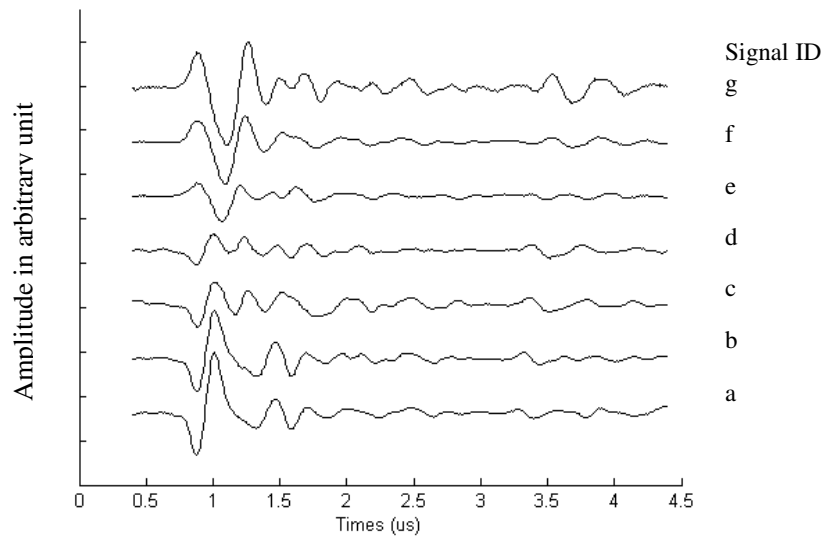
Figure 3.13 Measured plane shear waveforms in steel using the wedge-shaped test piece with the normal to the miniature probe at 60 degrees to the vertical Z-axis. The propagation direction for waveforms (a) to (g) is shown in Figure 3.14. For clarity, each plot is to an arbitrary time origin.
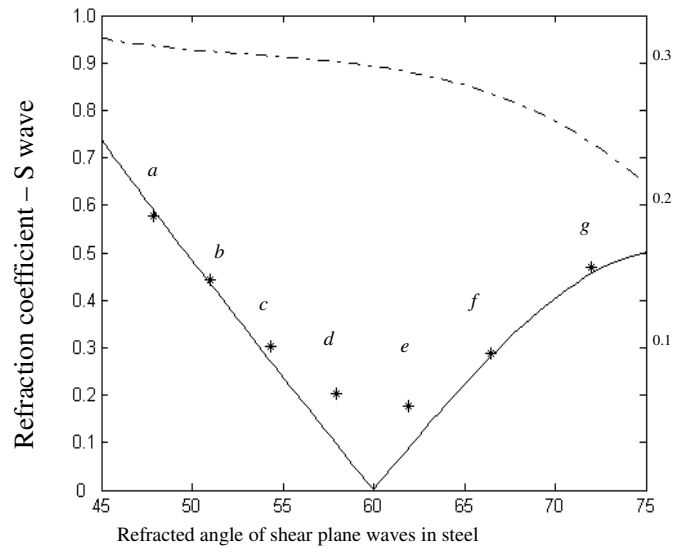
Figure 3.14 Measured (*) and calculated (solid line) refraction coefficient of the normal component of shear plane waves plotted to the right hand vertical axis. For comparison, the calculated refraction coefficient in the direction of propagation in the steel is plotted to the left hand vertical axis as the dashed-dotted curve. Note that in contrast to Figures 3.9 and 3.11, the normal to the miniature probe is at 60 degrees to vertical Z-axis.

3.7.3   Field point waveforms

To demonstrate briefly the usefulness of the miniature probe to measure the complicated nature of the ultrasonic beam from a transducer coupled to a solid, Figures 3.15 to 3.18 include typical measured field-point waveforms for a number of coupling situations, all using test pieces similar to that shown in Figure 3.6. For completeness, the measurements are compared to calculated waveforms [20].

Figure 3.15 shows how the waveforms at points on axis vary with range in steel. These results are obtained with the emitting longitudinal wave transducer directly coupled at normal incidence to steel test pieces of various thickness, no water or plastic "standoff" being employed. As before, for clarity, the waveforms are plotted with arbitrary time origins chosen to align the plane wave pulses. As outlined above, a longitudinal-wave transducer directly coupled to a solid does not radiate any shear plane waves in the solid but a shear edge wave is detected. In earlier work [7, 8] the existence of such a shear wave was attributed to the partial mode-conversion of the (toroidal) edge longitudinal wave. In Figure 3.15, the plane longitudinal and edge wave components are labelled PC and EC respectively and ES denotes the mode-converted shear edge wave. At the shortest range of 5 mm, most of the edge longitudinal wave converts into an edge shear wave. With increasing thickness, the refraction angles are such that less mode conversion occurs and as a result of the different velocities of propagation, the separation between the arrival times of the EC and ES pulses increases. The separation between the PC and EC pulses decreases with range as the path difference between the direct plane longitudinal wave and the edge longitudinal wave decreases with range. In general there is good agreement between the measurements and the calculated results [20]. However, the measured results show a number of small "ripples" throughout the waveforms that are not seen in the calculated results. These are due to a number of experimental factors. The emitting transducer is not an idealsource as assumed in the model used to make the calculations [20]. The transducer element is heavily damped in order to generate a short, wideband pulse. This backing is not perfectly homogeneous and produces some scattering that is radiated after the main pulse.

Furthermore, the miniature probe does not act as a perfect point receiver as assumed in the theoretical model [20]. Some of the incoming waves, especially the angled edge waves, reverberate within the probe itself to give small ripples that follow the main pulses received. Although in some results the pulses identified as edge wave contributions are of similar amplitude to these unwanted ripples, experimentally it is easy to discriminate the edge wave pulses, since there is a focussing effect for edge waves that does not exist for the randomly aligned waves giving rise to the ripples. This means that a small translation of the emitting transducer changes the amplitude of the received edge-wave pulses much more dramatically than that of the ripples, allowing the former to be identified.

Secondly, Figure 3.16 shows a similar set of results to that of Figure 3.15 but with the emitting transducer water coupled to the test pieces. A water path ("standoff") of 6mm was used. With such a small radius of curvature at the steel surface, significant mode conversion of the edge longitudinal wave can occur and the amplitudes of the resulting shear edge waves are similar to those of the corresponding waveforms of Figure 3.15, where direct coupling was used. Such results provide further evidence to support the concept that edge shear waves arise from the partial mode-conversion of the incident edge longitudinal wave [7,8,19], since in the fluid path no shear wave can propagate.
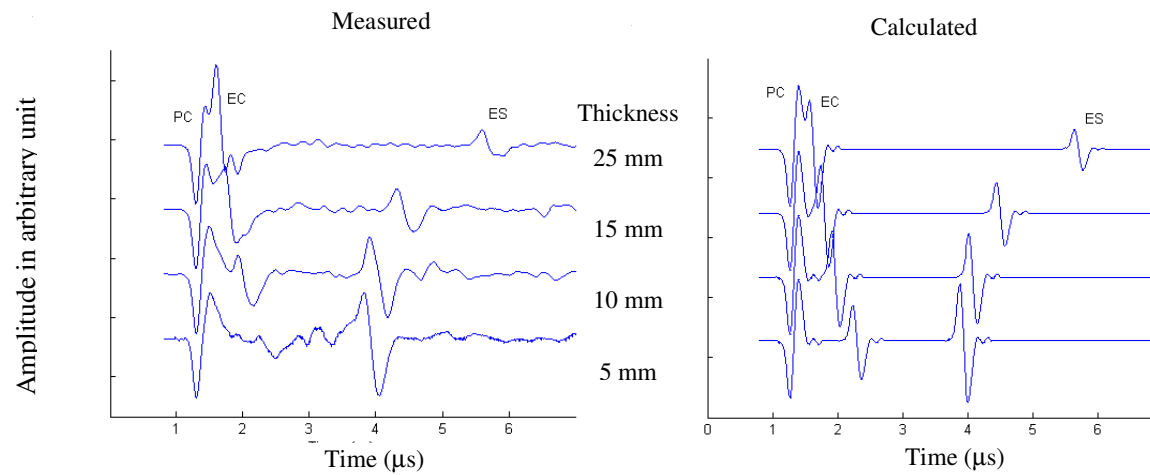
Figure 3.15 Axial waveforms from a directly coupled emitting transducer for various thickness of steel. For clarity, each plot is to an arbitrary time origin.
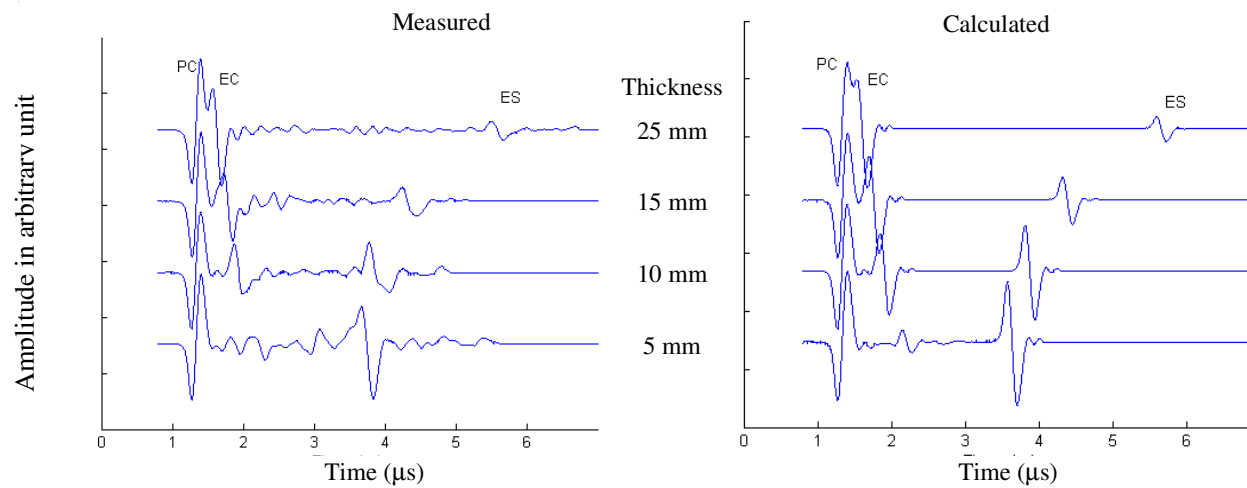
Figure 3.16 Axial waveforms for various thickness of steel using a normally aligned water-coupled emitting transducer (water path 6mm). For clarity, each plot is to an arbitrary time origin.
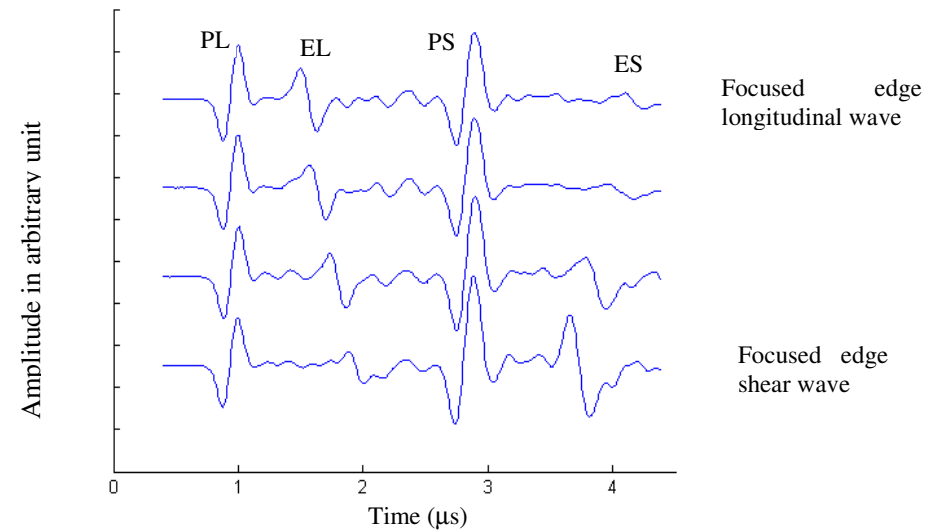
Figure 3.17 Measured waveforms with the emitting transducer at differing positions in the horizontal *X* direction. The incident angle in the water (θ_w) is 12 degrees and the water path along the transducer axis is 6 mm. For clarity, each plot is to an arbitrary time origin.
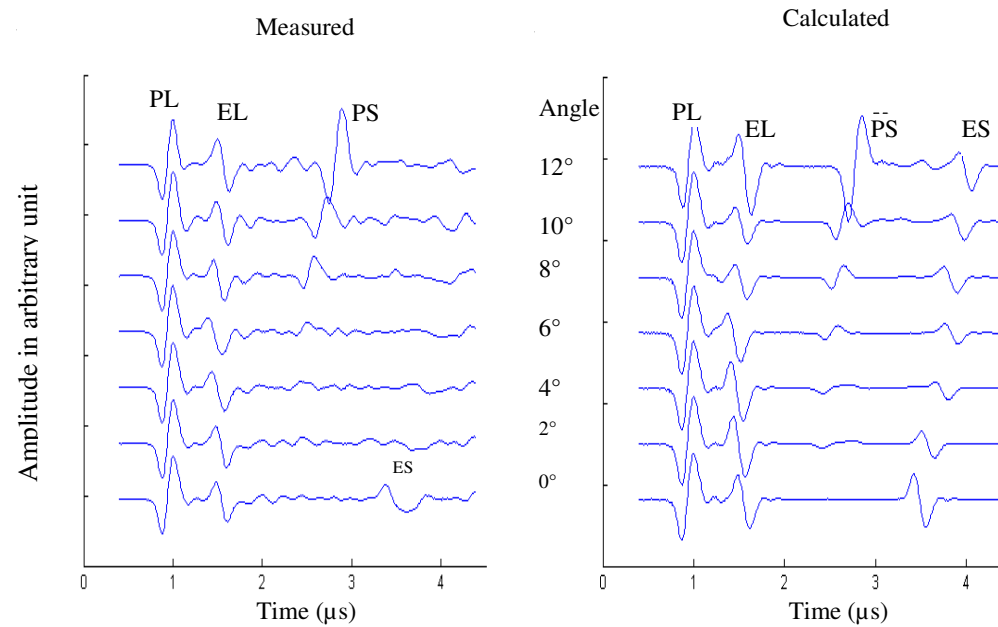
Figure 3.18 Waveforms with respect to the incident angle in the water (θ_w) for a steel test piece of thickness 10 mm. For clarity, each plot is to an arbitrary time origin.

Thirdly, Figure 3.17 shows results to demonstrate how the received field-point waveforms vary as an angled water-coupled transducer is translated in the horizontal X-axis. Such results are helpful in demonstrating further the experimental details earlier used when quantifying the response of the miniature probe (Figures 8-11 and 13-14). As discussed previously, with an angled emitter being water-coupled to a solid, the longitudinal and shear wave beams in the solid propagate in different directions and the emitting transducer must be translated to "centralise" the miniature probe to either beam. Although the beams no longer have circular symmetry, as shown in Figure 3.17, the emitting transducer can be translated to give maximum amplitude for either the edge longitudinal wave or the shear edge wave. By so doing it is possible to ensure that the miniature probe lies well within the plane wave beams and that details of each pulse can be observed measured free of errors due to overlapping edge-wave components. Note however that as demonstrated in Figures 8 and 10 the good separation of the plane and edge wave pulses demonstrated in Figure 3.17 cannot be maintained at all of the angles used in plotting the refraction coefficients in Figures 9 and 11. The technique used for measuring the amplitude of just the first half-cycle of the plane waveforms remains the best method to estimate the relative amplitude at each angle.

Finally Figure 3.18 shows how the ultrasonic field in steel varies with the angle of incidence from a water coupled emitting transducer. At each angle, the emitter has been translated to give a maximum edge longitudinal-wave pulse. As the coupling angle increases away from normal (0 degrees), partial mode conversion of the plane longitudinal wave into a plane shear wave can be observed. The complicated nature of the refracted beam is evident, there being four wave types contributing to the field point waveforms. Eventually, beyond the range of angles used here, the plane longitudinal wave can no longer propagate (at the first critical angle), however an edge longitudinal wave can still exist, in addition to the shear plane and edge waves. So even when using "shear wave" probes designed to exclude plane longitudinal waves by operating beyond the first critical angle, edge longitudinal waves will still be radiated. The existence of these various wave types can dramatically affect the form of echo pulses received back at the emitting

transducer when using pulse echo techniques to detect and characterise small, point-like defects in solids.

3.8   Conclusions

Specially constructed miniature transducers (probes) capable of measuring both longitudinal and shear waves at the surface of a solid have been discussed. The size and bandwidth of the probes allows field-point measurements to be made over a frequency range of around 0.5 to 7 MHz. Measurements of the amplitude of refracted locally plane longitudinal and shear waves made using such a probe directly coupled to the surface of a solid have been compared with predicted amplitudes given by well-known expressions for the reflection coefficients of infinite plane waves. Such comparisons have shown that, to a reasonable approximation, the miniature probe responds to the normal component of the particle velocity of both the incoming longitudinal- and shear-wave pulses. Furthermore, the measured particle velocity at the surface is proportional to that within the solid.

Field-point measurements made of the pulsed longitudinal and shear waves radiated into steel from an angled water-coupled emitting transducer, typical of those used in NDE applications, show a complicated field structure. Over certain angles, the field can include four wave types, longitudinal and shear locally plane waves together with longitudinal and shear spreading edge waves. The measured results compare well with calculations made using a recently developed theoretical model [20]. The existence of these various wave types dramatically affects the form of echo pulses encountered in pulse-echo techniques to detect and characterise small defects in solids. Knowledge of the true nature of the radiated beam greatly aids in the design of testing procedures and the interpretation of pulse-echo results.

3.9   References

1   Weight, J.P., and Hayman, A.J., "Observations of the propagation of very short ultrasonic pulses and their reflection by small targets", *J. Acoust. Soc. Am. 63*, 396-404 (1978)

2   Jian, X., Dixon, S. and Palmer S.B., "In-plane and out-of-plane particle velocity measurement using electromagnetic acoustical transducers," *IEEE Ultrasonic Symposium* 2005.

3   Stepanishen P. R. and Fisher G., "Experimental verification of the impulse response method to evaluate transient acoustic fields," *J. Acoust. Soc. Am.* 69, 1610-1617, 1981

4   Weight J. P., "Ultrasonic beam structure in fluid media," *J. Acoust. Soc. Am.* 76, 1184-1191, 1984

5   Monchalin J. P., "Heterodyne interferometric laser probe to measure continuous ultrasonic displacements," *Review of Scientific Instruments* 56, 543-546, 1985

6   Royer, D., Dubois, N. and Fink, M., "Optical probing of pulsed, focused ultrasonic fields using a heterodyne interferometer," *Applied Physics Letter* 61, 153-155, 1992

7   Pitts, T. A., Sagers, A., Greenleaf, J. F., "Optical phase contrast measurement of ultrasonic fields," *IEEE Trans. Ultrason. Ferroelectr. Freq. Control* 48, 1686-1694, 2001

8   Weight J. P., "A model for the propagation of short pulses of ultrasound in a solid," *J. Acoust. Soc. Am.* 81, 815-826, 1987

9   Ilan A. and Weight J. P., "The propagation of short pulses of ultrasound from a circular source coupled to an isotropic solid," *J. Acoust. Soc. Am.* 88(2), 1142-1151 (1990)

10   Bakker M.C.M., Verweij M.D., "An approximation to the far field and directivity of elastic wave transducers," *Journal of the Acoustical Society of America* 111, 1177-1188,2002

11   Bakker, M. C. M. and Verweij, M. D., "Experiment validation of two elastodynamic models for the wave field generated by ultrasonic transducer," *J. Acoust. Soc. Am.* 113, 1850-1862, 2003

12   Jian X, Dixon S, Edwards RS, "Modeling ultrasonic generation for Lorentz force EMATs," *Insight* 46 (11), pp671-673, Nov., 2004.

13   Jian X, Dixon S, Edwards RS, "Optimising Ultrasonic Wideband Rayleigh Wave Generation by Pulsed Electromagnetic Coils," *NDT&E* 2005 pp42-52.

14   Jian X, Dixon S, Edwards RS, J Reed, "Coupling Mechanism of a Pulsed EMAT," to be published.

15   Jian, X., Guo, N., Li, M.X., and Zhang, H.L., "Characterization of bonding quality in a multilayer structure using segment adaptive filtering," *J. Nondestructive Eval.*, vol.21, pp55-65, 2002.

16   Gendreu P., Fink M. and Royer D., "Optical imaging of transient acoustic fields generated by piezocomposite transducers," *IEEE Trans. Ultrason. Ferroelectr. Freq. Control* 42, 135-143, 1995

17   Barriere, C. and Royer D., "Optical measurement of large transient mechanical displacements," *Applied Physics Letter* 79, 878-880, 2001

18   Jian X., Weight J. P. and Grattan K. T. V., "The characterisation of miniature wide band ultrasonic transducers to measure compression and shear waves in solid media", *Proceeding of the 5th World Congress on Ultrasonic, Paris*, 2003.

19   Mayer W. G., "Energy partition of ultrasonic waves at flat boundaries," *Ultrasonics* 3, 62-68, 1965

20   Jian, X., Weight, J. P., Grattan, K. T. V., "A model for the propagation of short pulses of ultrasound in a solid immersed in water", *Proceeding of the 5th World Congress on Ultrasonics, Paris,* 2003

4. ULTRASONIC FIELD MEASUREMENT USING AN ELECTROMAGNETIC ACOUSTIC TRANSDUCER (EMAT)

4.1 Summary

EMATs are particle velocity sensors, which can be designed to have sensitivity to in-plane and, or out-of-plane ultrasonic displacements, by suitably arranging the magnetic field in the receiving EMATs relative to the orientation of the coil. Good agreement between the results from modelling and experimental measurements has been demonstrated.

4.2 Introduction

Ultrasonic field measurement is of great interest in transducer development, material evaluation and non-destructive evaluation (NDE) [1-10]. The in-plane and out-of-plane components of the particle velocity of bulk waves (longitudinal and shear) when they arrive at the surface of the sample are always in phase. The ratio of the amplitude of in-plane particle velocity to that of the out-of-plane particle velocity is dependent only on the incident angle of the incoming ultrasonic wave to the sample surface [6].

However, the in-plane and out-of-plane particle velocities of guided waves, such as Rayleigh or Lamb waves are not in phase [9, 11]. The ratio of the amplitude of the in-plane particle velocity to that of the out-of-plane particle velocity is dependent on the material's elastic properties. It has been reported that the responses from defects of in-plane and out of-plane ultrasonic wave displacements are different [9]. Thus, it

is reasonable to speculate that a particular particle velocity component may have optimal sensitivity for a specific defect inspection and sizing [9] application.

Miniature conventional piezoelectric transducers have been reported for the measurement of the surface normal component of ultrasonic fields in solids and fluids, where the size of the piezoelectric element is required to be smaller than the half-wavelength of the ultrasonic waves [6]. Consistent acoustic coupling throughout the entire measurement process is required, but this is often difficult to maintain, resulting in inaccurate results.

Laser interferometers, such as Michelson interferometers, can be used to measure the absolute out-of-plane displacement of ultrasonic fields in solids with smooth, highly reflective surfaces, as well as in liquids by means of an optically transparent plate [7, 10]. Since it is non-contact, there are no coupling problems and there is no perturbation of the ultrasonic field by the measurement probe. The cost of such types of interferometer is high and there is a potential laser hazard associated with their use.

EMATs generate and detect ultrasonic waves via electromagnetic coupling between the EMAT and the metal samples. They operate via the Lorentz force or magnetoelastic mechanism, or both simultaneously [12-17]. EMATs are non-contact devices, and therefore, ultrasonic waves can be measured with minimal disturbance to the ultrasonic wave or material. However, the stand-off between an EMAT and a metal sample does have an influence on the generation or detection characteristics. EMATs are inexpensive, inherently safe and highly portable, but are relatively insensitive when compared to piezoelectric based devices.

It has been reported that the EMAT generation efficiency can be enhanced by arranging the magnetic field optimally [2,] or by means of a ferrite back-plate [1]. The ultrasonic field generated by a circular coil EMAT can be modelled, to analyze the influence of the various parameters of EMAT design upon the ultrasonic generation mechanism [12-13].

Modelling the detection of ultrasound via an EMAT is important for understanding the mechanism of wave detection, and informing the design of optimal EMAT receivers [3]. This chapter is organized as following; the Theory section deals with the modelling of EMATs as receivers, treating the EMAT as velocity sensors with the capability of the detection of the in-plane and out-of-plane particle velocities of ultrasonic waves, whilst the section of Experimental Measurements presents experimental verifications and the last section provides conclusions and discussions on the work reported.

4.3   Theory

A model for the calculation of the ultrasonic signal induced in an EMAT detection coil is presented, which is useful for both general EMAT design, and for a tailoring EMATs to a specific NDT application.

4.3.1   Large EMATs

Figure 4.1 shows the typical structure of an EMAT receiver, which is composed of the receiving coil and the magnet that supplies the static magnetic field in the test specimen for ultrasonic wave detection.

Generally, the thickness of the test specimen and the magnet in the EMAT is much larger than the electromagnetic skin depth at the corresponding frequency of the detected ultrasonic waves. Thus, the experimental geometry shown in figure 4.1 can, in fact, be simplified to that shown in figure 4.2. In figure 4.2, zone 0 is the air gap between the magnet and the test specimen, and is the region where the EMAT's receiving coil is located. Zone 1 corresponds to the magnet, which is usually an electrical conductor (NdFeB), and zone 2 and 3 are the electrically conductive test specimen.

Magnet

O O O   coil
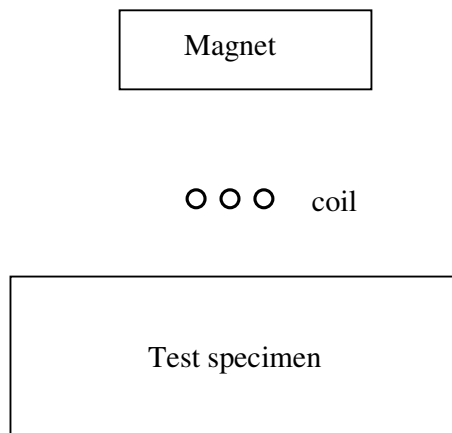
Test specimen

**Figure 4.1 Typical structure of an EMAT receiver composed of a coil and a magnet,
which is positioned over the test specimen at a lift-off distance.**

Zone 1

$z = z_1$

Zone 0

○ ○ ○ ←── coil

Z

X

$z = 0$

Zone 2

Current sheet J_d

$z = z_0$
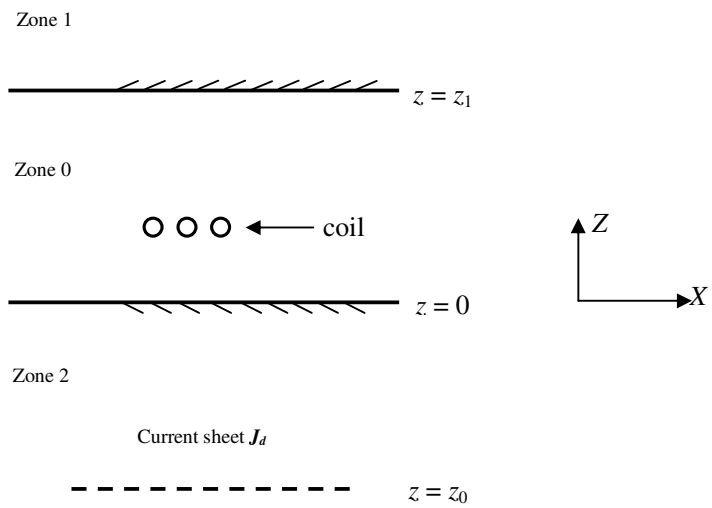
Figure 4.2 Current sheets in an electrically conductive test specimen, generate magnetic vector potentials in the air above the conductor.

Ultrasonic waves induce particle vibration in the test specimen as they propagate through the specimen. Eddy currents induced in the test specimen in the presence of a static magnetic field, produce time varying magnetic fluxes though the receiving coil, and generate a voltage across the coil. The induced eddy current sheet at a depth z_0 in the test specimen, which is due to the particle vibration, is given by

$$J_{ed}(z_0) = \sigma_2 v(z_0) \times B_0(z_0) \tag{4.1}$$

where, $v(z_0)$ and $B_0(z_0)$ are the vectors of the particle velocity and magnetic field at depth z_0 in the test specimen respectively. Here and elsewhere in this chapter, variables in bold denote a vector.

From Maxwell's equations, the magnetic vector potential differential equations in zones 1, 0, 2 and 3 are A_1, A_0, A_2 and A_3, and are given respectively by [1, 3],

$$\nabla^2 A_1 = j\omega\mu_1\sigma_1 A_1 \tag{4.2}$$

$$\nabla^2 A_0 = -\omega^2\mu_0\varepsilon_0 A_0 \tag{4.3}$$

$$\nabla^2 A_2 = j\omega\mu_2\sigma_2 A_2 \tag{4.4}$$

$$\nabla^2 A_3 = j\omega\mu_3\sigma_3 A_3 \tag{4.5}$$

where μ_i and σ_i are magnetic permeability and electrical conductivity in corresponding zone i, ω is the frequency of the changing magnetic field, and j is $\sqrt{-1}$.

Taking the boundary conditions into account, the solutions are obtained. The magnetic vector potential in zone 0 at a distance z from the test block, due to a sheet current at a depth z_0, is given by,

$$A_0 = \mu_2 e^{\frac{1+j}{\delta_2}z_0}\frac{\delta_2}{1+j}\boldsymbol{J}_{ed}(z_0)(e^{jk_0z}+e^{-jk_0z}e^{j2k_0z_1}) \tag{4.6}$$

where δ_2 and k_0 are the skin depth and the wave number of the electromagnetic wave of frequency ω in the test specimen respectively. From figures 1 and 2, z_1 represents the liftoff whilst z_0 denotes the depth of the induced eddy current sheet.

Integrating over the thickness of the test specimen, the total magnetic vector potential in zone 0, due to the eddy current sheet in the entire test specimen is obtained by,

$$\boldsymbol{A}_{0t} = \int_{-\infty}^{0} \boldsymbol{A}_0 dz_0 \tag{4.7}$$

The total voltage induced in a linear coil of N turns and length l_0 in the receiving EMAT is given by

$$V = N\boldsymbol{l}_0 \cdot \boldsymbol{E}_0 = -N\boldsymbol{l}_0 \cdot \frac{\partial \boldsymbol{A}_{0t}}{\partial t} \tag{4.8}$$

Assuming a plane ultrasonic wave, $\boldsymbol{v}(z_0) = \boldsymbol{v}_0(e^{-jk_0z}+e^{jk_0z})$, and uniform magnetic field, $\boldsymbol{B}_0(z_0) = \boldsymbol{B}_0$.

After some manipulations, the total magnetic vector potential is given by,

$$\boldsymbol{A}_{0t} = 4\frac{1}{j\omega(1-jk_0^2\delta_2^2/2)}\boldsymbol{v}_0 \times \boldsymbol{B}_0 \tag{4.9}$$

The total voltage induced in the coil is given by,

$$V = -4N\frac{1}{1-jk_0^2\delta_2^2/2}\boldsymbol{l}_0 \cdot (\boldsymbol{v}_0 \times \boldsymbol{B}_0) \tag{4.10}$$

The voltage signal detected by the EMAT receiver is proportional to the cross product of the vector of particle velocity, v_0, and the vector of the magnetic field, B_0, and is not dependent on the lift-off between the coil and the test specimen. This is a particle velocity sensor. It is noted that the signal produced by a practical EMAT in detecting an ultrasonic wave is dependent of the lift-off between the receiving EMAT and the test specimen.

In the case that the eddy current induced in the magnet is ignored, the detected voltage signal is given by [3]

$$V = -2N \frac{1}{1 - jk_0^2 \delta_2^2 / 2} l_0 \cdot (v_0 \times B_0) \qquad (4.11)$$

4.3.2   EMATs of Finite Size

Only particle vibrations within the skin depth of the electromagnetic wave can produce an effective contribution to the induced voltage signal [3, 12-13]. Assuming an equivalent current, J_{eq}, in air that generates an identical magnetic field in the coil of the receiving EMAT to that generated by the current sheet, J_{ed}, at depth, z_0, which is given by,

$$J_{eq} \propto \mu_2 e^{\frac{1+j}{\delta_2} z_0} \frac{\delta_2}{1+j} J_{ed} \qquad (4.12)$$

Considering a magnet of a size of w_0 wide and l_0 long with its centre at the origin of the coordinate system, the static magnetic field, B_0, is mainly limited to this area. The magnetic field, B, at point (x, y, z), produced by the current sheet element due to the particle vibration within the area between, $-w_0/2$ to $+w_0/2$, in the x-axis and, $-l_0/2$ to $+l_0/2$ in the y-axis, where, B_0, has significant amplitude, is given by

$$B = \mu_2 e^{\frac{1+j}{\delta_2} z_0} \frac{\delta_2}{1+j} \int_{-\frac{l_0}{2}}^{\frac{l_0}{2}} dy_0 \int_{-\frac{w_0}{2}}^{\frac{w_0}{2}} \frac{\mu_0}{4\pi} \frac{J_{ed} \times r}{r^2} dx_0 \qquad (4.13)$$

where r is the distance between the eddy current element (x_0, y_0, z_0) and the field point (x, y, z), and is given by,

$$r = \sqrt{(x-x_0)^2 + (y-y_0)^2 + (z-z_0)^2}$$

Considering that the particle velocity, v_0, is in the x-axis direction, and the magnetic field, B_0, is in the z-axis direction, then the eddy current sheet, J_{ed}, is in the y-axis direction. Assuming that the coil is arranged in the middle of the magnet, in the x-axis direction, the magnetic field, B, that is induced by, J_{ed}, the eddy current sheet in the test specimen, is in the x-axis direction due to symmetry, and is given by,

$$B_x = e^{\frac{1+j}{\delta_2}z_0} \frac{\delta_2}{1+j} \frac{\mu_2\mu_0}{4\pi} \int_{-\frac{w_0}{2}}^{\frac{w_0}{2}} dx_0 \int_{-\frac{l_0}{2}}^{\frac{l_0}{2}} \frac{J_{ed}B_0(z-z_0)}{r^3} dy_0 \tag{4.14}$$

By taking the integral of the whole thickness of the test specimen, the total magnetic field is obtained, and is given by,

$$B_{xt} = \frac{\delta_2}{1+j} \frac{\mu_2\mu_0}{4\pi} \int_{-\infty}^{0} e^{\frac{1+j}{\delta_2}z_0} J_{ed}(z-z_0) dz_0 \int_{-\frac{w_0}{2}}^{\frac{w_0}{2}} dx_0 \int_{-\frac{l_0}{2}}^{\frac{l_0}{2}} \frac{B_0}{r^3} dy_0 \tag{4.15}$$

The voltage of the detected ultrasonic signal is given by

$$V = -N \int_{-\frac{l_0}{2}}^{\frac{l_0}{2}} \frac{\partial B_{xt}}{\partial t} dy \tag{4.16}$$

Considering a special case, $x \gg l_0$ and $x \gg w_0$,

$$V = -Nl_0 \frac{\partial B_{xt}}{\partial t}\bigg|_{(0,0,z)} \tag{4.17}$$

After some manipulations, the voltage of the detected ultrasonic signal is given by,

$$V = j \frac{\mu_0}{4\pi} N l_0{}^2 w_0 B_0{}^2 \frac{v}{z^2} \tag{4.18}$$

4.3.3 In-plane and Out-of-plane Ultrasonic Waves

As stated earlier, guided waves such as Rayleigh waves have in-plane and out-of-plane particle velocities that are not in phase.

The in-plane and out-of-plane particle velocity components of Rayleigh waves can be given by [11]

$$v_x(z) = A_R k_R (e^{-q_R z} - \frac{2 q_R s_R}{k_R{}^2 + s_R{}^2} e^{-s_R z}) e^{j(k_R x - \pi/2)} \tag{4.19}$$

$$v_z(z) = A_R q_R (e^{-q_R z} - \frac{2 k_R{}^2}{k_R{}^2 + s_R{}^2} e^{-s_R z}) e^{j k_R x} \tag{4.20}$$

where k_R is the wave number of Rayleigh wave, q_R and s_R are given by

$$q_R = \sqrt{k_R{}^2 - k_l{}^2} \tag{4.21}$$

$$s_R = \sqrt{k_R{}^2 - k_t{}^2} \tag{4.22}$$

The out-of-plane particle velocity of Rayleigh waves within the skin depth, has a phase of $\pi/2$ ahead of the in-plane particle velocity. The amplitude of the out-of-plane particle velocity is not the same as that of the in-plane particle velocity, and is dependent on the material of the test specimen. For a test specimen of aluminium, the former has a larger amplitude than the latter.

4.4   Experimental Measurements

Measurements were carried out on an aluminum test block. Its longitudinal wave and shear wave velocities in the test piece are 6310 and 3100 m/s respectively, and the Rayleigh wave velocity is 2920 m/s.

Figure 4.3 is a schematic view of the EMATs for in-plane and out-of-plane ultrasonic wave velocity.,

A circular magnet was used to provide external permanent magnetic field for ultrasonic field detection. Measured magnetic field is shown in Figures 4.4 and 4.5. It can be seen that the static magnetic varied with lift-off and radial distance.

Rayleigh waves in the aluminum test block are measured, and are shown in figure 4.6. The lines "In" and "Out" denote in-plane and out-of-plane ultrasonic wave displacement. The line "Out" is about 1.7 times larger in amplitude than that of the line "In", and it has phase of $\pi/2$ ahead of the latter. Figure 4.8 shows calculated Rayleigh wave, using finite element methods [7, 9].

$$B$$

$$v_{out}$$

(a)

$$B$$

$$v_{in}$$
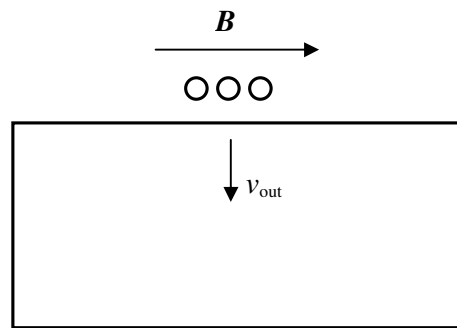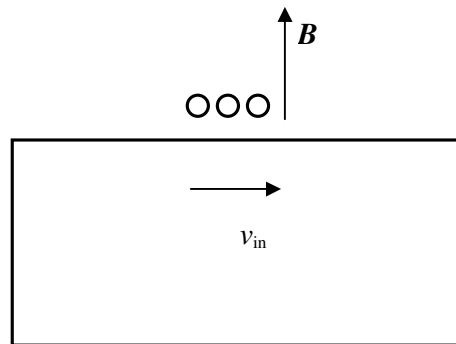
(b)

Figure 4.3 Schematic structure of EMAT receivers for out-of-plane (a) and in-plane (b) particle velocity detection, where the applied static magnetic fields in the specimen supplied by the magnet in the EMATs are in-plane and out-of-plane respectively.
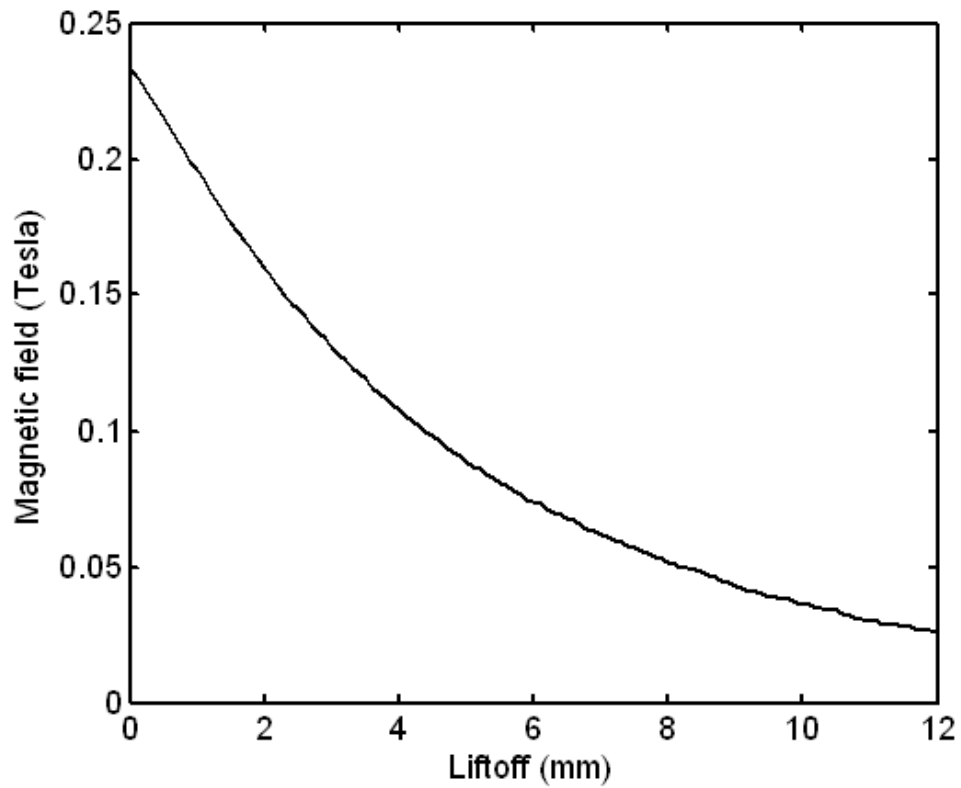
Figure 4.4 Measured normal magnetic fields on the axis of the circular magnet with respect to the distance from the magnet.
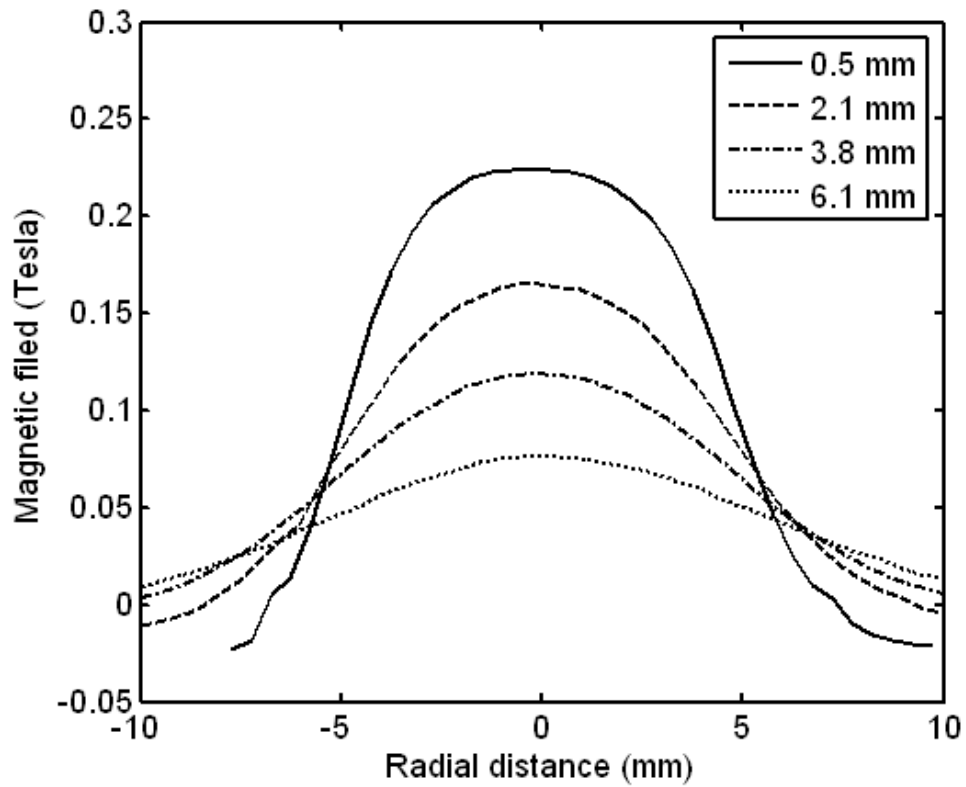
Figure 4.5 Measured normal magnetic fields with respect to radial distance at various distances to the cylindrical magnet flat surface.
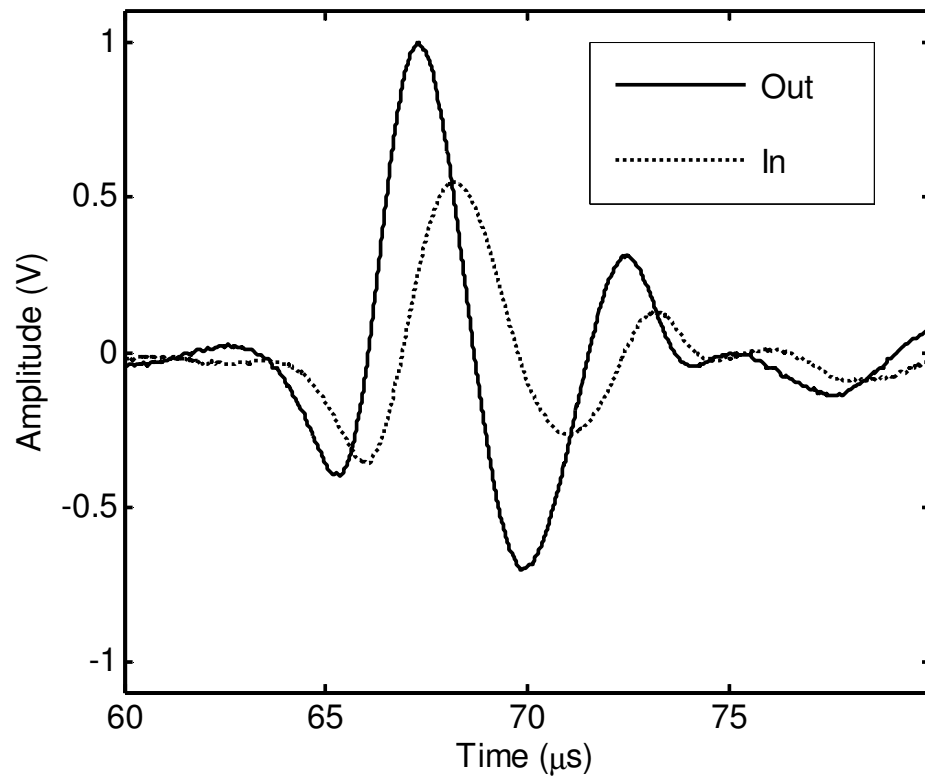
Figure 4.6 Measured in-plane and out-of-plane particle velocity of Rayleigh waves. The out-of-plane particle velocity is of $\pi/2$ phase ahead of the in-plane particle velocity.

4.5   Discussion and Conclusions

A model has been developed, allowing the calculation the ultrasonic signal detected using EMATs. Receiving EMATs are particle velocity sensors, detecting mainly the ultrasonic waves within the skin depth of the electromagnetic wave in the test specimen at the frequency interested. The influence of liftoff on the detection of the ultrasonic plane wave is dependent on the size of the coil. A large receiving EMAT is generally less subject to the liftoff variations in response.

By arranging the static magnetic field of the magnet in the EMATs perpendicular to the surface of the test specimen, the EMATs are predominantly sensitive to in-plane particle velocity of the incident ultrasonic waves. By arranging the static magnetic field parallel to the surface of the test specimen, the EMATs are predominantly sensitive to out-of-plane particle velocity of the incident ultrasonic waves.

The in-plane particle velocities of bulk waves (longitudinal waves and shear waves) are always in-phase with that of the out-of-plane particle velocities. However, the phases of in-plane and out-of-plane particle velocities of guided waves such as Rayleigh waves, are different. The Defect response of in-plane particle is different from out-of-plane particle velocity. One may carry more information about the defect than the other, for a specific measurement. The capability of selective detection of the in-plane or out-of-plane particle velocity is sometimes very useful for defect evaluation, using guided waves such as Rayleigh waves or Lamb waves [9, 11]. However, for general applications, receiving EMATs are designed to pick up both in-plane and out-of-plane particle velocities to enhance the detection sensitivity of the receiving EMATs.

4.6   References

1   Jian X, Dixon S, Enhancement of EMAT and Eddy Current using a Ferrite Back-Plate, Sensors & Actuators: A Physical, 136(2007), pp132-136.

2   Jian X, Dixon S, Grattan KTV, Edwards RS, A Model for Pulsed Rayleigh Wave & Optimal EMAT Design, Sensors & Actuators: A. Physical 128 (2006): 296-304.

3   Kawashima K, "Quantitative calculation and measurement of longitudinal a transverse ultrasonic wave pulses in solid," IEEE Trans. Son. & Ultrason. SU31 (2), pp 83-94, 1984.

4   Dodd CV, Deeds WE, "Analytical solutions to eddy-current probe-coil problems," *J. Appl. Phys.* 39 (1968), pp2829-2838.

5   Bakker, M. C. M. and Verweij, M. D., "Experiment validation of two elastodynamic models for the wave field generated by ultrasonic transducer," J. Acoust. Soc. Am. 113, 1850-1862, 2003.

6   Jian X, Weight JP, Grattan KTV, Miniature wideband ultrasonic transducers to measure compression and shear waves in solid, Sensors & Actuators: A. 127 (2006): 13-23.

7   Jian X, Fan Y, Edwards RS and Dixon S, Surface-breaking crack gauging with the use of laser-generated Rayleigh waves, J. Appl Phys. 100 (2006): 064907.

8   Jian X., Dixon S, Baillie I, Edwards RS, Morrison J, Integrity evaluation of steel products using EMATs, J Physics D Applied Physics 40 (2007) pp 300-304.

9   Jian X, Dixon S, Guo N, Edwards RS, Pulsed Rayleigh Wave Interaction with Surface Cracks, J. Appl. Phys 101 (6): 064906, 2007.

10   Cooper J.A., Dewhurst, R.J., Palmer S.B., "Characterization of surface-breaking defect in metals with the use of laser-generated ultrasound," Phil. Trans. Royal Soc. London. A, Math. Phys. Sci. 320, pp319-326, 1986.

11   Viktorov IA, Rayleigh waves and Lamb waves-Physical theory and application, Plenum, New York, 1964.

12   Jian X, Dixon S, Edwards RS, K Quirk, Baillie I, Effect on Ultrasonic Generation of a Back-plate in Electromagnetic Acoustic Transducer, J. Appl. Phys. 102, 024909, 2007.

13   Jian X, S Dixon, Edwards RS, Reed J, Coupling mechanism of electromagnetic acoustical transducers for ultrasonic generation, *J. Acoust. Soc. Am.* 119 (2006): 2693-2701.

14   Kawashima K, "Theory and numerical calculation of the acoustic field produced in metal by an electromagnetic ultrasonic transducer," *J. Acoust. Soc. Am.* 60(1976), pp1089-1099.

15   Thompson RB, "Mechanisms of electromagnetic generation and detection of ultrasonic Lamb waves in iron-nickel alloy polycrystals," *J. Appl. Phys.* 48(1977) 4942-4950.

16   Thompson RB, "Physical principles of measurements with EMAT transducers," *Physical Acoustics* 19(1990) 157-200.

17   Ogi H, Filed dependence of coupling efficiency between electromagnetic filed and ultrasonic waves, *J Appl. Phys.* 82 (1997), pp3940-3949.

5.   A MODEL FOR PULSED ULRASONIC FIELD OF A PIEZOELECTRIC TRANSDUCER

5.1   Summary

A model has been developed which can be used to calculate the particle velocity waveforms at arbitrary positions in a solid immersed in a fluid when irradiated by a transmitting transducer, launching a short pulse of a longitudinal wave into the fluid. Mode-converted longitudinal and shear waves are generated at the interface between the solid and the fluid. Calculations performed agree well with the results of experimental measurements using a specially-constructed miniature piezoelectric receiving probe. The model constructed has been used to explain the radiation of a transmitting transducer into an immersed solid and it can be used for the optimal design of a transducer and ultrasonic NDT device in immersion mode that has been widely used for ultrasonic imaging and automatic inspection.

5.2   Introduction

Ultrasonic non-destructive testing is widely used for flaw detection, quantitative evaluation and material characterization. Ultrasonic modelling of transducer radiation and flaw scattering is very helpful for explicit physical interpretations of the results of measurements, optimal transducer design and measurement system arrangement [1-12]. In ultrasonic imaging and automatic ultrasonic testing, the immersion mode is widely employed to remove the coupling problem and to enhance the inspection speed [13-18]. It is of particular interest, as a result, to predict the ultrasonic field in the immersion mode.

Ultrasonic radiation from a transmitting transducer in a fluid, a solid directly-coupled and a solid in immersion are totally different in nature. Many models for field prediction and several measurement methods have been reported. In fluids, the ultrasonic field has been thoroughly investigated [3, 8-9, 15], and the analytical solution of the particle velocity field in a solid due to a circular or a square piston has been obtained [3, 8]. In a solid in general, however, such simple analytical solutions are not available. Numerical evaluations are obtained with the finite element method [5, 18] and the finite-difference method [10] which are accurate but extremely time consuming to implement, especially for high frequency wide band pulses [18]. Furthermore, they do not elucidate the physics of the problem and cannot be used to easily predict the dependence of the wave components on the problem parameters [2, 4].

In order to reduce the run time in obtaining valid solutions to such problems, several researchers have developed approximate numerical schemes to treat the situation. Weight has offered a model based on geometrical acoustic considerations to describe pulse propagation in terms of direct longitudinal, edge longitudinal and shear waves [1]. This model incorporates an empirical extension of the impulse-response method developed for fluids [8, 9]. Lhemery refined Weight's results by introducing an approximate integral formula for transient elastic waves which is closely related to the exact Rayleigh integral [7-9] for ultrasonic radiation into the fluid. Gridin and Fradkin used a high-frequency asymptotic approximation to obtain a time-harmonic solution and then performed harmonic synthesis to obtain information on the pulse using a fast Fourier transform [2, 4]. Jian et al have combined analytical solutions and numerical integrals to calculate the ultrasonic field due to the Lorentz force in metals, induced by an Electromagnetic Acoustical Transducer (EMAT) [5]. The force can be of arbitrary spatial distribution in the metal.

Experimental measurements of the ultrasonic field can be used to verify the theoretical predictions made. Jian employed a laser interferometer approach in the measurement of the true displacement generated by EMATs, where this is of the

order of 10 nanometres [5]. Jian et al also used miniature piezoelectric transducers to measure the particle velocity in a solid [17]. Bakker et al have employed an EMAT to measure the incoming bulk waves [13], whilst Jian et al have used an EMAT to measure both in-plane and out-of-plane particle velocities [16-17].

This chapter is organized as follows. In the section of Theory, the integral formula is derived. In a fluid, the analytic and exact solution is known [8] and the particle velocity at the interface might be deemed locally to be plane for a point source in a fluid when the local interface area is small enough, compared to the distance to the point source. Using Mayer's formula [19], the contribution at a spatial point in a solid medium carried by a small source in a fluid is obtained. Integrating over the piston, the total field at the spatial point in the solid is obtained. In the case of normal incidence and being on axis, the particle velocity can be calculated very quickly. In the section of Calculation and Measurement Set-up, the background to the calculation and the measurement setup are discussed. The section of Results presents the calculated results for both normal and oblique incidences, which are compared with the experimental measurements made using a specially constructed miniature receiver [17]. The last section contains conclusions and broad discussion of the significance of the results.

5.3   Theory

5.3.1   Acoustical field in fluid

From the velocity potential, the particle velocity can be expressed by [8],

$$V_\phi(Q,t) = -\nabla \phi(Q,t) \qquad (5.1)$$

where Q is field point, t is tim instance, and Φ is particle velocity potential.

Assuming that a piston is mounted in an infinite planar rigid baffle, which transmits ultrasonic waves into an isotropic fluid half space, the particle velocity at point Q in the fluid is given by [8],

$$\phi(Q,t) = \int_0^t dt_0 \int_\sigma v_0(P,t_0) g(Q,t;P,t_0) ds \tag{5.2}$$

where $v_0(P,t_0)$ is the vibration velocity of the piston at point P. For a piston of uniform vibration in this chapter, $v_0(P,t_0)$ is replaced with $v(t_0)$ in the following. $g(Q,t;P,t_0)$ is the well known Green function for velocity potential at point Q that is generated by the source at point P, given by

$$g(Q,t;P,t_0) = \frac{1}{2\pi} \frac{\delta(t - t0 - |Q - P|/c_w)}{|Q - P|} \tag{5.3}$$

Where c_w is ultrasonic propagation velocity in water.

The particle velocity is given by

$$V_\phi(Q,t) = v_0(t) \otimes V_{\phi,\delta}(Q,t) \tag{5.4}$$

where $\otimes$ is the convolution operator, and

$$V_{\phi,\delta}(Q,t) = -h_\phi(Q,t) \tag{5.5}$$

$$h_\phi(Q,t) = \int_\sigma g_l(Q,t;P,t_0) ds \tag{5.6}$$

where σ is area of surface of active crystal.

$$g_l(Q,t;P,t_0) = -\frac{1}{2\pi c_w} \frac{\delta'(t - t0 - |Q - P|/c_w)}{|Q - P|} n_{PQ} \tag{5.7}$$

where $\boldsymbol{n}_{PQ}$ is the unit vector pointing from point P to point Q.

Considering a field point that is on the axis of a circular piston and z above the piston, the particle velocity is given by

$$V_{\phi,\delta}(Q,t) = \delta(t - \frac{z}{c_w}) - \frac{z}{\sqrt{z^2+a^2}}\,\delta(t - \frac{\sqrt{z^2+a^2}}{c_w})$$

(5.8)

Unlike pressure, the particle velocity of the edge wave has an amplitude smaller than that of a plane wave.

5.3.2   Acoustical field in a solid in immersion

As shown in figure 5.1, both the transducer generating the wave and the solid to be tested are immersed in a fluid (in the most general case, it is water). The longitudinal waves generated by the piston arrive at the interface of the solid and the fluid and ultrasonic wave reflection and refraction occur at the interface. Mode-converted longitudinal and shear waves are generated in the solid half space. A point P on the piston radiates longitudinal waves in many directions. Among them, there are only two paths, PP_lQ and PP_tQ, along which the mode-converted longitudinal and shear waves, respectively at the interface between the solid and the fluid, will reach point Q. Snell's law is observed for these paths [19]. PP_l and PP_t are not necessarily perpendicular to the piston and it is clear that PP_l and PP_t cannot be perpendicular to the piston at the same time.
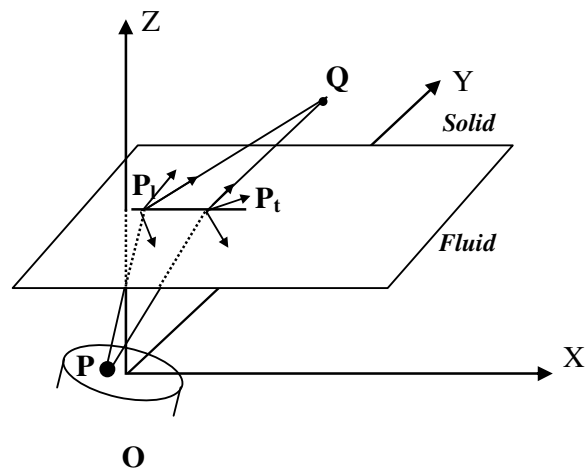
Figure 5.1 Mode-converted longitudinal and shear waves, which are from the same source point *P* on the piston but have different propagation path in the fluid, are received at field point *Q*

The particle velocity of the mode-converted longitudinal and shear waves at point Q in the solid due to the source at point P in a liquid are approximately given by

$$\boldsymbol{g}_l(Q,t;P,t_0) = -\frac{1}{2\pi c_w}\frac{\delta'(t-t0-|P_l-P|/c_w-|Q-P_l|/c_l)}{|P_l-P|+|Q-P_l|}\eta_l(Q,P)\boldsymbol{n}_{P_lQ} \quad (5.9)$$

where c_l is the propagation velocity of the longitudinal wave in the solid, and $\boldsymbol{n}_{P_lQ}$ is the unit vector from point P_1 to point Q, denoting the propagation direction of the refracted longitudinal wave. $\eta_l(Q,P)$ is plane longitudinal wave refraction coefficient in solid at the interface between fluid and solid following the path PP_lQ.

$$\boldsymbol{g}_t(Q,t;P,t_0) = -\frac{1}{2\pi c_w}\frac{\delta'(t-t0-|P_t-P|/c_w-|Q-P_t|/c_t)}{|P_t-P|+|Q-P_t|}\eta_t(Q,P)\boldsymbol{n}_t \quad (5.10)$$

where c_t is the propagation velocity of the shear wave in the solid, $\boldsymbol{n}_t$ is the unit vector of the particle velocity of the shear wave that is perpendicular to the propagation direction of the shear wave denoted by the unit vector, $\boldsymbol{n}_{P_tQ}$. $\eta_t(Q,P)$ is plane shear wave refraction coefficient in solid at the interface between fluid and solid following the path PP_tQ.

The mode-converted longitudinal velocity at point Q, contributed by the whole piston, is given by

$$V_l(Q,t) = \int_0^t v_0(t_0)dt_0\int_\sigma \boldsymbol{g}_l(Q,t;P,t_0)ds \quad (5.11)$$

The mode-converted refracted shear velocity potential at point Q, contributed by the whole piston, is given by

$$V_t(Q,t) = \int_0^t v_0(t_0)dt_0\int_\sigma \boldsymbol{g}_t(Q,t;P,t_0)ds \quad (5.12)$$

Equations 5.11 and 5.12 can be further written, in convolution form, by

$$V_l(Q,t) = v_0(t) \otimes V_{l,\delta}(Q,t) \tag{5.13}$$

$$V_t(Q,t) = v_0(t) \otimes V_{t,\delta}(Q,t) \tag{5.14}$$

where $V_{l,\delta}(Q,t)$ and $V_{t,\delta}(Q,t)$ are called the impulse response of the particle velocity in the solid of the piston radiation which is immersed in fluid, and are defined by

$$V_{l,\delta}(Q,t) = \int_\sigma g_l(Q,t;P,0)ds \tag{5.15}$$

$$V_{t,\delta}(Q,t) = \int_\sigma g_t(Q,t;P,0)ds \tag{5.16}$$

The particle velocity at point Q is the sum of the contributions of the longitudinal waves and shear waves,

$$V(Q,t) = V_l(Q,t) + V_t(Q,t) \tag{5.17}$$

The components of the refracted longitudinal wave and shear wave in a specific direction described by unit vector n_p can be given by

$$V_{pl,\delta}(Q,t) = \int_\sigma g_l(Q,t;P,0) \cdot n_p ds \tag{5.18}$$

$$V_{pt,\delta}(Q,t) = \int_\sigma g_t(Q,t;P,0) \cdot n_p ds \tag{5.19}$$

Considering that a field point is in the plane *XOZ*, the particle velocities of the refracted longitudinal and shear waves are also in the plane *XOZ*. Only the components in the *X*- and the *Z*-axis directions are available and needed to be calculated.

A more special case is where the transmitting transducer is arranged in a position normal to the solid bottom surface and the field point Q is on the axis of the transmitting transducer. Both the refracted longitudinal wave and shear wave have only particle velocity components in the Z-axis direction, and are given by

$$V_{zl,\delta}(Q,t) = -\frac{1}{2\pi c_w} \int_0^a \frac{\delta'(t - |P_l - P|/c_w - |Q - P_l|/c_l)}{|P_l - P| + |Q - P_l|} \eta_l(Q,P) n_{zP_lQ} r dr \quad (5.20)$$

where a is the radius of the transmitting transducer. Because of the symmetry, only the components in Z-axis direction contribute to the total shear wave, and this is given by

$$V_{zt,\delta}(Q,t) = -\frac{1}{2\pi c_w} \int_0^a \frac{\delta'(t - |P_l - P|/c_w - |Q - P_l|/c_l)}{|P_l - P| + |Q - P_l|} \eta_t(Q,P) n_{zt} r dr \quad (5.21)$$

5.4   Calculation and Measurement Set-up

Consider the ultrasonic field in a steel half space that has a density $\rho = 7800 kg/m^3$, a longitudinal wave propagation velocity $c_l = 5850 m/s$ and a shear wave propagation velocity $c_t = 3230 m/s$. The transmitting transducer has a round, active PZT element of diameter 0.75 inch (18 mm). The ultrasonic fields are calculated in this chapter in the case where the piston is normal and oblique to the bottom surface of the solid.

To A/D Board

Constant Press

Pre-amplifier

Jig

Miniature Probe

BNC

Air

Probe Guide

Water

Round hole

Transmitting Transducer
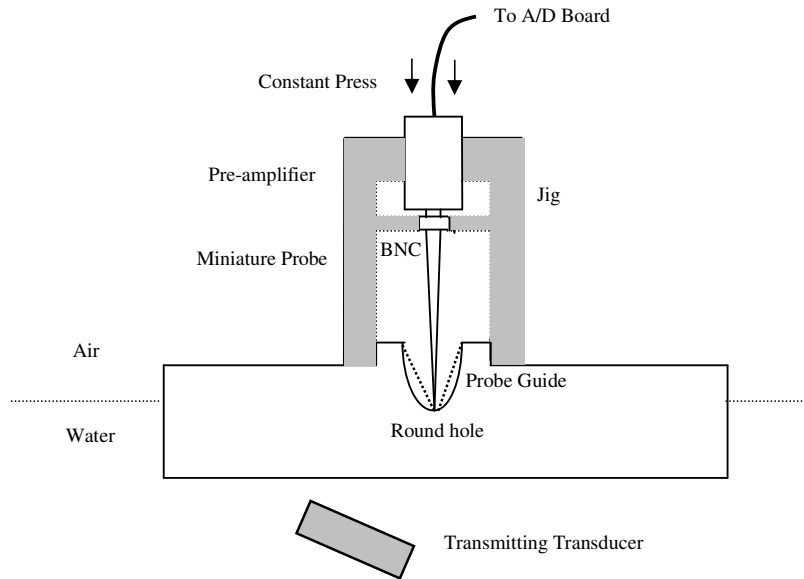
Figure 5.2 Measurement Set-up with miniature probe normal to solid bottom surface

Experimental measurements were carried out to verify the simulations. Four steel samples are made, which are round steel cylinders of diameter 180 mm but of varied thickness. A round-bottomed hole of 10-mm radius was bored into one side of each test sample. As shown in figure 5.2, the test steel piece was half immersed in water while the transmitting transducer was totally immersed in the water on the other side of the test samples.

The ultrasonic fields at the surface of the test samples are measured by employing a miniature probe supported by a specially constructed jig, to avoid coupling problems. The jig was clamped to the test pieces and was not disturbed throughout the course of each set of measurements and the miniature probe was fixed to the jig using four screws.

The tip of the miniature probe was coupled to the bottom of each hole. The function of the hole is to avoid a problem that occurs with some block thicknesses due to the overlapping of the shear edge wave with a multiple reflection (between the two surfaces of the block) of the faster-propagating longitudinal wave. It is most important that the miniature probe is positioned normal to the bottom of the hole. The measured signal should therefore be proportional to the normal component of the particle velocity in an elastic medium [17].

In the measurement, the incident angle of the ultrasonic waves to the test piece was adjustable from 0 to 90 degrees and by rotating the transmitting transducer, it was able to move in 3 dimensions, with the support jig being adjustable in height. Necessary adjustments are carried out until the amplitude of the echo from the bottom surface of the test piece was the same as that reflected from the water surface to ensure that the bottom surface of the test piece is horizontal and parallel to the still water level.

5.5 **Results**

5.5.1 **On axis at normal incidence**

It is assumed that the transmitting transducer is normal to the bottom plane surface of the solid, and the receiving probe is on the axis of the transmitting transducer. It is well known that plane and edge longitudinal waves are excited in a fluid [8]. The incident plane longitudinal waves in the fluid do not excite shear waves in the solid at the interface by mode-conversion. However, the edge longitudinal wave in the water is incident at a non-zero angle; therefore, shear waves can be excited by the longitudinal waves from the piston edge by means of mode conversion.
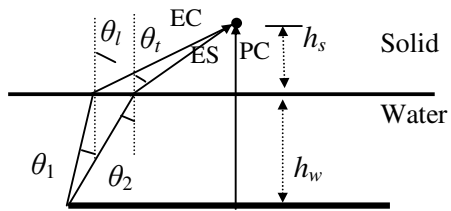
Figure 5.3 Mode-conversed plane longitudinal and edge waves and shear edge wave received at a point on the axis of the piston that is parallel to the solid bottom surface
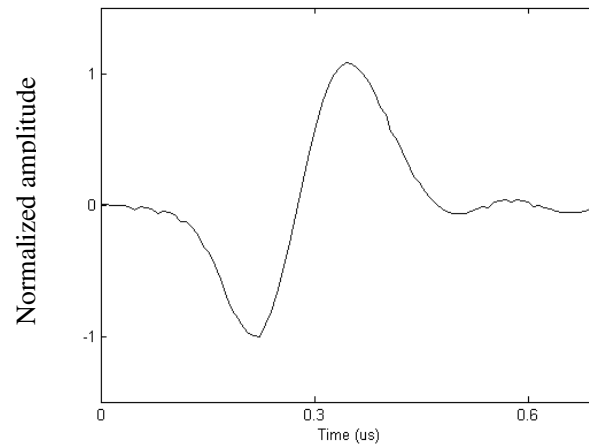
Figure 5.4 Measured particle velocity waveform is used as the vibration function of transmitting transducer ($v_0(t)$) in the calculation in this chapter

Figure 5.3 shows the propagation path of the plane longitudinal and edge waves and the shear edge wave. The arrival times of these three kinds of waves are given, respectively, by

$$t_{lp} = h_w / c_w + h_s / c_l \tag{5.22}$$

$$t_{le} = h_w / \cos\theta_1 c_w + h_s / \cos\theta_l c_l \tag{5.23}$$

$$t_{te} = h_w / \cos\theta_2 c_w + h_s / \cos\theta_t c_t \tag{5.24}$$

where h_w and h_s are the thickness of the water path between the transmitter and the solid, and the thickness of the solid respectively. The corresponding incident and refraction angles in Equations 5.23-5.24 and in figure 5.3 can be calculated by using Snell's law [19], and thus

$$a = h_w \tan\theta_1 + h_s \tan\theta_l \tag{5.25}$$

$$\frac{\sin\theta_1}{c_w} = \frac{\sin\theta_l}{c_l} \tag{5.26}$$

$$a = h_w \tan\theta_2 + h_s \tan\theta_t \tag{5.27}$$

$$\frac{\sin\theta_2}{c_w} = \frac{\sin\theta_t}{c_t} \tag{5.28}$$

The particle velocities only have components in the Z-axis direction and the velocity impulse responses can be calculated by using Equations 5.20-5.21. By means of a convolution operation of the particle velocity impulse response with the vibration temporal function, the particle velocities can be calculated by use of Equations 5.13-5.14. Figure 5.4 shows the vibration temporal function, $v_0(t)$, of the piston in this chapter, which convolves with the particle velocity impulse response to obtain the particle velocity waveform.

Figure 5.5 shows the calculated and measured particle velocity waveforms where the solid is 10 mm thick [17]. The transmitting transducer is normal to the bottom surface of the solid and the receiving miniature probe is on the axis of the transmitting transducer that is normal to the bottom surface of the solid. The water paths change from 48 mm to 6 mm. As the water path increases, θ_1 and θ_2, the incident angles of the edge waves that are mode-converted into longitudinal (EC) and shear waves (ES) decrease. As a result, the refraction coefficient of the longitudinal wave increases, approaching the value at normal incidence (its maximum), whilst the refraction coefficient of the shear wave decreases, approaching the minimum value at normal incidence, which is zero. The difference of the arrival times of the plane longitudinal, the edge longitudinal and the shear wave changes inversely with the water path.
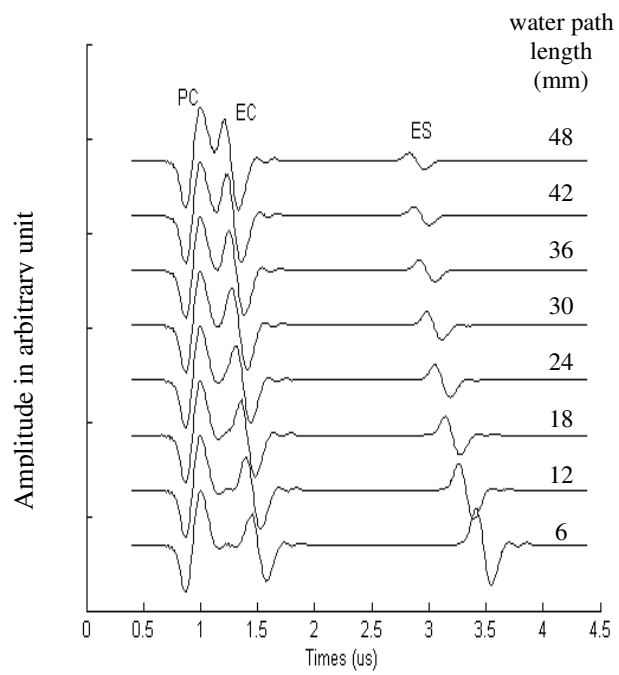
Figure 5.5 Calculated ultrasonic waveforms in solid on axis of the transmitting transducer in normal incidence. The thickness of solid is 10 mm
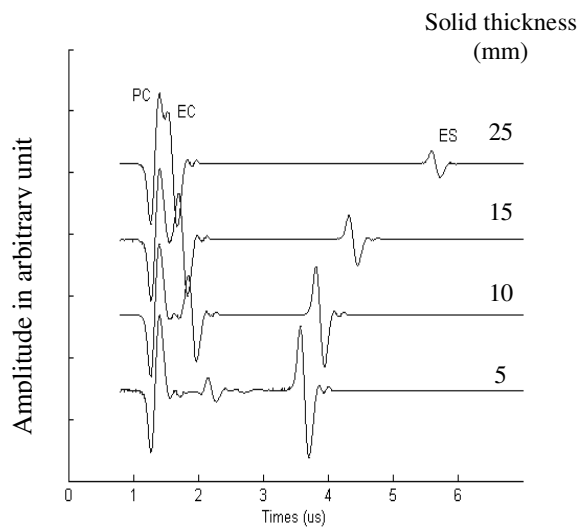
Figure 5.6 Calculated ultrasonic waveforms in solid on the axis of the transmitting transducer in normal incidence. Water path is 6 mm

Figure 5.6 shows the calculated and measured particle velocity waveforms where the water path length is fixed whilst the thickness of the solid changes from 25 mm to 5 mm [17]. When the thickness of the solid is 5 mm, the amplitude of the edge shear wave is much higher than 25 mm, because the refraction coefficient of the edge shear wave at the solid of 5 mm thickness is much greater than that at the solid of 25 mm in thickness.

5.5.2   Oblique incidence

Both the plane longitudinal wave and the plane shear wave in the solid can be generated at the interface of the solid and the fluid, when the incident angle of the plane longitudinal wave in the fluid, or the angle between the normal of the transmitting transducer and the normal of the bottom surface of the solid is smaller than the first critical angle. Only the plane shear wave can be generated when the incident angle is between the first and the second critical angles. In the rare case that the incident angle is larger than the second critical angle, no plane longitudinal and shear wave is available in the solid. However, edge longitudinal and shear waves can always be expected, but their amplitudes are also dependent on the incident angle [17].
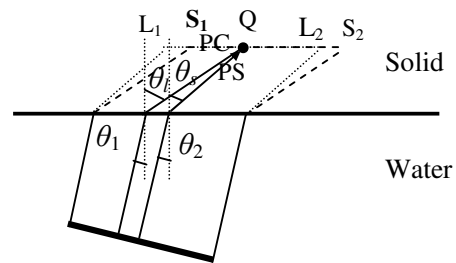
Figure 5.7 Refracted plane longitudinal wave can be detected between L₁ and L₂,
     whilst refracted plane shear wave can be detected between S₁ and S₂. At
     the field point *Q* in this figure, plane longitudinal wave and plane shear
     wave come from different sources on the pistons with same incident angle
     in fluid but different refraction angles in solid.

The amplitudes and arrival times of the four types of waves are dependent on the properties of the solid, the thickness of solid, the water path and the incident angle. Figure 5.7 shows the propagation path of the plane longitudinal wave, the plane shear wave, the edge longitudinal wave and the edge shear wave in the solid. The first arriving longitudinal wave to a field point arising from the plane where the transmitting transducer is located, must be the plane longitudinal wave in the solid that is mode-converted from the plane longitudinal wave that is perpendicular to the piston [17, 19]. Similarly, the first arrival shear wave to a field point arising from the plane where the transmitting transducer is located, must be the plane shear wave in the solid that is mode-converted from the plane longitudinal wave that is perpendicular to the piston [17]. The plane longitudinal and the plane shear waves in the solid can be detected in their own zones L_1L_2 and S_1S_2 respectively, which are partly overlapping with each other, depending on the incident angle of the plane longitudinal wave in the fluid. Outside the zones of corresponding plane waves, the first arrival plane wave, or the plane longitudinal or shear wave cannot be detected. Unlike normal incidence, the maximum edge longitudinal wave is not at the centre of the beam of the plane longitudinal wave in the solid, L_1L_2, neither is the maximum edge shear wave at the centre of the beam, S_1S_2. For oblique incidence, the edge wave can have larger amplitude than the corresponding plane wave. Generally, the edge wave is more sensitive to the detection point than the corresponding plane wave. A small change in its position around the position of the focused edge wave can cause a great change of the edge wave in terms of its amplitude and shape. This property of the edge wave can be used to identify it from the corresponding plane wave.

Usually, the plane and the edge longitudinal waves partially overlap. When measuring the amplitude of the plane wave, caution must be taken to ensure that no edge wave is involved. In an appropriate location near the geometrical centre of the beam of the corresponding plane wave, the first cycle of the plane-longitudinal-wave-excited longitudinal wave never overlaps the edge-longitudinal-wave-excited longitudinal wave. Reasonably accurate estimates of the plane longitudinal or shear wave amplitude can therefore be obtained by confining measurements to the first

half cycle of the plane wave and by arranging the transmitting transducer to ensure the miniature probe is placed at the geometric centre of the beam. Any attenuation of the wave in either the water or the steel can be completely neglected for the frequencies and path lengths used [17].

Figure 5.8 shows the calculated and measured particle velocity waveforms. The thickness of the solid is 10 mm and of the incident angle 12 degrees. The water path is fixed whilst the transmitting transducer moves from creating the focused edge longitudinal wave (*a*) to the focused edge shear waves (*d*). In figure 5.8(*a*) the edge longitudinal wave is high while in figure 5.8(*d*) the edge shear wave is high. The results of the calculations agree well with the measurements made.
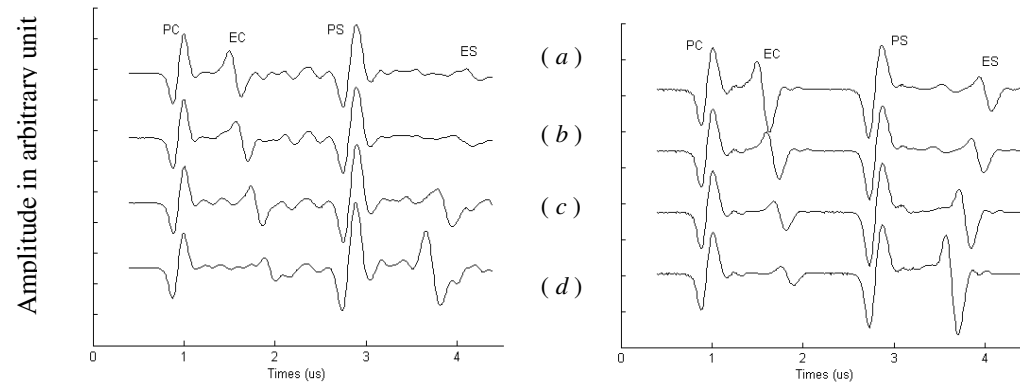
Figure 5.8 The measured (left column) and calculated (right column) waveforms when solid is 10 mm thick and transmitting transducer of incident angle of 12 degree moves from a position of focused edge longitudinal wave (*a*) to a position of focused edge shear wave (*d*) with step of 1.5 mm

5.6   Conclusions and Discussion

The longitudinal waves radiated by a circular transducer in water consist of a plane wave propagating in the geometric region ahead of the source, together with an edge wave that propagates from the rim of the source. The plane longitudinal wave interacts with the interface of water and the solid immersed in the water, and is partly mode-converted into a plane longitudinal wave and a plane shear wave in the solid. Similarly, the edge longitudinal wave in the fluid is partly mode-converted into the edge longitudinal wave and the edge shear wave in the solid.

Due to the difference of the propagation velocities of the longitudinal and the shear waves, the beam of the plane longitudinal wave and the plane shear wave totally overlap with each other at the interface, and separate gradually with increasing distance from the interface. If a spatial point lies in both geometrical regions of the plane longitudinal and the shear wave, both the plane longitudinal and the shear waves are received. If it is outside the geometrical region of the plane wave, then it cannot be received. Since the edge wave from a different source rim of the transducer has a different incident angle (smaller absolutely than the corresponding critical angle), the refraction coefficient of the edge wave will vary. Consequently, the edge wave may be greater than the plane wave of the same type in some cases. A special case is that of normal incidence, where the plane shear does not exist while the edge shear does. As the water path increases, the edge shear wave tends towards zero, approaching the case of shear wave refraction at normal incidence.

A model allows rapid calculations of the particle-velocity waveforms in a solid immersed in a fluid, and explains the origin of the plane and edge longitudinal and shear waves as partial mode conversion of the plane and edge longitudinal wave in a fluid at the interface of the solid and the fluid. Once the field point and the source point on the rim of the transmitting transducer are fixed, there is only one path available for the longitudinal wave, which is governed by Snell's law. When the incident longitudinal wave in the fluid is perpendicular to the surface of transmitting transducer, the refracted longitudinal wave is known as the plane longitudinal wave, or it is the edge longitudinal wave. The plane wave is always the first longitudinal

wave to arrive. The argument is also true for the shear wave, because the longitudinal wave propagates faster than the shear wave, the plane longitudinal wave is the first wave to arrive and to be measured at a field point.

Calculations made using the model agree well with the measured field-point waveforms obtained using specially constructed miniature receiving probes [17]. The plane wave and the edge wave description of the pulsed field have been found useful, since the waves can be time resolved. Such a system is a valuable aid in understanding the pulsed-field structure in the immersion mode and in the optimal design of the transmitting transducer. While only calculated results for a circular piston are given in this chapter, this model can be used for the prediction of the ultrasonic field for a transducer of any shape.

5.7   References

1   Weight, J. P., "A model for the propagation of short pulses of ultrasound in a solid," *J. Acoust. Soc. Am.* 81 (1987), pp815-826.

2   Fradkin L. J., Kiselev, A. P., Krylova E., "The radiating near-field asymptotics of a normal time-harmonic circular ultrasonic transducer in an elastic half-space," *J. Acoust. Soc. Am.* 104(1998), pp1178-1187.

3   Hayman, A. J. and Weight J. P., "Transmission and reception of short ultrasonic pulses by circular and square transducers," *J. Acoust. Soc. Am.* 66(1979), pp945-951.

4   Gridin D., Fradkin L. J., "The high-frequency asymptotic description of pulses radiated by a circular normal transducer into an elastic half-space," *J. Acoust. Soc. Am.* 104(1998), pp3190-3198.

5   Jian, X., Dixon, S., Grattan, K. T. V., Rachel R.S., "A model for pulsed Rayleigh wave & optimal electromagnetic acoustical transducer design," *Sensors & Actuators: A. Physical* 128 (2006), pp *296-304*.

6   Jian X., Dixon S., Edwards R.S., Reed J., "Coupling Mechanism of Electromagnetic Acoustical Transducers for Ultrasonic Generation," *Journal of Acoustics Society of America* 119 (2006).

7   Lhemery, A, "A model for the transient ultrasonic field radiated by an arbitrary loading in a solid," *J. Acoust. Soc. Am.* 96 (1994), pp3776-3786.

8   Stepanishen, P. R., "Transient radiation from pistons in an infinite planar baffle," *J. Acoust. Soc. Am.* 49 (1971), pp1629-1638.

9   Stepanishen, P.R., "An approach to computing time-dependent interaction forces and mutual radiation impedances between pistons in a rigid planar baffle," *J. Acoust. Soc. Am.* 49(1971), pp283-292.

10   Ilan, A. and Weight, J. P., "The propagation of pulses of ultrasound from a circular source coupled to an elastic half-space," *J. Acoust. Soc. Am.* 88(1990), pp1142-1151.

11   Bresse, L.F. and Hutchins, D.A., "transient generation of elastic waves in solids by a disk-shaped normal force source," *J. Acoust. Soc. Am.* 86 (1989), pp810-817.

12   Mair, H.D., Bresse, L. and Hutchins, D.A., "Diffraction effects of planar transducers using a numerical expression for edge waves," *J. Acoust. Soc. Am.* 84 (1988), pp1517-1525.

13   Bakker, M. C. M. Bakker and Verweij, M. D., "Experiment validation of two elastodynamic models for the wave field generated by ultrasonic transducer," *J. Acoust. Soc. Am.* 113(2003), pp1850-1862.

14   Stepanishen, P. R., Fisher, G., "Experimental verification of the impulse response method to evaluate transient acoustic fields," *J. Acoust. Soc. Am.* 69 (1981), pp1610-1617.

15   Weight, J. P. and Hayman, A. J., "Observations of the propagation of very short ultrasonic pulses and their reflection by small targets," *J. Acoust. Soc. Am.* 63 (1978), pp396-404.

16   Jian, X., Dixon, S. and Palmer, S. B., "In-plane and out-of-plane particle velocity using electromagnetic acoustical transducers," Proceeding of *IEEE Ultrasonic Symposium* 2005.

17   Jian, X., Weight, J. P., Grattan, K. T. V., "Measurement of longitudinal and transverse waves of pulsed ultrasound in solid media with miniature probe," *Sensors & Actuators: A. Physical* 127 (2006), pp 13-23.

18   Jian, X., Fan, Y., Edwards, R. S. and Dixon, S., "Surface-breaking crack gauging with the use of laser-generated Rayleigh waves," Submitted to *J. Appl. Phys*, 2005.

19   Mayer, W. G., "Energy partition of ultrasonic waves at flat boundaries," *Ultrasonics* 3 (1965), pp62-68.

6. A MODEL FOR EMAT ULTRASONIC FIELD AND EMAT OPTIMIZATION

6.1 Summary

A model has been developed for the prediction of the transient displacement of a Rayleigh wave generated by an Electromagnetic Acoustic Transducer (EMAT), operating on the Lorentz principle. This model can be used to calculate Rayleigh waves of arbitrary forces. A linear coil and a spiral coil are considered as two examples. Out-of-plane displacement of the Rayleigh wave is measured experimentally using a Michelson laser interferometer. Good agreement is observed between the calculated and the measured results, demonstrating the value of this method. This chapter explains how the Lorentz forces due to the static and dynamic magnetic fields work constructively and destructively, indicating that the orientation of the external magnetic field must be correct to achieve an efficient generation of the Rayleigh wave.

6.2 Introduction

Conventional contact ultrasonic techniques require direct physical contact or the use of a coupling medium between the sample and the transducer to allow the ultrasonic waves to penetrate the sample [1]. The contact approach can suffer from very variable contact conditions and care must be taken if this variation is not to corrupt the physical measurements being made. In addition, it is not always practical to use contact techniques, particularly where the sample may be moving relative to the transducer or in situations where the environmental conditions are hostile, such as at elevated temperatures. There are various non-contact alternatives for generating and detecting ultrasound, including laser based approaches and Electro-Magnetic Acoustic Transducers (EMATs) [2-16].

EMATs offer a non-contact, non-destructive evaluation (NDE) method. They can be rapidly scanned across a sample as there is no acoustic coupling medium, which is especially desirable in on-line or hostile environmental measurement conditions. As the coupling between the EMAT and the sample is electromagnetic, they are relatively insensitive to misalignment when compared to contact methods. EMATs can be designed to generate a range of specific wave modes such as the Rayleigh wave, Lamb wave and Shear Horizontal (SH) wave.

EMATs can generate or detect ultrasound in electrically conductive or magnetic materials through the Lorentz force principle or by magneto-elastic effects. In this chapter, work has been limited to investigating non-magnetic metals where the operation of the EMAT is due to the Lorentz force mechanisms alone [2, 4-16]. Wideband generation is also considered where the EMAT is driven by a broadband pulse of current, rather than a single frequency or pseudo single frequency (tone burst) pulse. When a current is pulsed through an EMAT coil, eddy (or mirror) current is induced within the skin depth. The electrons that make up this eddy current experience a Lorentz force under the interaction with the dynamic magnetic field from the coil itself and if present, also with the external static magnetic field. Considerable research effort has been devoted to study the underlying physical principles of these EMATs for a wide variety of configurations and applications [2, 4-16]. Most of the analytical treatments to quantify the EMAT transduction phenomena are based on time-harmonic far-field derivations [2, 9-11], and simplifying assumptions with regard to the underlying constitutive relations arising from the coupling between the elastic and electromagnetic fields, the induced field distribution, and elastic-wave generation and propagation mechanisms.

Due to the complexity of the problem, an analytical solution is only available for some simple uniform force distributions, such as uniform normal piston force and radially acting ring force [17-18]. Accordingly, transient field studies have generally been carried out by using Finite Element Method (FEM) [14-16]. In much of the previous research, the Lorentz force contribution due to the dynamic magnetic field from the coil itself has been ignored. It is usually assumed that the dynamic magnetic field is much smaller than that of the external static magnetic field, so the

Lorentz force due to the static magnetic field should be much bigger than that due to the dynamic magnetic field. Accordingly, it has been argued that the ultrasonic field generated by the latter could be neglected to allow a simplification of the problem.

The disadvantages of a fully numerical calculation are that it lacks an explicit physical interpretation of the relationship between the source and its resulting ultrasonic field and it also requires access to huge computer resources for a 3-D problem because the mesh requirements for the Lorentz force calculation and for the ultrasonic field calculation are different [14-16].

In this chapter, numerical calculations and analytical solutions are combined to compute Rayleigh waves generated by EMATs. The FEM is applied to calculate the transient force distribution generated by an EMAT and then the force is decomposed into many force components for which analytical solutions exist. Finally the sum of the displacements generated by each of these components is calculated to obtain the total displacement field. The analysis of the contribution of the Lorentz forces due to dynamic magnetic field (mainly out-of-plane component down to the sample) and due to the static magnetic field explains the constructive and destructive interference of forces and helps the understanding of the novel experiment results [2]. A Michelson laser interferometer is used to measure out-of-plane displacement and a good agreement between the results of calculations and experiments has been observed. It is found that the contribution of the Lorentz force due to the dynamic magnetic field is larger than that of the Lorentz force due to the static magnetic field in the generation of the Rayleigh wave, contrary to some previous reports [15-17].

6.3   Method

When time varying current is passed through a coil above a sample surface, the electromagnetic waves emitted from the coil will induce an eddy current in the

sample within the skin-depth which is roughly one wavelength of the radio frequency electromagnetic wave thickness [2]. A dynamic magnetic field is present at the surface of the sample below the coil. This dynamic magnetic field can interact with the induced eddy current via the Lorentz mechanism. The resulting Lorentz force always acts in such a way as to try to move the sample away from the exciting coil. There is also an in-plane Lorentz force present that is usually much smaller than the out-of-plane Lorentz force. The dynamic magnetic field and eddy current are, to a good approximation, independent of the external static magnetic field. In the presence of an external static magnetic field, the interaction of the eddy current with the static field produces an additional Lorentz force contribution which is equal to the cross product of the eddy current vector and the external static magnetic field. This is the Lorentz force component that is often considered to be solely responsible for ultrasonic generation using EMATs.

6.3.1   Lorentz Force Distribution

Figure 1 shows the experimental arrangement used, demonstrating the directions of the pulsed current flowing in a linear coil and a spiral coil, which applies in the calculations and measurements in this chapter. B_s is a static magnetic field, and J_0 and J_e are the excitation current and eddy current respectively. F_d and F_s are the Lorentz forces due to dynamic and static magnetic fields respectively. The XZ plane is parallel to the sample surface, with the origin on the surface below the exciting current. The Z-axis is directed out of the page. It is assumed that the external static magnetic field is in the negative Y-direction, while the exciting current is in the Z-direction.

An eddy current is excited in the metal sample, and under the interaction with the external static magnetic field and the dynamic magnetic field, a Lorentz force is produced, as shown in figure 6.1. The Lorentz force is given by

$$\boldsymbol{F} = \boldsymbol{F}_s + \boldsymbol{F}_d \tag{6.1}$$

A vector magnetic potential A, is defined by

$$B_d = \nabla \times A \tag{6.2}$$

where B_d is the dynamic magnetic field. Partial differential equations in all three media are obtained. In the coil of exciting current pulse [2, 10-16],

$$\nabla^2 A - \mu\sigma \frac{\partial A}{\partial t} = -\mu J_0 \tag{6.3}$$

In a sample to be tested,

$$\nabla^2 A - \mu\sigma \frac{\partial A}{\partial t} = 0 \tag{6.4}$$

and in the air surrounding coil and sample,

$$\nabla^2 A - \mu\varepsilon \frac{\partial^2 A}{\partial t^2} = 0 \tag{6.5}$$
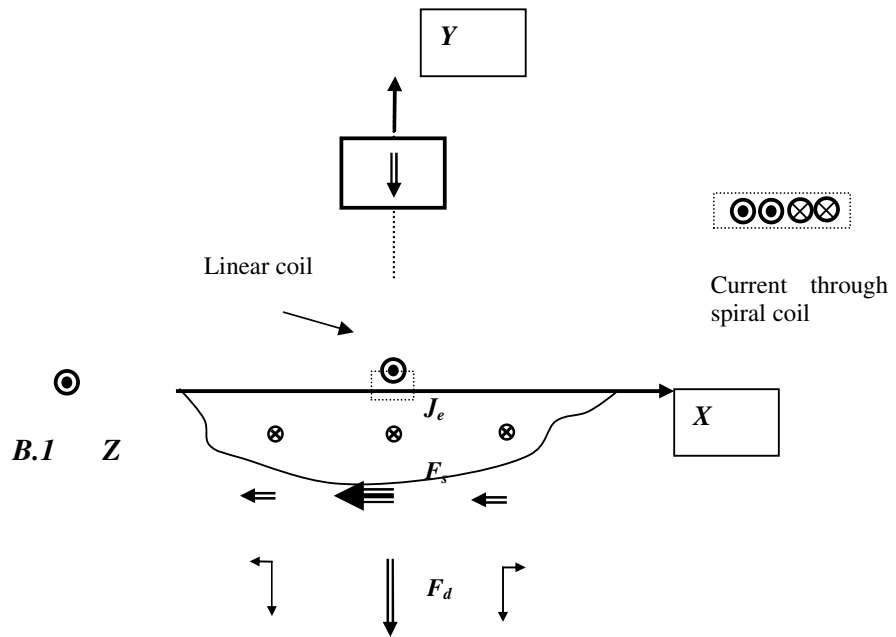
Figure 6.1 Experimental arrangement, showing excitation currents J_0 through a linear coil and a spiral coil

Assuming that the exciting current is only in the Z-direction, the vector potential A has a component in Z-direction only (A_z). For simplicity A is still used here for A_z. Solving Equations 6.3 to 6.5 by use of the FEM, the potential, A may be obtained. The induced eddy current in the metal sample is given by,

$$J_e = -\sigma \frac{\partial A}{\partial t} \tag{6.6}$$

Consequently, the Lorentz forces due to the static and dynamic magnetic fields are given respectively by,

$$F_s = J_e \times B_s \tag{6.7}$$

$$F_d = J_e \times B_d \tag{6.8}$$

Taking the direction of the eddy current and the magnetic fields (static & dynamic) into account, Equation 6.7 and 6.8 can be rewritten as,

$$F_s = -J_e \vec{k} \times (B_{sx}\vec{i} + B_{sy}\vec{j}) = J_e B_{sy}\vec{i} - J_e B_{sx}\vec{j} \tag{6.9}$$

$$F_d = -J_e \vec{k} \times (B_{dx}\vec{i} + B_{dy}\vec{j}) \cong -J_e B_{dx}\vec{j} \tag{6.10}$$

where i and j are unit vectors in X- and Y-directions respectively.

It should be noted that Equation 6.9 is an approximation, since the magnitude of the in-plane dynamic magnetic field is about one tenth of the out-of-plane dynamic magnetic field for general EMAT applications in NDE. Thus the Lorentz force due to the dynamic magnetic field is mainly in the negative Y-direction. The eddy current J_e is either parallel to or inverse to the exciting current J_0. Either J_0 or B_s changing in direction will result in a reverse of the Lorentz force F_s. However, if both J_0 and B_s change together, F_s will not change. One point to note is that the directions of the out-of-plane and in-plane Lorentz force F_d due to the dynamic

magnetic field are independent of the exciting current, and the force always acts in such a way as to attempt to move the sample away from the exciting coil.

In typical EMAT configurations for NDE applications where the frequency is of the order of several hundreds of kHz to a few MHz, the Lorentz force due to the dynamic field may be larger than the Lorentz force due to the static magnetic field. This, of course, depends on the size of the static field, the current through and the design of the EMAT coil, and the stand-off between the coil and the sample. In general, ignoring the Lorentz force due to the dynamic magnetic field from the EMAT coil itself is an unsafe assumption.

6.3.2   Rayleigh Wave Generation

Solutions to Lamb's problem for point, linear and ring sources are available in the published literature [17-21]. For a uniform piston of radius r_0 vibrating with time dependence of $f(t)$ mounted on half-space, the ultrasonic bulk wave displacement in a half-space has been calculated [17-21]. By allowing the field point to approach the surface of the half-space, the out-of-plane and the radial in-plane displacement on the surface at a distance r from the piston centre are given by [17-21],

$$U_y(r,t) = \frac{2r_0 f(t)}{\pi^2} * Im \int_0^\pi \frac{r_0 - r\cos\theta}{\rho} d\theta \int_0^{\frac{\pi}{2}} \frac{\alpha}{c_s{}^2 R(\xi)} \frac{\partial \xi}{\partial t} \cos\phi d\phi \qquad (6.11)$$

$$U_r(r,t) = \frac{2r_0 f(t)}{\pi^2} * Re \int_0^\pi \cos\theta d\theta \int_0^{\frac{\pi}{2}} \frac{\xi(\xi^2 + \beta^2) - 2\xi\alpha\beta}{R(\xi)} \frac{\partial \xi}{\partial t} d\phi \qquad (6.12)$$

Similarly, an expression for a radially acting ring force is given by [17-21],

$$U_y(r,t) = \frac{2r_0 f(t)}{\pi^2} Re \int_0^\pi d\theta \int_0^{\frac{\pi}{2}} \frac{\alpha\xi}{c_s{}^2 R(\xi)} \frac{\partial \xi}{\partial t} d\phi \qquad (6.13)$$

$$U_r(r,t) = \frac{2r_0 f(t)}{\pi^2} \text{Im} \int_0^\pi \frac{r_0 - r\cos\theta}{\rho} d\theta$$

$$\int_0^{\frac{\pi}{2}} \frac{\xi^2 [(\xi^2 + \beta^2) - 2\alpha\beta]}{R(\xi)} \frac{\partial\xi}{\partial t} \cos\phi d\phi \tag{6.14}$$

In Equations 6.11-6.14, $R(\xi)$ is the Rayleigh function [17-21] and given by

$$R(\xi) = (\xi^2 + \beta^2)^2 - 4\xi^2\alpha\beta \tag{6.15}$$

where

$$\alpha = \sqrt{\xi^2 + \frac{1}{c_p^2}} \tag{6.16}$$

$$\beta = \sqrt{\xi^2 + \frac{1}{c_s^2}} \tag{6.17}$$

The variable ξ is defined by

$$\xi = i\frac{t}{\rho\cos\phi} \tag{6.18}$$

The derivative of ξ is easily obtained by

$$\frac{\partial\xi}{\partial t} = i\frac{1}{\rho\cos\phi} \tag{6.19}$$

where the variable ρ is defined by

$$\rho = \sqrt{r_0^2 + r^2 - 2r_0 r\cos(\theta)} \tag{6.20}$$

c_p and c_s are the phase velocity of the longitudinal and the shear waves.

6.3.3 Ultrasonic Field generated by EMATs

The Lorentz force of a spiral coil can be assumed to be of cylindrical symmetry, and be decomposed into many uniform normal piston forces and radial ring sources of different radii for which analytical solutions are available, albeit the in-plane and out-of-plane components of the Lorentz forces generally are not uniform normal piston forces or radial ring forces. For a linear coil of variable coil width, the force can be decomposed into many line forces at different positions. However, if a practical coil does not permit such a decomposition of the force, the force may be decomposed into many point forces, but this requires considerably greater computation time.

The Lorentz forces are calculated by using the FEM. The induced eddy current amplitude decreases exponentially with depth, and exists mainly within the skin-depth. The Lorentz forces therefore need only be considered close to the sample surface. In this chapter, the force within 0.01 mm of the sample surface along the *X*-direction for the linear coil or the radial direction for a spiral coil are calculated and used to determine the Rayleigh waves.

Lorentz force decomposition is based on the Lorentz force distribution that is dependent on the coil configuration. For example, the Lorentz force of a linear coil is decomposed into many line sources whilst the Lorentz force of a spiral coil may be decomposed into many uniform normal piston forces and radially-acting ring forces. Figure 6.2 shows how the spatial out-of-plane Lorentz force of a spiral coil may be decomposed schematically into six uniform normal piston forces.

Assuming the Lorentz force is decomposed spatially into *N* force components, the ultrasonic displacement resulting from the i_{th} force component acting with a delta temporal function may be expressed by u_i^{δ}. The total displacement for these temporal delta forces of a linear coil is given by,

$$u^{\delta}(t, x, y = 0, z) = \sum_{i=1}^{N} u_i^{\delta}(t, x, y = 0, z; x_i, y_{\max}) \tag{6.21}$$

where (x, y, z) are the coordinates of field point to be considered, x_i is the position of the i_{th} line force component in X-direction, and y_{max} is the depth in the metal sample where the maximum Lorentz force is observed. Similarly, the total displacement for these temporal delta force components of the circular sources (uniform normal piston forces or radially acting ring forces) is given by,

$$u^\delta(t, x, y = 0, z) = \sum_{i=1}^{N} u_i^\delta(t, x, y = 0, z; r_i, y_{max})$$ (6.22)

where r_i is the radius of uniform piston or ring force components and y_{max} is the depth in the metal sample where the maximum Lorentz force is observed. Assuming that the Lorentz force produced by the EMAT is of temporal function $f(t)$, the total displacement is given by

$$u^f(t, x, y = 0, z) = f(t) \otimes u^\delta(t, x, y = 0, z)$$ (6.23)

where $\otimes$ denotes a convolution operation.
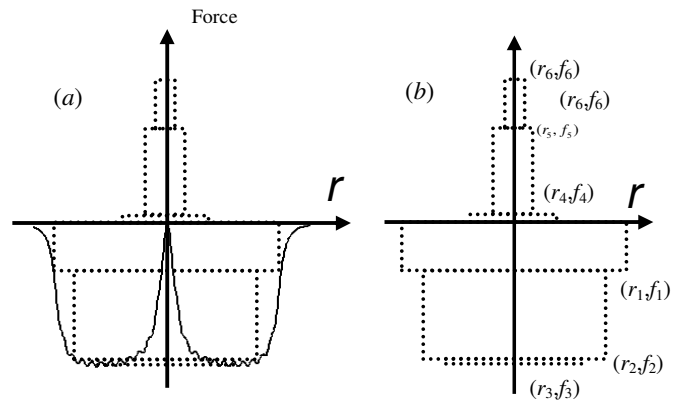
Figure 6.2 Decomposition of out-of-plane Lorentz force (*a*) of a spiral coil into 6 uniform normal piston forces (*b*)

6.4　　Results

A linear coil of 40 mm in length and 2 mm in width and an evenly-wound spiral pancake coil of radius of 5 mm are fabricated using insulated copper wires of radius 0.15 mm. A static magnet that supplies an out-of-plane magnetic flux density of 0.39 Tesla or an in-plane magnetic flux density of 0.16 Tesla was also applied. A large Aluminium block that has density of 2700 kg/m^3, longitudinal wave speed of 6300 m/s and shear wave speed of 3100 m/s was used in the calculation and measurement in this chapter. The Lorentz forces induced by the two coils due to the static and dynamic magnetic fields are calculated, which can be perpendicular or parallel to each other, dependent on the orientation of the static magnetic field. The Rayleigh waves generated by the spiral coil in a large aluminium block were calculated and the displacements of Rayleigh waves in the same side of the EMATs are measured using a Michelson laser interferometer. The measured and the calculated results are compared to each other to validate the method previously.

6.4.1　　Lorentz force calculation by FEM

The measured excitation current is shown in figure 6.3. The excitation current is dependent on the sample, the lift-off, the pulse generator and the coil [2]. The external static magnetic flux density is assigned as

$$
\boldsymbol{B}_s = \begin{cases} -\boldsymbol{B}_j \boldsymbol{j} \\ \boldsymbol{B}_j \boldsymbol{j} \\ -\boldsymbol{B}_i \boldsymbol{i} \\ \boldsymbol{B}_i \boldsymbol{i} \end{cases} \tag{6.24}
$$

where $\boldsymbol{i}$ and $\boldsymbol{j}$ are unit vectors in *X*- and *Y*-directions respectively, $\boldsymbol{B}_j = 0.39$ Tesla and $\boldsymbol{B}_i = 0.16$ Tesla.

Figures 6.4 & 6.5 show the calculated Lorentz forces due to the static magnetic field and due to the dynamic magnetic field respectively generated by a linear coil. As expected, the Lorentz forces due to the static magnetic field shown in figure 6.4 change with static magnetic field whilst the Lorentz forces due to dynamic magnetic field shown in figure 6.5 are independent of static magnetic field. As shown in figure 6.5, the directions of the forces due to the dynamic magnetic field are independent of the direction of the excitation current flowing in a coil, but the magnitudes of the forces are related to the excitation current through the coil.

Figure 6.6 shows the normalized Lorentz force at a position 0.01 mm below the sample surface, generated by the spiral coil and the linear coil where the static magnetic field is in the negative *Y*-direction. Lines "spiral d" and "spiral s" are the Lorentz force components generated by the spiral coil, denoting the Lorentz forces in the negative *Y*-direction due to the dynamic magnetic field, and the Lorentz force along the *X*-direction due to the static magnetic field. Lines "linear d" and "linear s" are the Lorentz force generated by the linear coil, denoting the Lorentz force in the negative *Y*-direction due to the dynamic magnetic field, and the Lorentz force in negative *X*-direction. The Lorentz forces for both the spiral coil and the linear coil along the *X*- direction are not displayed here because they are much smaller than the Lorentz force in the negative *Y*-direction due to the corresponding dynamic magnetic field.
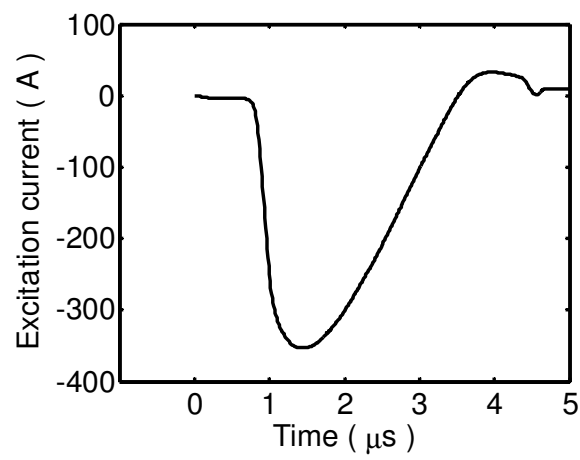
Figure 6.3 Measured excitation current through coil. For clarity, the figure is to an arbitrary time origin
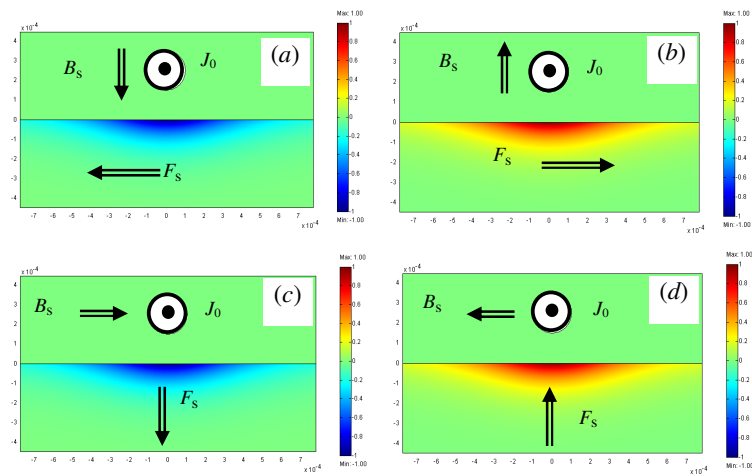
Figure 6.4 Calculated Lorentz forces due to static magnetic field when static magnetic field at time instant 1.3 μs generated by the linear coil when static magnetic field is arranged in negative *Y*-direction (*a*), *Y*-direction (*b*), *X*-direction (*c*) and negative *X*-direction (*d*) respectively. The maximum Lorentz forces in the sample are normalized
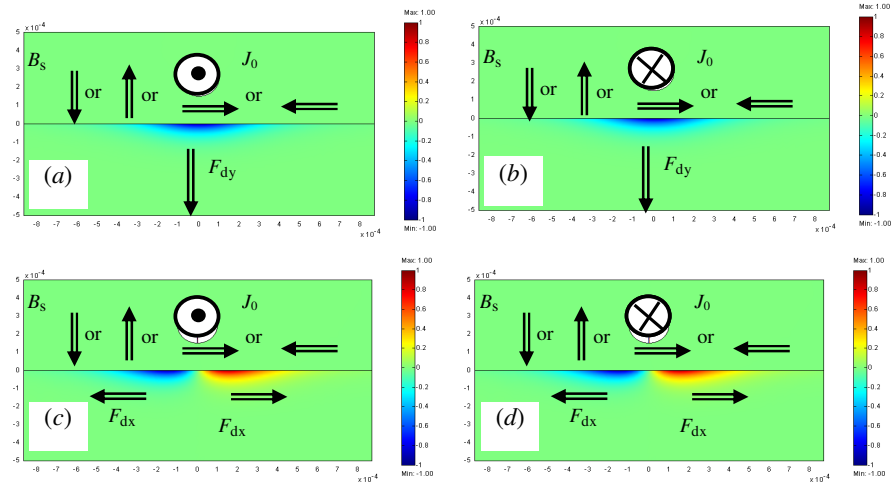
Figure 6.5 Calculated Lorentz forces of the linear coil due to dynamic magnetic field with different directions (Negative *Y*-, *Y*-, *X*- and negative *X*-direction) of static magnetic field. The direction of the Lorentz force due to dynamic magnetic field is independent of static magnetic field and the direction of the excitation current flowing in the coil. The maximum Lorentz forces in the sample are normalized.
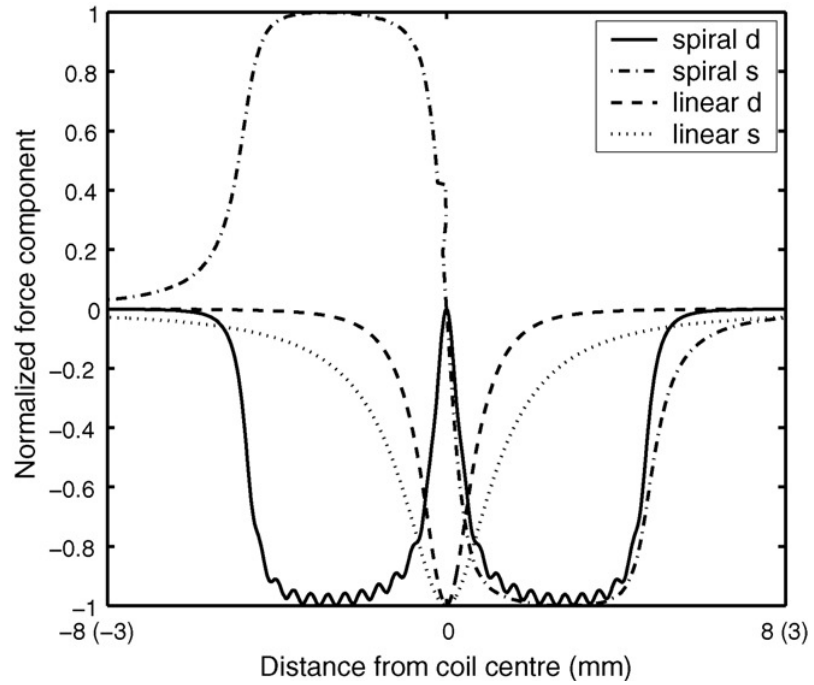
Figure 6.6 Normalized Lorentz force components at 0.01mm below the sample surface for a spiral coil of radius 5mm (solid line, and dashed and dotted line) and a narrow linear coil (dashed line and dotted line)

6.4.2   Rayleigh wave of a spiral coil

Considering the spiral coil of radius 5 mm, the calculated Rayleigh waves are shown in figure 6.7. When the static magnetic field is in the *Y*-direction, the Lorentz force due to the static magnetic field is inward to the coil center radially. When the static magnetic field is in the negative *Y*-direction, the Lorentz force due to the static magnetic field is outward and acts radially away from coil center. When the in-plane force due to the static magnetic field is radially inward to the center, the generated Rayleigh waves are larger than those in the absence of the static magnetic field. However, when the in-plane force due to the static magnetic field is outward and away from the coil center radially, the generated Rayleigh waves are smaller than those in the absence of the static magnetic field.
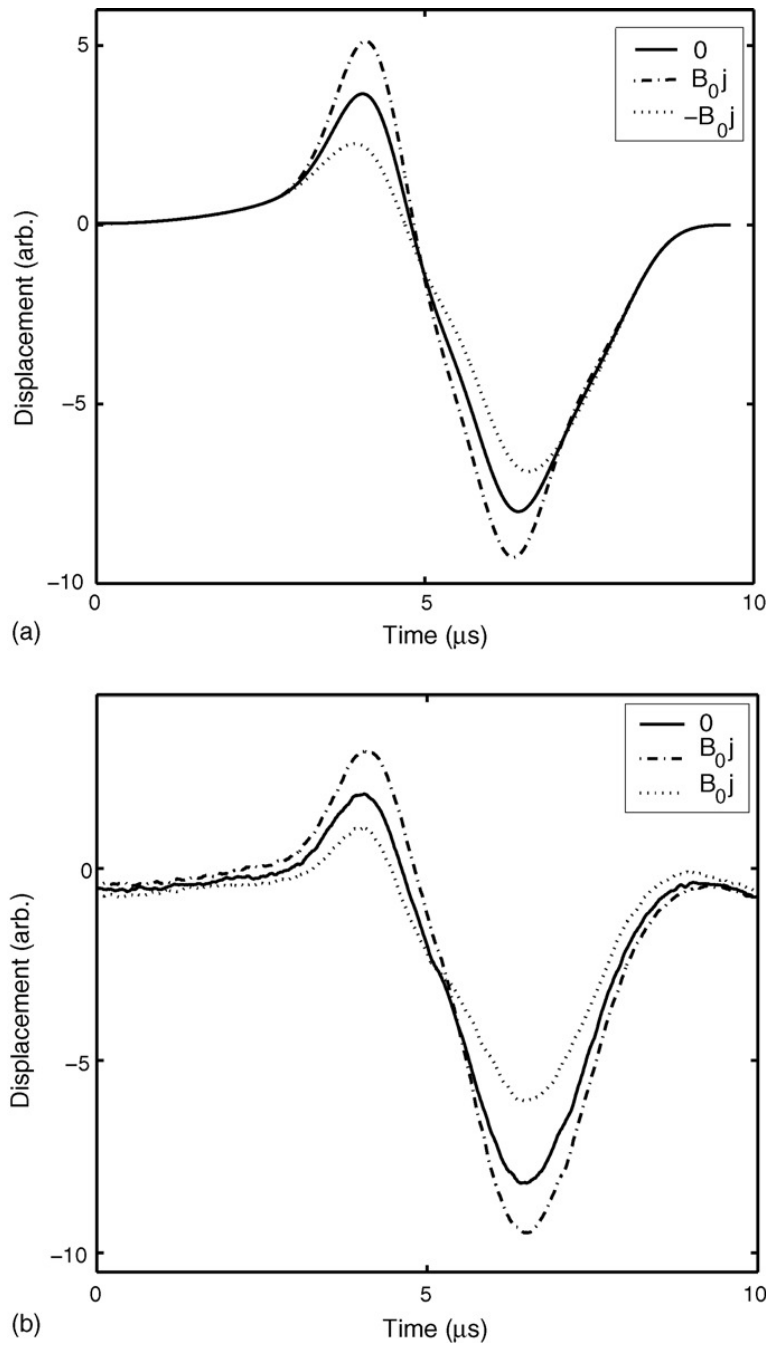
Figure 6.7 Calculated (a) and measured (b) Rayleigh wave at a point of 36mmfrom the coil axis, generated by a spiral coil. The static magnetic field is along *Y* direction generating the Lorentz force along the *X*-direction. For clarity, each plot is to an arbitrary time origin

The amplitude difference between the Rayleigh waves with the presence and the absence of the static magnetic field is much smaller than the amplitude of the Rayleigh wave in the absence of the static magnetic field, indicating that the contribution of the Lorentz force due to the static magnetic field is smaller than that due to the dynamic magnetic field. Ignoring the contribution of the Lorentz force due to the dynamic magnetic field is problematic. The Lorentz force due to the dynamic magnetic field and the static magnetic field may arise constructively or destructively. This is a particularly important result as it explains the experimental observations that had previously been reported by the authors [2], that the orientation of the static magnetic field had a significant influence on the amplitude of the generated Rayleigh wave.

6.4.3   Experimental validation

The Rayleigh waves in a thick aluminium block generated by the spiral coil were measured using a Michelson laser interferometer, and shown in figure 6.7. The measurement set-up is shown in figure 6.8. The advantage of using the interferometer is that the result is independent of the receiver and can be scaled to a true displacement [1-2].
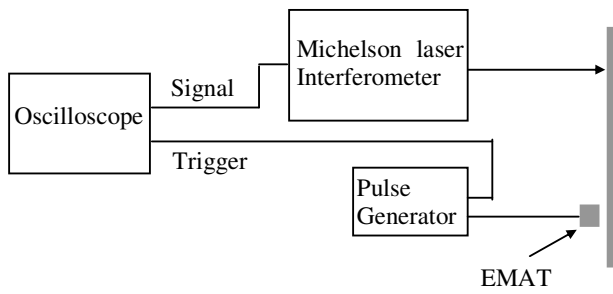
Figure 6.8 Displacement measurement set-up using Michelson laser interferometer

The measured Rayleigh waves shown in figure 6.7(b) agree well with the calculated Rayleigh waves shown in figure 6.7(a) in the three cases, in the absence static of the magnetic field, and in the presence of the static magnetic fields in the *Y-* and the negative *Y-*directions.

6.4.4   Symmetry of the ultrasonic field

Figure 6.9 schematically shows the Lorentz forces due to the dynamic magnetic field and due to the static magnetic field which can be perpendicular or parallel to the sample surface for a linear coil (figure 6.9(*a*) & (*b*)) and a spiral coil (figure 6.9(*c*) & (*d*)). The ultrasonic field generated by a linear coil can be symmetrical when the static magnetic field is parallel to the sample plane surface, as shown in figure 6.9(*b*), or is not symmetrical when the static magnetic field is perpendicular to sample surface, as shown in figure 6.9(*a*).

Figure 6.10 shows the measured Rayleigh waves at the opposite sides of the linear coil. The Rayleigh wave in the *X-*direction in the presence of the static magnetic field in the negative *Y-*direction is similar to that in the negative *X-*direction in the presence of the static magnetic field in the *Y-*direction. The measured Rayleigh waves agree with the contribution of the combined Lorentz forces due to the dynamic magnetic field and the static magnetic field, schematically shown in figure 6.9(*a*). When the static magnetic field is in the *X-*direction as shown schematically in figure 6.1, the Lorentz force due to the static magnetic field is in the negative *Y-*direction and is the same as that of the Lorentz force due to the dynamic magnetic field, constructive generation of Rayleigh waves is expected. When the static magnetic field is in the negative *X-*direction, the forces due to the dynamic magnetic field are opposite to that due to the static magnetic field, and as a result, destructive generation of Rayleigh waves is expected.

The ultrasonic field generated by a spiral coil can be symmetrical when the static uniform magnetic field is perpendicular to the sample plane surface, as shown in

figure 6.9(*c*), or is not symmetrical when a static uniform magnetic field is parallel to the sample surface, as shown in figure 6.9(*d*).
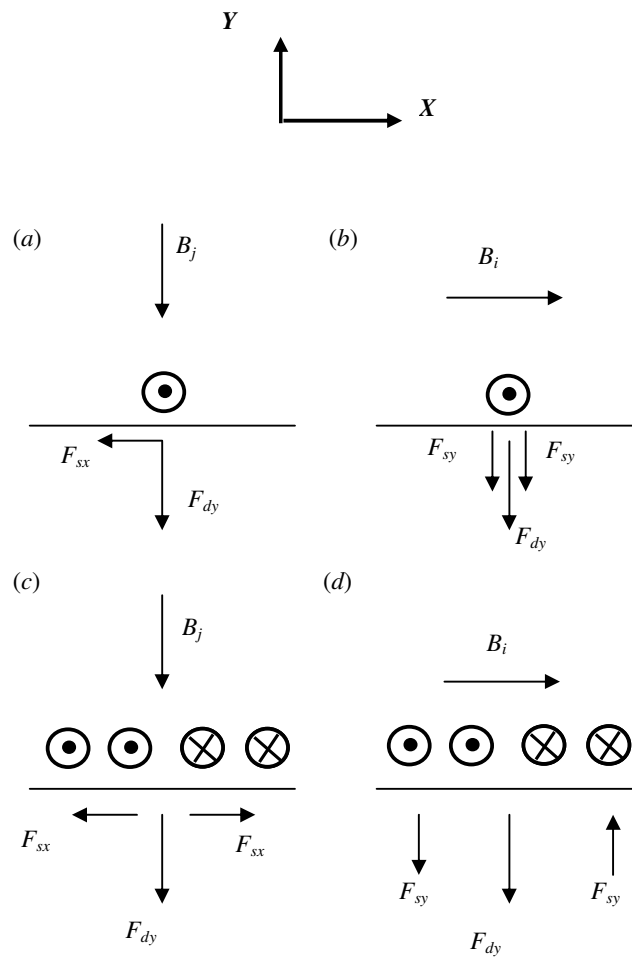
Figure 6.9 Lorentz forces of a linear coil are of non-symmetry (*a*) and symmetry (*b*) over its middle. The Lorentz forces of a spiral coil are of symmetry (*c*) and non-symmetry (*d*) over its axis

(a)

(b)
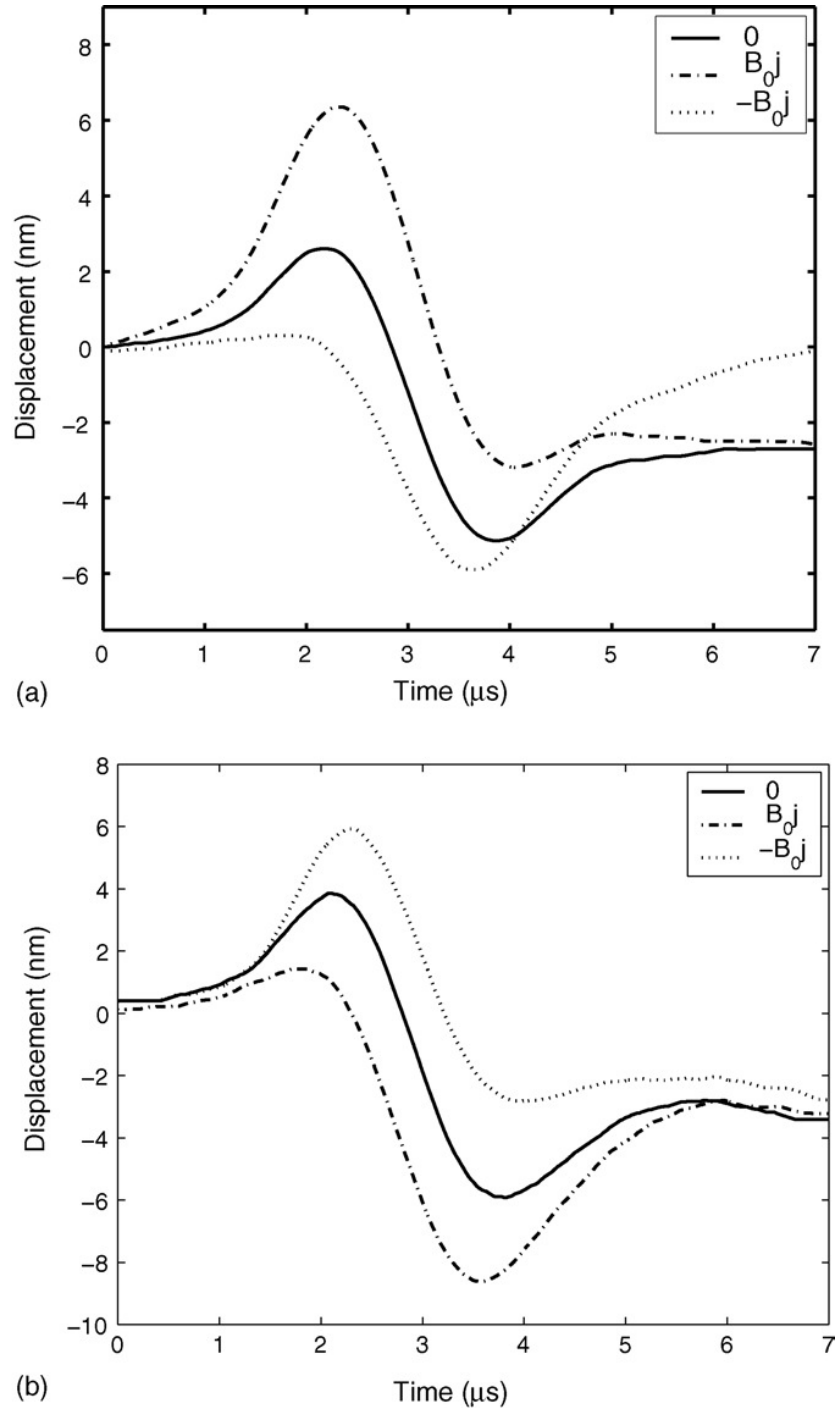
Figure 6.10 Measured Rayleigh wave at a point in *X*-direction (a) and at a point in negative *X*-direction (b) respectively, demonstrating the ultrasonic field is not of symmetry over the middle of the linear coil when static magnetic field is along the *Y*-direction. For clarity, each plot is to an arbitrary time origin

6.5 Discussion and conclusions

A model which can be used to predict the Rayleigh wave generated by an EMAT of arbitrary configuration has been discussed. The model combines analytical solutions and numerical calculations to calculate the Rayleigh waves. Although the Rayleigh wave generated by the Lorentz force may be determined using the FEM approach, a huge computer resources are required due to the mesh requirements for the Lorentz force calculation and the Rayleigh wave calculation being different. The situation becomes more serious for 3-dimensional problems. Also such full numerical calculations fail to yield a physical explanation of the phenomena occurring.

A linear and a flat spiral or 'pancake' coil have been used as examples and their Lorentz forces have been calculated. The Lorentz force due to the dynamic magnetic field mainly has an out-of-plane component, always acts as a repulsive force between the EMAT and the sample and is independent of the static magnetic field. The Lorentz force due to the static magnetic field is dependent on the static field. The two forces can work constructively or destructively to generate Rayleigh waves dependent on the orientation of the static magnetic field.

The Rayleigh waves of a spiral coil have been calculated and measured using a Michelson laser interferometer. Good agreement between measured calculated/ simulated results has been observed proving the usefulness of the method presented in this chapter.

The Rayleigh wave has a larger out-of-plane displacement component compared to the in-plane displacement component for aluminium and steel. An out-of-plane Lorentz force can generate Rayleigh waves more efficiently than an in-plane Lorentz force of the same amplitude [17-21]. The Lorentz force due to the dynamic magnetic field mainly has an out-of-plane component. When the applied static magnetic field is normal to the sample surface, the Lorentz force due to the static magnetic field mainly has an in-plane component and generates a Rayleigh wave

less efficiently than the Lorentz force due to the dynamic field for a pulsed excitation current of a peak amplitude about 300 *A* and a static magnetic field in air of about 0.39 Tesla in this chapter. Neglecting the contribution of the Lorentz force due to the dynamic magnetic field would cause a serious error in the shape and amplitude of the Rayleigh wave prediction [15-16].

Although Rayleigh waves close to the sample surface have been calculated in this chapter, this model can also be used to predict ultrasonic displacement in a sample.

6.6   References

1   Jian X, Weight J, Grattan, K T V, Miniature wideband ultrasonic transducers to measure compression and shear waves in solid, *Sensors & Actuators: A. Physical* 127 (2006), pp 13-23.

2   Jian X, S Dixon, Palmer SB, In-plane and Out-of-plane Particle Velocity Measurement Using EMATs, *Proceeding IEEE Ultrasonic Symposium* 2005.

3   Dewhurst R. J., Edwards C., McKie A. D. W., and Palmer S. B**.,** A remote laser system for ultrasonic velocity measurement at high temperatures, *J. Appl. Phys.* 63**,** pp 1225-1227, 1988

4   Jian, X., Dixon, S. and Edwards S. R., Ultrasonic Generation and Optimization for EMAT, *Review of progress in QNDE* 24A, pp1041-1046, 2004.

5   Jian X., Dixon S., Guo N., Edwards RS, Yan F., Pulsed Rayleigh Wave Interaction with a Surface Crack, *Proceeding of Ultrasonic International* 2005.

6   Edward RS, Jian X., and Dixon S, Signal Enhancement of the in- and out-of-plane Rayleigh wave components, *Applied Physics Letters* 87, 194104 (2005).

7   Jian, X., Dixon, S., Edwards, R.S., Reed J., Coupling Mechanism of an EMAT, accepted by *J. Acoust. Soc. Am.* 2005.

8   Jian, X., Dixon, S. and Edwards S. R., Optimal ultrasonic wave generation of EMAT for NDE, *Non-destructive & Evaluation*, pp 42-62, 2005.

9   Dodd, CV, Deeds, WE, Analytical solutions to eddy-current probe-coil problems, *J. Appl. Phys.* 39, pp2829-2838, 1968.

10   Dobbs E R, "Electromagnetic Generation of Ultrasonic Waves," *Physical Acoustics* 10, edited by Mason W P and Thurston R N, Academic Press, 1973, pp127.

11   Kawashima K, "Theory and numerical calculation of the acoustic field produced in metal by an electromagnetic ultrasonic transducer", *J. Acoust. Soc. Am.* 60, pp1089-1099, 1976.

12   Thompson, R. B., "Mechanisms of electromagnetic generation and detection of ultrasonic Lamb waves in iron-nickel alloy polycrystals," *Journal of Applied Physics* 48, pp4942-4950, 1977.

13   Kawashima K. and Wright O. B., Resonant electromagnetic excitation and detection of ultrasonic waves in thin sheets, *J. Appl. Phys.* 72, pp.4830-4839, 1992

14   Ludwig R., You Z., Palanisamy R., "Numerical simulation of an electromagnetic acoustic transducer-receiver system for NDT applications," *IEEE Trans. Magnetics* 29, pp.2081-2089, 1993

15   Ogi, H. et al., "Line-focusing of ultrasonic *SV* wave by electromagnetic acoustic transducer," *J. Acoust. Soc. Am.* 103, pp2411, 1998.

16   Ogi, H., Hirao M., Ohtani T., "Line-focusing electromagnetic acoustic transducers for the detection of slit defects," *IEEE Trans UFFC* 46, pp.341-346, 1999.

17   Bresse, L F and Hutchins, D A, "Transient generation by a wide thermoelastic source at a solid surface," *J. Appl. Phys.* 65(4), pp1441-1446, 1989.

18   Bresse, L F and Hutchins, D A, "Transient generation of elastic waves in a solid by a disk-shaped normal force source," *J. Acoust. Soc. Am.* 86(2), pp810-816, 1989.

19   Viktorov IA, *Rayleigh waves and Lamb waves-Physical theory and application*, Plenum, New York, 1964.

20   Miklowitz J, The theory of elastic waves and waveguides, *Applied Mathematics and Mechanics* 22, edited by Lauwerier HA and Koiter WT, North-holland Publishing Company, Amsterdam, 1978 and 1980.

21   Achenbach JD, Wave propagation in elastic solids, *Applied mathematics and mechanics 16*, edited by Lauwerier HA and Koiter WT, North-holland Publishing Company, Amsterdam, 1973.

7. APPLICATION OF A FOCUSED ULTRASONIC TRANSDUCER IN BOND EVALUATION

7.1 Summary

The evaluation of weak bonds within an IC package has been investigated in this chapter. Samples of IC packaging have been fabricated containing structures of the die (silicon) / die-attach (silver-based adhesive) / lead-frame (copper), which are typically found in IC packaging, and are degraded, to various extents, through thermal cycling to obtain varied levels of bond degradation. Interface reflection ultrasonic waveforms have been measured using a spherically-focused transducer and C-scan imaging is carried out, with the results explained using an interface spring model. The ultrasonic waveforms and images obtained clearly match the thermal-cycling history, the failure shear stress measurements and the results of optical microscopy reasonably well.

7.2 Introduction

Ultrasonic inspection is one of the most effective Non-destructive Testing (NDT) methods available for bond evaluation [1-12]. Longitudinal waves [1-4], shear waves [5] and Lamb waves [6] have been used for bond evaluation. When a sample comprising more than two layers is considered and interest is not limited to only the first interface, it is difficult to extract the required information using a Lamb wave method, due to the complicated mode structure [1, 5]. A deconvolution technique has been reported for separating the signals arising from the different interfaces to improve the capability of achieving deeper interface evaluation [1], and frequency spectra information has been widely used [7-8].

Ultrasonic detection of total disbonds (where an air gap exists between two layers) has been successfully demonstrated. However, it is very difficult to quantify the degree of bond weakness. The challenge arises from the lack of a valid and clear definition of what is a weak bond due to the uncertainties of interface degradation mechanisms, adhesive properties, non-identical ultrasonic transducers, and the frequency dependency of the ultrasonic response to the weak interface. An interface spring model has been reported to predict the interface reflection echoes at a uniform weak interface for the case where the wavelength is larger [9-12] or smaller [1] than the thickness of the adhesive layer.

Integrated circuit (IC) plastic packaging has a layered structure consisting of an epoxy mould compound / die (silicon) / die-attach (silver-based adhesive) / lead-frame (copper)/ epoxy mould compound, typically of thickness less than 1 mm [13-15]. The entire structure is usually encapsulated by an epoxy mould compound. Weak interfaces within the IC package may occur prior to other defect types during the fabrication process, and could cause failure in the packaging process and subsequently in-service. The causes of such defects can be contamination on the surface prior to bonding, use of unsuitable adhesive, improper curing of adhesive, and various other types of potential degradation mechanisms that can arise after curing or packaging [13-15]. The sample preparation and evaluation of the causes of weak bonding prior to the final stages of fabrication have been examined in other publications [13-15]. This chapter focuses on a study of weak interfaces in IC packaging, formed after curing and packaging, which in our case arises due to a degradation mechanism consistent with long term service in a humid environment.

Since the type of degradation chosen for study arises from a long term process, bond condition at a point weakens gradually with time, and the area of weakness in the bond develops slowly over time. Due to the manufacturing techniques used and the geometry of the structure, some locations of the IC components are more vulnerable to degradation than others. This comprises the non-uniform spatial distribution of a weak bond.

In order to reduce the beam spot at the interface, to enhance the spatial resolution and to obtain separated echoes from consecutive interfaces within the IC packaging, a spherically-focused broadband transducer with a nominal centre frequency of 100 MHz was used in measurement in immersion. In a similar way to non-contact transducers [16], piezoelectric transducers in immersion [17] do not have the coupling problems evident from direct-contact transducers. Therefore, the interface spring model can be used to predict the interface reflection echoes in IC packaging.

This chapter is organized such that the section entitled Methods describes the experimental setup and the spring model for weak bonds and sample preparation. The section of Results presents the experimental results including the C-scan imaging, A-scan waveforms, microscopy of disbonded sample surfaces and failure shear strength measurements. Finally, conclusions are given in the last section.

7.3   Methods

For a multilayer (more than two layers), the first interface can be evaluated using longitudinal, shear or Lamb waves, or alternatively using a resonance method. In order to evaluate at a deeper level, such as at the second or third interface, normal or angled longitudinal and shear wave incidence are widely used. By studying the reflection coefficient at an interface, information that relates to the condition of the bond can be obtained.

Creating a model describing the boundary conditions allowing for stress and strain across an interface to be evaluated is very important. It allows an understanding of the physical process and thus a prediction of the ultrasonic response from a weak interface, and using the model the interfacial condition can be evaluated quantitatively. The key problem is that the boundary conditions of realistic interfaces in IC packaging are generally not simple and cannot therefore be described by a relatively simple mathematical model such as the spring model, and is likely to give rise to errors on interface evaluation.

7.3.1   Ultrasonic interface model

The spring model assumes a virtual spring linking two boundaries together. The strain and stress at the two boundaries can be described by Hooke's law, and the spring stiffness is related to the bond condition.

A virtual spring can be used to represent a very thin adhesive layer bonding two layers together [9-12], and it may also be used to describe two directly contacting boundaries [1], as is the case considered in this chapter. The reflection coefficient of an imperfect interface at normal incidence from layer i to layer j is given by [1]

$$R_{ij} = \frac{Z_j - Z_i + i(\omega / K_{nij})Z_i Z_j}{Z_j + Z_i - i(\omega / K_{nij})Z_i Z_j} \tag{7.1}$$

where Z_i and Z_j are the acoustical impedance of layers i and j respectively, ω is angular frequency of the incident ultrasonic wave and K_{nij} is the normal spring stiffness of the interface. The reflection coefficient increases with spring stiffness, and is dependent on the frequency of the incident ultrasonic waves.

Considering the multilayer structure of die / die-attach / lead-frame in IC packaging, with the ultrasonic waves being at normal incidence to the silicon layer, the reflection coefficients at the two interfaces of the structure can be calculated using Equation 7.1. Figure 7.1 shows the schematic structure using the spring model in the IC. At interface 12, the reflection coefficient is -0.46 for a perfect bond and -1 for a total disbond. At interface 23, the reflection coefficient is 0.72 for a perfect bond and -1 for a total disbond. The relative change in the magnitude of the reflection coefficient from the perfect bond condition to the total disbond at interface 12 is larger than that at interface 23. However, at interface 23, phase reversal is observed.

Figure 7.2 shows the calculated reflection coefficients with respect to the frequency of the incident ultrasonic waves. The spring stiffness for interface 12 and 23 is

assumed to be the same with a value of $K_{n12} = K_{n23} = 6 \times 10^{15} \, \text{N/m}^3$. It is found that the reflection coefficients are dependent on the frequency of the ultrasonic waves [2, 7-8].

Figure 7.3 shows the calculated reflection coefficients with respect to spring stiffness for ultrasonic longitudinal waves with a frequency of 90 MHz. A spring stiffness below $8 \times 10^{14} \, \text{N/m}^3$ is approximated to a total disbond, whilst a stiffness above $5 \times 10^{16} \, \text{N/m}^3$ is approximated to be a perfect bond. A spring stiffness in the range of 8×10^{14} to $5 \times 10^{16} \, \text{N/m}^3$ is assumed to be a weak bond, based on the calculated value of the reflection coefficient. If the incident ultrasonic waves are of a different frequency to 90 MHz, then the values of spring stiffness over which a perfect bond may be assumed, a total disbond or a weak bond will change. Ultrasonic waves of a higher frequency will generally be more sensitive to weak bonds.

Die

Interface 12 →

K_{n12}

Die-attach

Interface 23 →

K_{n23}

Lead-frame
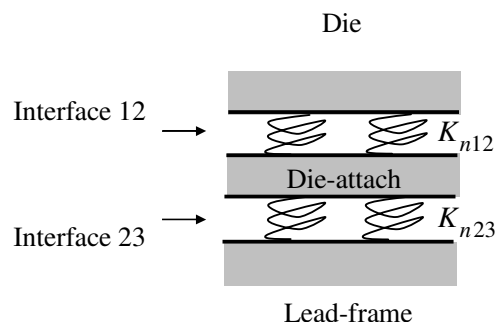
Figure 7.1 Structure in IC with spring model
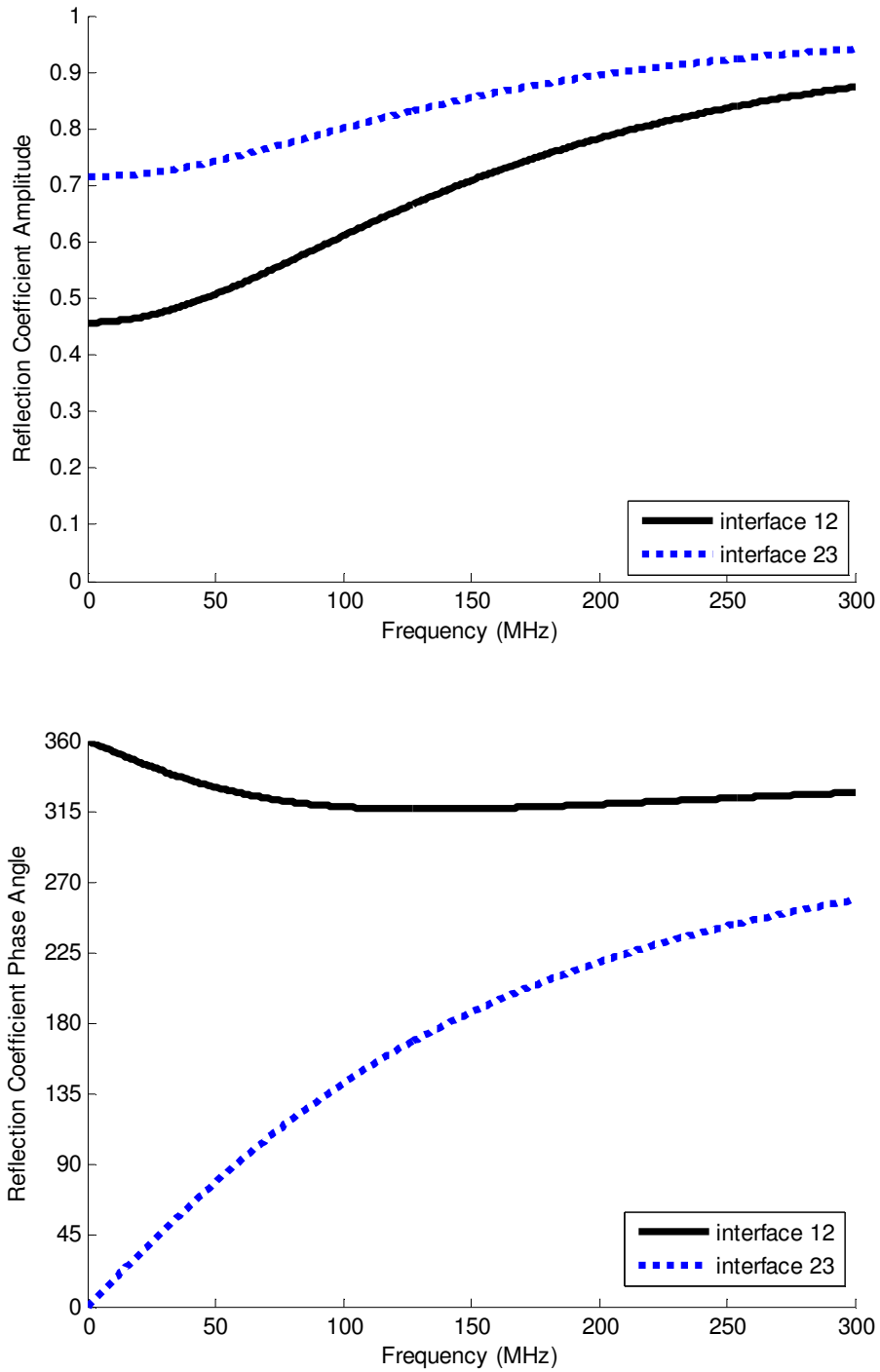
Figure 7.2 Reflection coefficients with regard to ultrasonic frequency at spring stiffness 6×10^{15} N/m^3
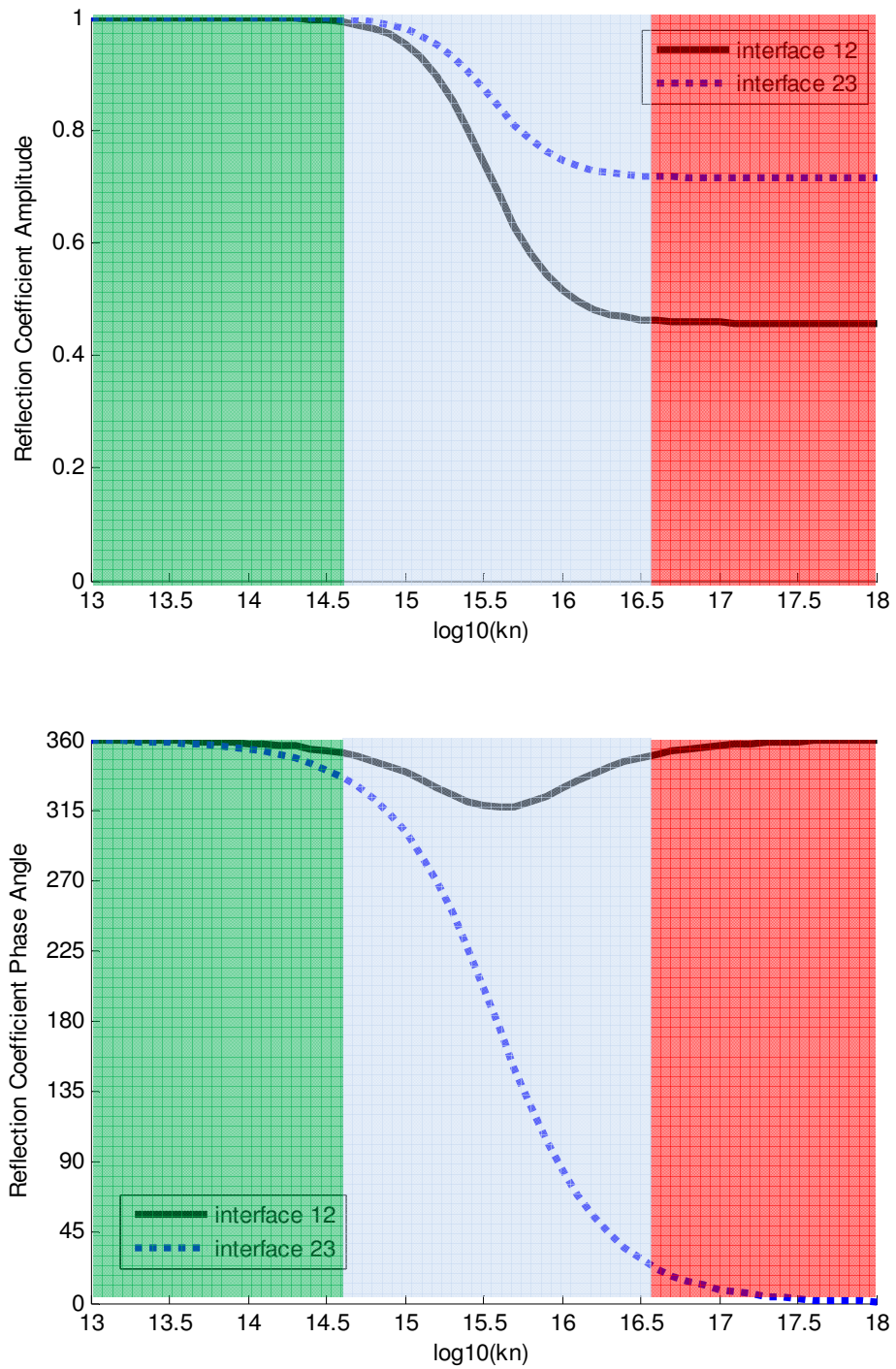
Figure 7.3 Reflection coefficients with regard to spring stiffness in log scale (top-amplitude; bottom-phase angle) at ultrasonic frequency of 90 MHz. Zones classification using 90 MHz ultrasound: Green-good; Blue-weak; Red-bad.
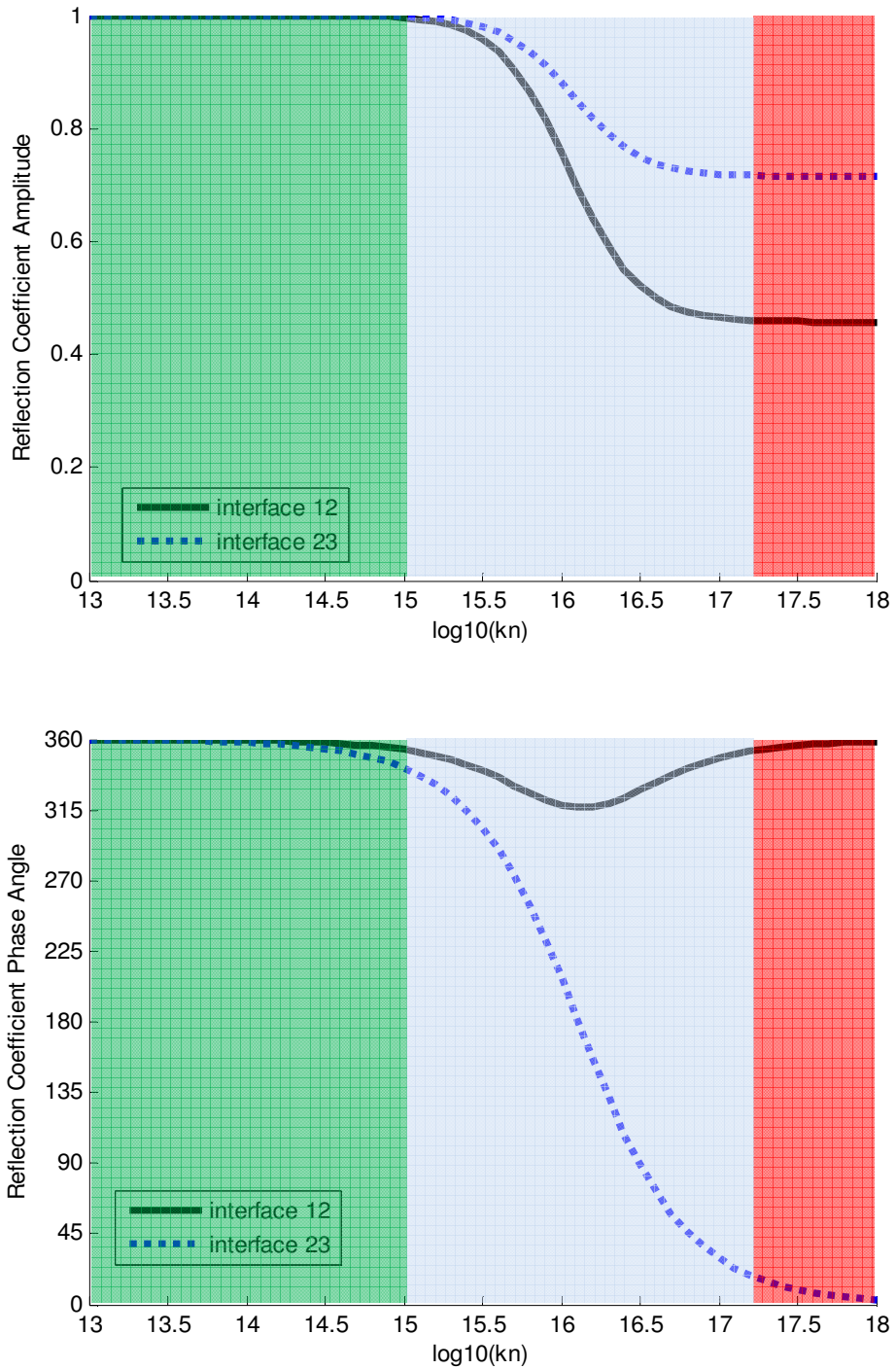
Figure 7.4 Reflection coefficients with regard to spring stiffness in log scale (top-amplitude; bottom-phase angle) at ultrasonic frequency of 150 MHz. Zones classification using 150 MHz ultrasound: Green-good; Blue-weak; Red-bad.

From Equation 7.1 and figures 2-3, the determination, using ultrasonic devices, of what is a weak bond is strongly frequency dependent [4]. Therefore the interface condition based on a measurement of the reflection coefficient or a change in the reflection coefficient, then some type of calibration is necessary. There is a need to ensure that the interface evaluation made using one particular ultrasonic transducer is comparable to that made by another ultrasonic transducer, and that these are referenced to other measurements taken using non-ultrasonic means.

7.3.2   Sample preparation

The first step in the work of this investigation was the preparation of samples with varied degrees of a weak bonding. Then a transducer of the required frequency characteristics was selected, and the experimental measurement set-up constructed. Finally, the ultrasonic model is validated by comparison with measurements and microscopy on the samples.

Two thermally and electrically conductive silver-based adhesives were used in this chapter for bonding the silicon and copper components as is best practice in IC packaging. The samples fabricated using the two adhesives were termed group 1 and group 2 respectively. The copper lead frame has dimensions $40 \times 25 \times 0.25$ mm, and the silicon part has dimensions $8 \times 8 \times 0.615$ mm. The material properties are shown in Table 1. A specially designed mould was made and used in sample fabrication to keep the adhesive thickness uniform at around 80 micrometers.

	Silicon	Adhesive 1	Adhesive 2	Copper
Density (kg/ m³)	2279	2652	2180	8920
Longitudinal wave velocity (m/s)	7892	2525	2231	4520

Table 7. 1 Material properties

The copper and silicon components were washed with detergent, and then with fresh water. After drying with compressed air, the components were washed with silicone. After cleaning, the copper component wa placed in the mould, the adhesive was then applied to the copper, and the silicon component placed onto the adhesive. The mould lid was then applied and then the entire mould placed in an oven to cure the adhesive. The curing process takes 50 minutes at a temperature of $120^{O}C$ in accordance with the adhesive manufacturer's instructions.

The samples are assumed to have been fabricated with perfect bonds. The two groups of samples experienced different degradation processes. The samples of group 1 were immersed in a chamber containing ice and water for 5 seconds, then immediately transferred and immersed in a chamber of boiling water for 5 seconds. That step constitutes one cycle. The samples can rapidly reach the temperature of the contents of each chamber because the volume of the water is much larger than that of the samples. The samples experience 100 cycles per day and are subsequently soaked in water at room temperature until the next degradation process is performed. To achieve varied interfacial conditions, samples were divided into several sub-groups of degradation cycles of 0, 500, 600, 680 and 760 cycles.

The second group of samples were placed in a chamber with a relative humidity of 85% and the temperature is cycled from $-20^{O}C$ to $180^{O}C$ within 8 minutes. These samples were also divided into several sub-groups of degradation thermal-cycling time of 0, 60, 72, 82 and 90 hours.

7.3.3   Ultrasonic measurements

A spherically-focused wideband ultrasonic transducer of nominal centre frequency 100 MHz is used for C-scan imaging and A-scan waveform measurement in this work. The transducer has a focus length of 3.2 mm, a cross-sectional beam size of 0.015 mm at the focal point and an active diameter of 3.2 mm. Samples of varied interfacial conditions were placed in a water bath for immersion C-scan imaging and A-scan waveform acquisition. Figure 7.4 is a schematic diagram of the measurement setup, where the ultrasonic waves are incident on the sample from the silicon layer side. The broadband ultrasonic waves that are generated by the transducer propagate down through the water giving a very small beam spot at interfaces 12 and 23.

C-scan (signal amplitude) imaging, together with a measurement of the polarity of the detected signal was used in this study, such that the magnitude of the signal is digitized to seven bits and an eighth bit is used to indicate polarity. The polarity of a pulse is defined where the echoes that are in phase with the incident ultrasonic signal have a positive polarity and visa versa. A colour scale bar is presented along the left side of each C-scan image that effectively runs from values equivalent to -128 to +127. There are several choices for colour maps. For a positive polarity signal the minimum to maximum peak amplitude runs from a grey scale of black (0) to white (127). For a negative polarity signal the minimum to maximum peak amplitude runs from black (0), through yellow to red (-128). In previous section, it has been demonstrated that the phase of an ultrasonic echo reflected from a weak interface 23 is between 0 and π. In the following measurements these phase predictions are experimentally verified.
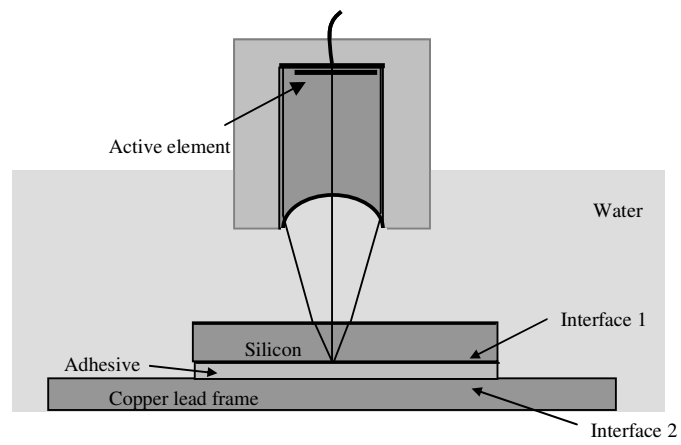
Figure 7.5 Measurement arrangement

7.4   Results

It is reasonable to assume that the samples that experience a greater level of thermal-cycling are statistically more likely to have of weaker bonds and worse interfacial conditions. Although the extent of degradation is also dependent on the properties of the adhesive used, the number or hours of thermal-cycling itself is an indication of interface weakness. C-scan imaging and A-scan waveform measurements are taken at each stage of thermal-cycling. In order to better understand the ultrasonic response of a weak interface, failure shear stress and optical microscopy are performed and the results from these are compared with the ultrasonic measurements.

7.4.1   Ultrasonic results

Figure 7.5 shows C-scan images of a sample of group 1 at interface 12 (*a*) and 23 (*b*). Figure 7.6 shows A-scan waveforms changing with respect to thermal cycles of 0, 500, 600, 680 and 760 respectively.

From Equation 7.1 and figures f.2 and 7.3, the phase of the reflection coefficient at interface 12 is approximately π, and so the polarity of the image is ascribed a value of -1. The phase of reflection coefficient at interface 23 is should be 0 for a perfect bond and π for a total disbond. They are of polarity +1 and -1, and are shown by grey scale and yellow-red color range respectively. It is observed that the yellow area increases with thermal-cycling, indicating that the interface has suffered degradation.

In Figure 7.6, the first echo of each waveform corresponds to an ultrasonic wave pulse that is reflected from the interface between the water and the silicon layer. It is constant in amplitude and shape denoting a consistent coupling condition for the 5 measurements. The second and third echoes are reflected from interface 12 and 23 respectively, which are used to produce the C-scan images of figure 7.5. The echoes from interface 12 show little variation in shape and amplitude, whilst the echoes

from interface 23 appear to change gradually from a positive to a negative polarity with increased cycling. This would appear to verify the predictions shown in figure 7.3, based on Equation 7.1.

Figure 7.7 shows C-scan images of a sample of group 2 at interfaces 12 (*a*) and 23 (*b*). Figure 7.8 shows A-scan waveforms corresponding to varied thermal cycle hours. The amount of red area in figure 7.8 increases with thermal-cycling, indicating the degradation of interface 12. The shadow area in figure 7.7(b) increases with thermal-cycling too, because the degradation of interface 12 allows fewer ultrasonic waves to pass through the interface and reach interface 23. Accordingly, the ultrasonic echo reflected from interface 23 is lower. This can be verified by examining the A-scan waveforms in figure 7.8. The echoes from interface 12 increase in amplitude without shape change whilst the echoes from interface 23 decrease in amplitude. Note that the weak interface 23 leads to an amplitude increase and shape or polarity change from in-phase to out-of-phase as already shown in figure 7.6(b).
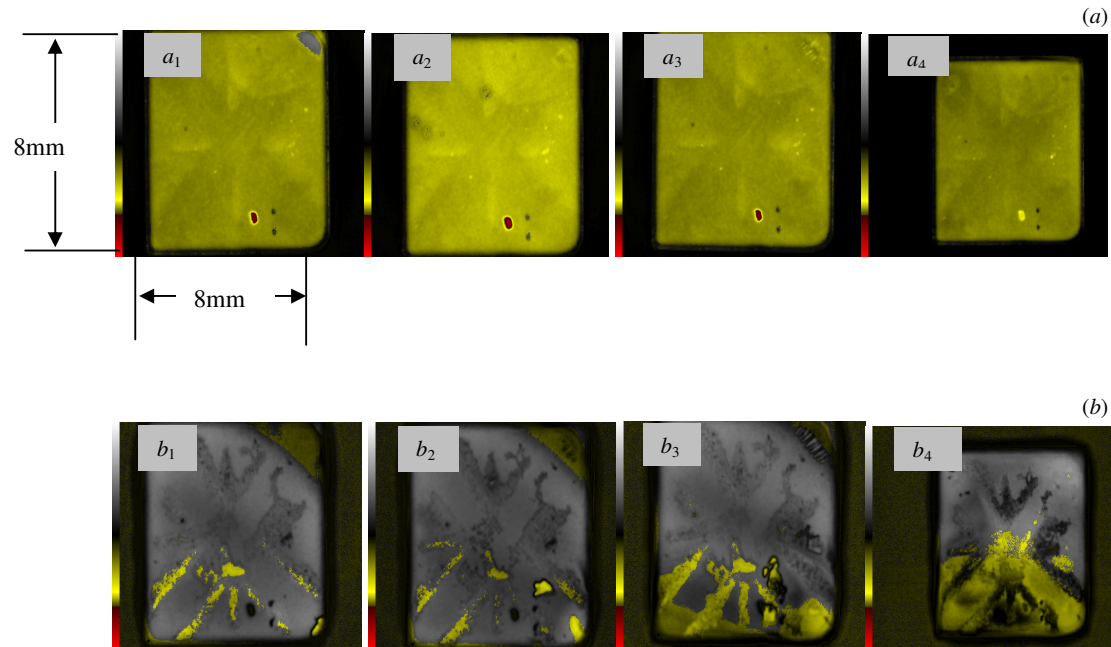
Figure 7.6 C-scan images at interfaces 12 (*a*) and interface 23 (*b*) of a sample of group 1.
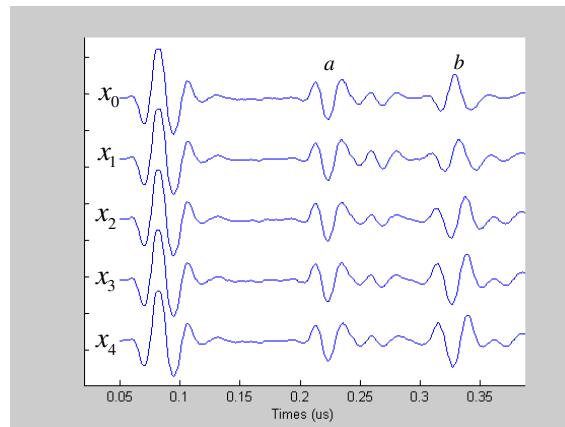
Figure 7.7 Waveforms measured at the same location of a sample with different number of thermal cycling. Amplitude and shape change of the echoes (*b*) that are reflected at interface 23 is observed indicating interface degradation. The echoes (*a*) that are reflected at interface 12 nearly do not change in shape and amplitude
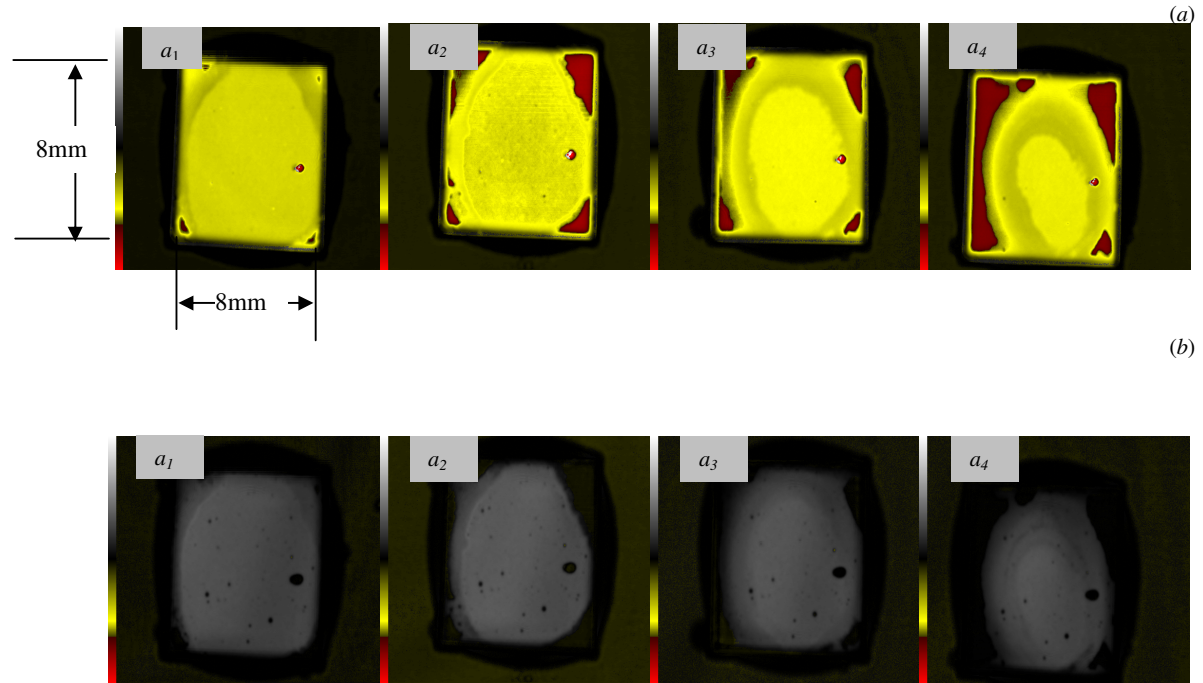
**Figure 7.8 C-scan images at interfaces 12 (*a*) and interface 23 (*b*) of a sample of group 2**
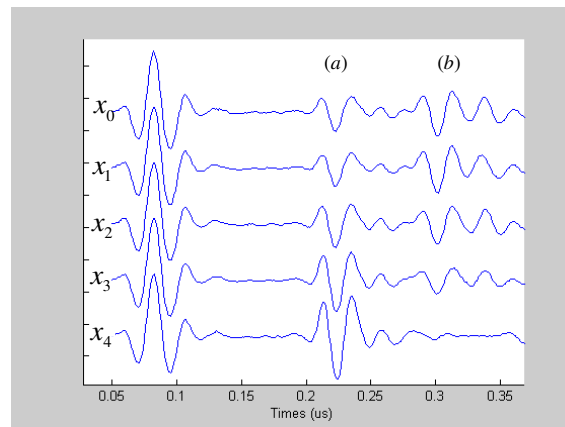
Figure 7.9 Waveforms measured at the same location of a sample with different number of thermo cycling. The echoes (*a*) that are reflected from interface 12 increase in amplitude indicating the degradation of interface 12, which causes the amplitude reduction of the echoes (*b*) that are reflected at interface 23.

7.4.2   Non-ultrasonic results

Because the lead-frame is much larger than silicon component in area, the failure shear strength of the adhesive / lead-frame interface can be measured more easily than that of the silicon / adhesive interface. A special jig was designed and fabricated to undertake this measurement. Ten samples were selected from each degraded sample group for the measurement of the failure shear strength and the results are shown in Table 2. The first two rows in Table 2 are the results from first group of samples, and the third and fourth rows are the results from the second group of samples. For the first group of samples, the failure shear strength clearly changes with respect to the number of thermal cycles between 500 and 680 cycles. After the samples experience 680 thermal cycles, the failure shear strength decreases sharply. For the second group of samples, the failures shear strength changes very clearly with respect to the total time of thermal cycling between 60 and 82 hours. After 82 hours of thermal cycling, the failure shear strength decreases sharply.

The disbonded samples after the failure shear strength were studied using optical microscopy. Figure 7.9 is an optical image of a sample from the first group on the adhesive surface that was contacting the lead-frame. Dark spots visible in figure 7.9 correspond to cavities, where some adhesive has remained fixed to the lead-frame. Such cavities indicate that in these regions, the adhesion between the adhesive and lead-frame was stronger than the cohesive strength within adhesive. These areas then correspond to good interfacial bonding at the time of the measurement of the failure shear strength. It is interesting to note that such cavities are distributed mainly along the cross in the C-scan images shown in figure 7.5(a).

Sample 1	Cycling Numbers	0	500	600	680	760
	FSS (MPa)	8.6	8	7.1	5.6	2.5
Sample 2	Cycling Hours	0	60	72	82	90
	FSS (MPa)	6.5	5.9	5.5	4.8	3.6

Table 7. 2 Measured failure shear strength (FSS)
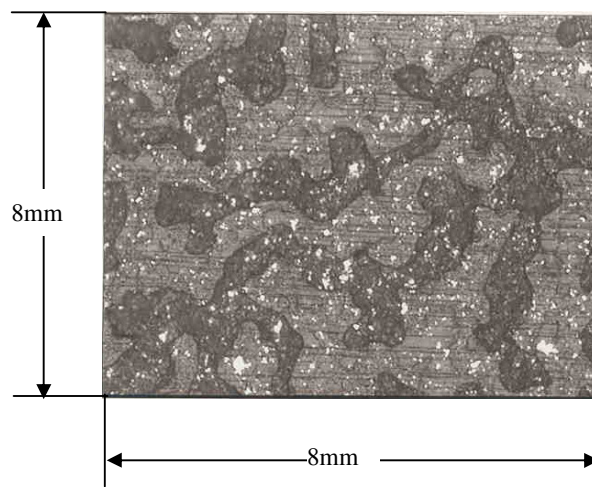

Figure 7.10 Optical image on the adhesive surface contacting lead-frame. Dark spots are cavities.

7.5 Conclusions

Weak bond evaluation in IC packaging with a typical structure of silicon / adhesives / lead-frame has been investigated in this chapter. Thermal-cycling was used to prepare samples with varied interfacial conditions, leading to an interfacial degradation that is gradual both temporally and spatially. A broadband spherically-focused transducer with a nominal centre frequency of 100 MHz was used in immersion mode, and the ultrasonic beam focused to a very small spot at the interfaces between the silicon and adhesive and between the adhesive and lead-frame. The interfacial condition over the area insonified by the focused beam can be considered uniform. Such a spherically-focused transducer has the capability to measure ultrasonic echoes of a specific interface condition at a point rather than an average over a larger area as would be obtained with a larger focal spot size. Therefore the measurements compare well with the predictions made by an interface spring model that is based on a uniform interfacial condition. An ultrasonic response for a specific interfacial condition rather than an average of a non-uniform interfacial condition has been obtained

Ultrasonic C-scan imaging and A-scan waveform measurements were captured, and have been used to monitor the interfacial degradation ageing. The ultrasonic behavior of a weak interface 12 was observed to be different from that of weak interface 23. Ultrasonic responses of a weak interfaces were experimentally measured. The imaging polarity of a reflected signal has been found to be insufficient to provide useful information of a weak interface. Also, due to the specific adhesive properties and the structure examined, it is observed that some parts of the package were more vulnerable to degradation.

Failure shear stress measurements correlate well with thermal cycling and ultrasonic measurements. Because failure shear stress is an average result, it is very difficult to determine quantitatively the interfacial condition. Both the microscopy and failure shear stress measurements are of course destructive techniques. Ultrasonic measurements (both C-scan and A-scan) correlate well with the number of thermal

cycling that a sample has experienced, demonstrating the potential usefulness of ultrasonic weak interface evaluation in IC packaging.

7.6   References

1   X. Jian and N. Guo, et al, "Characterization of bonding quality in a multilayer structure using segment adaptive filtering," *J. NDE* 21 (2), pp55-65, 2002.

2   B. Drinkwater, P. Cawley, "Measurement of the frequency dependence of the ultrasonic reflection coefficient from thin interface layers and partially contacting interface," *Ultrasonics* 35, pp479-488, 1997.

3   K. Vine, P. Cawley, A.J. Kinloch, "Comparison of normal and oblique incidence ultrasonic measurements for the detection of environmental degradation of adhesive joints," *NDT & E International* 35 (2002): 241-253.

4   S.I. Rokhlin, L. Wang, B. Xie, et al., "Modulated angle beam ultrasonic spectroscopy for evaluation of imperfect interfaces and adhesive bonds," *Ultrasonics* 42 (2004): 1037-1047.

5   S. Dixon, .D Jaques, S. Palmer and G. Rowlands, "The measurement of shear and compression waves in curing epoxy adhesives using ultrasonic reflection and transmission techniques simultaneously," *Meas. Sci. Technol.* 15, 939-947, 2004.

6   F. Di Scalea, P. Rizzo, A. Marzani, "Propagation of ultrasonic guided waves in lap-shear adhesive joints: Case of incident a(0) Lamb wave," *J. Acoust. Soc. Am.* 115: 146-156, 2004.

7   A.I. Lavrentyev and S.I. Rokhlin, "Ultrasonic spectroscopy of imperfect contact interfaces between a layer and two solids," *J. Acoust. Soc. Am.*103, pp657-664, 1998.

8   J. Allin, P. Cawley, M. Lowe, "Adhesive disbond detection of automotive components using first mode ultrasonic resonance," *NDT&E Int*. 36 (7): 503-514 Oct 2003.

9   D. Levesque, A. Legros, A. Michel, et al., "High-resolution ultrasonic interferometry for quantitative nondestructive characterization of interfacial adhesion in multilayer (metal-polymer metal) composites," *J. Adhesion Sci. Technol.* 7 (1993): 719-741.

10   D. Jiao, "An ultrasonic interface layer model for bond evaluation," *J. Adhesion Sci. Technol*. 5 (1991): 631.

11   S.I. Rokhlin, B. Xie, A. Baltazar, "Quantitative ultrasonic characterization of environmental degradation of adhesive bonds," *J. Adhesion Sci. Technol* 18 (2004): 327-359.

12   A.I. Lavrentyev, J.T. Beals, "Ultrasonic measurement of the diffusion bond strength," *Ultrasonics* 38 (2000): 513-516.

13   E. Wong, S. Koh, K. Lee, R. Rajoo, "Comprehensive treatment of moisture induced failure - Recent advances," *IEEE Trans*. *Elec*. *Pack*. *Manu*. 25, pp 223-230, 2002.

14   M. Sato, H. Yokoi, "Visualization analysis of melt flow in IC packaging process along thickness direction," *IEEE Transactions on Advanced Packaging* 23 (4): 729-736 Nov. 2000.

15   S. Kim, "The role of plastic package adhesion in performance," *IEEE Trans. CHMP*, pp 809-817, 1991.

16   X. Jian, et al, "Coupling mechanism of electromagnetic acoustical transducers for ultrasonic generation," *J. Acoust. Soc. Am.* 119 (2006), pp 2693-2701.

17   X. Jian, et al, "Miniature wideband ultrasonic transducers to measure compression and shear waves in solid," *Sensors & Actuators: A. Physical* 127 (2006), pp 13-23.

8. CONCLUSIONS AND FURTHER WORK

8.1 Conclusions

This thesis explores a broad range of ultrasonic field measurement and modelling, optimal probe/EMAT for ultrasonic generation and detection of specially intended components of ultrasonic waves. The primary objective of the research was to develop new and innovative techniques that were both accurate and robust. Six main problem areas were focused on including

- Measurement of ultrasonic field in solid of a piezoelectric transducer either in immersion or with piezoelectric transducer directly mounted.

- Modelling of ultrasonic field in solid of a piezoelectric transducer either in immersion or with piezoelectric transducer directly mounted.

- EMAT measurement of in-plane and out-of-plane ultrasonic particle velocities.

- Experimental study and modelling of optimal Rayleigh wave generation of EMATs.

- Modelling of optimal Rayleigh wave generation of EMATs.

- High lateral spatial resolution ultrasonic pulse echo technique for weak bond evaluation.

These problem areas are found throughout many engineering disciplines and the adaptability and suitability of the techniques developed shows the great potential for practical NDT.

The ultrasonic fields of a conventional piezoelectric probe were described as plane waves and edge waves and were shown to be quite different from typical ultrasonic

pulse-echo responses observed elsewhere. The capability to measure edge waves promotes the potential of the detection of planar defect edge scattering signals, which would improve defect detection capability.

EMATs can be specially designed to pick up in-plane or out-of-plane or both by applying an external magnetic field in the appropriate manner. This has been experimentally validated by comparing phase and amplitude of measured in-plane and out-of-plane Rayleigh waves with theoretical predictions.

For EMAT ultrasonic generation, excitation electric currents induce eddy currents in the electrically conductive material and magnetic field around the EMAT. The interaction of the induced eddy current with the generated magnetic field produces Lorentz force for ultrasonic generation without the presence of an external magnetic field. However, it was found that if an external magnetic field is applied correctly, the efficiency of ultrasonic signal generation can be enhanced. Because of its low transduction, EMAT optimization becomes crucial to successful applications.

There are some piezoelectric transducers that can work at high temperatures either through the use of piezoelectric ceramics of high Curie temperature (the ceramics has low transduction efficiency or through the use of special dry couplant layers to the hot test pieces. On both cases, the overall ultrasound transduction efficiency is low. Piezoelectric transducer techniques require ultrasound couplant and are therefore not suitable for automated inspection of hot test pieces because liquid couplant is boiled off quickly and dry couplant layer causes difficulty for the probe to move freely. The EMAT bored technique is non-contact and couplant free and can therefore work at high temperature. These attributes make it ideal for inspection in extreme conditions, such as high temperature, high speed, etc.

Weak bond evaluation in IC fabrication has always been a challenge. As an example of practical applications, this study has evaluated Integrated Circuit packaging in electronic industry using Scanning Acoustical Microscopy (SAM). The relationship among resulting ultrasonic C-scan images, destructive mechanical

failure measurements over serial degradation cycles have been observed. The result is promising indicating that SAM is a very useful tool for weak bond evaluation.

8.2   Further Work

There is a clearly potential for future work regarding the techniques developed and areas explored in this thesis, which are of great interest and significance to NDT, but were beyond the scope of this investigation due to limited time.

Further to optimal Rayleigh wave EMAT generation, it is worth exploring EMAT design for generation of longitudinal waves, shear waves and Lamb waves to improve efficiency. These should be done by experimental measurement and modelling.

It has already seen that ultrasonic field signals are quite different from ultrasonic pulse-echo responses. Ultrasonic pulse echo responses are predominantly specular reflections. Planar defects such as cracks have a much greater impact on material integrity than volumetric defects. Where incident ultrasonic beams are not near norm to the major face of a planar defect, specular reflection is weak and there is risk of failure of detection of the defect. With a miniature probe or small probe, which can be a piezoelectric transducer or an EMAT, defect edge scattering signals may be comparable with plane wave reflections in amplitude. It is also less orientation dependent. With advanced amplification and filtering, defect scattering signals may be detected with a good signal to noise ratio, which is potentially highly advantageous and may provide complementarity to conventional UT in pulse echo.

The EMAT technique is non-contact and couplant free and can work at high temperature. These attributes make it ideal for inspection in extreme conditions, such as high temperature, high speed, etc. Areas of EMAT onload monitoring at high temperature certainly should be studied.

Evaluation of weak bonds e.g. in IC inspection applications is still a major challenge. Further to the high spatial resolution technique presented in this thesis, a combination of it and another nonlinear ultrasonic assessment may bring forward good results and should be explored.

LIST OF PUBLICATIONS

[1].   Jian X, Weight JP, Grattan KTV, Miniature wideband ultrasonic transducers to measure compression and shear waves in solid, *Sensors & Actuators: A. Physical* 127 (2006): 13-23.

[2].   Jian X, Dixon S, Grattan KTV, Edwards RS, A Model for Pulsed Rayleigh Wave & Optimal EMAT Design, *Sensors & Actuators: A. Physical* 128 (2006): 296-304.

[3].   Jian X, Guo N, Dixon S, Grattan KTV, Ultrasonic Weak Bond Evaluation in IC Packaging , *Meas. Sci.& Techno.* 17 (2006): 2637-2642.

[4].   Jian X, Weight JP, Grattan KTV, Dixon S, A model for propagation of short pulses of ultrasound in solid immersed in a fluid, *Sensors & Actuators*: A *Physical* 133 (2007): 439-446.

[5].   Jian X., S Dixon, K Quirk, K T V Grattan, Electromagnetic Acoustic Transducers for In- and Out-of plane Ultrasonic Wave Detection, *Sensors & Actuators A: Physical*,148 (2008), pp151-156.